2002-09

A fine resolution model of the Leeuwin Current System off western and southern Australia

Phillips, Robyn L.

Monterey, California. Naval Postgraduate School

NAVAL POSTGRADUATE SCHOOL
Monterey, California

THESIS

A FINE RESOLUTION MODEL OF THE LEEUWIN CURRENT SYSTEM OFF WESTERN AND SOUTHERN AUSTRALIA

by

Robyn L. Phillips

September 2002

Thesis Advisor: Mary L. Batteen
Second Reader: Curtis A. Collins

Approved for public release; distribution is unlimited

THIS PAGE INTENTIONALLY LEFT BLANK

REPORT DOCUMENTATION PAGE			Form Approved OMB No. 0704-0188
Public reporting burden for this collection of information is estimated to average 1 hour per response, including the time for reviewing instruction, searching existing data sources, gathering and maintaining the data needed, and completing and reviewing the collection of information. Send comments regarding this burden estimate or any other aspect of this collection of information, including suggestions for reducing this burden, to Washington headquarters Services, Directorate for Information Operations and Reports, 1215 Jefferson Davis Highway, Suite 1204, Arlington, VA 22202-4302, and to the Office of Management and Budget, Paperwork Reduction Project (0704-0188) Washington DC 20503.			
1. AGENCY USE ONLY *(Leave blank)*	**2. REPORT DATE** September 2002	**3. REPORT TYPE AND DATES COVERED** Master's Thesis	
4. TITLE AND SUBTITLE: A Fine Resolution Model of the Leeuwin Current System off Western and Southern Australia			**5. FUNDING NUMBERS** N/A
6. AUTHOR(S) LEUT Robyn L. Phillips			
7. PERFORMING ORGANIZATION NAME(S) AND ADDRESS(ES) Naval Postgraduate School Monterey, CA 93943-5000			**8. PERFORMING ORGANIZATION REPORT NUMBER**
9. SPONSORING /MONITORING AGENCY NAME(S) AND ADDRESS(ES) N/A			**10. SPONSORING/MONITORING AGENCY REPORT NUMBER**
11. SUPPLEMENTARY NOTES The views expressed in this thesis are those of the author and do not reflect the official policy or position of the Department of Defense or the U.S. Government.			
12a. DISTRIBUTION / AVAILABILITY STATEMENT Approved for public release; distribution is unlimited.			**12b. DISTRIBUTION CODE**

13. ABSTRACT ***(maximum 200 words)***

To investigate the role of wind forcing, bottom topography and thermohaline gradients in the Leeuwin Current System (LCS) off western and southern Australia, several experiments are conducted with a sigma coordinate primitive equation model on a beta-plane. Results show that off the west (southern) coast the LCS is an anomalous eastern boundary current system that generates a coastal poleward (eastward) current, an equatorward (westward) undercurrent, and highly energetic mesoscale features such as meanders and eddies. Off the west coast, thermohaline forcing, wind forcing and bottom topography all play important roles: Thermohaline gradient effects are shown to be the primary mechanism in the generation of the poleward current, equatorward undercurrent, eddies and meanders. Inshore of the poleward surface flow, next to the coast, wind forcing also plays an important role in generating an equatorward coastal current and upwelling. Bottom topography is responsible for strengthening and trapping currents near the coast, intensifying eddies off capes and in preventing the undercurrent from becoming the dominant surface flow. Bottom topography is also shown to play a dominant role off the southern coast in trapping the eastward Leeuwin Current and the westward Flinders Current over the shelf break and slope, respectively. Overall, the results of the study compare well with available observations and previous studies of the LCS.

14. SUBJECT TERMS Primitive Equation Model, Leeuwin Current System, Great Australian Bight, Currents, Sigma-Level, Princeton Ocean Model (POM), Flinders Current			**15. NUMBER OF PAGES** 107
			16. PRICE CODE
17. SECURITY CLASSIFICATION OF REPORT Unclassified	**18. SECURITY CLASSIFICATION OF THIS PAGE** Unclassified	**19. SECURITY CLASSIFICATION OF ABSTRACT** Unclassified	**20. LIMITATION OF ABSTRACT** UL

NSN 7540-01-280-5500 Standard Form 298 (Rev. 2-89)
Prescribed by ANSI Std. 239-18

THIS PAGE INTENTIONALLY LEFT BLANK

Approved for public release; distribution is unlimited

A FINE RESOLUTION MODEL OF THE LEEUWIN CURRENT SYSTEM OFF WESTERN AND SOUTHERN AUSTRALIA

Robyn L. Phillips
Lieutenant, Royal Australian Navy
B.Sc. (Hons), University of New South Wales (ADFA), 1993

Submitted in partial fulfillment of the
requirements for the degree of

**MASTER OF SCIENCE IN
PHYSICAL OCEANOGRAPHY**

from the

**NAVAL POSTGRADUATE SCHOOL
SEPTEMBER 2002**

Author: Robyn L. Phillips

Approved by: Mary L. Batteen
Thesis Advisor

Curtis A. Collins
Second Reader

Mary L. Batteen
Chair, Department of Oceanography

THIS PAGE INTENTIONALLY LEFT BLANK

ABSTRACT

To investigate the role of wind forcing, bottom topography and thermohaline gradients in the Leeuwin Current System (LCS) off western and southern Australia, several experiments are conducted with a sigma coordinate primitive equation model on a beta-plane. Results show that off the west (southern) coast the LCS is an anomalous eastern boundary current system that generates a coastal poleward (eastward) current, an equatorward (westward) undercurrent, and highly energetic mesoscale features such as meanders and eddies. Off the west coast, thermohaline forcing, wind forcing and bottom topography all play important roles: Thermohaline gradient effects are shown to be the primary mechanism in the generation of the poleward current, equatorward undercurrent, eddies and meanders. Inshore of the poleward surface flow, next to the coast, wind forcing also plays an important role in generating an equatorward coastal current and upwelling. Bottom topography is responsible for strengthening and trapping currents near the coast, intensifying eddies off capes and in preventing the undercurrent from becoming the dominant surface flow. Bottom topography is also shown to play a dominant role off the southern coast in trapping the eastward Leeuwin Current and the westward Flinders Current over the shelf break and slope, respectively. Overall, the results of the study compare well with available observations and previous studies of the LCS.

THIS PAGE INTENTIONALLY LEFT BLANK

TABLE OF CONTENTS

I. INTRODUCTION 1

II. MODEL DESCRIPTION 5
- **A. DATA SETS 5**
- **B. PRE-PROCESSING 5**
- **C. BRIEF MODEL DESCRIPTION 7**
- **D. INITIALIZATION, FORCING AND BOUNDARY CONDITIONS 8**

III. RESULTS FROM MODEL SIMULATIONS 11
- **A. PRESSURE GRADIENT FORCE ERROR DETERMINATION 11**
- **B. WIND FORCING ON A FLAT BOTTOM 12**
- **C. WIND FORCING OVER TOPOGRAPHY 13**
- **D. THERMOHALINE FORCING ON A FLAT BOTTOM 15**
- **E. THERMOHALINE FORCING OVER TOPOGRAPHY 17**
- **F. WIND AND THERMOHALINE FORCING ON A FLAT BOTTOM ... 18**
- **G. WIND AND THERMOHALINE FORCING OVER TOPOGRAPHY .. 19**
- **H. DISCUSSION 21**

IV. SUMMARY 25

LIST OF REFERENCES 85

INITIAL DISTRIBUTION LIST 89

THIS PAGE INTENTIONALLY LEFT BLANK

LIST OF FIGURES

Figure 1. The model domain for the Leeuwin Current System (LCS) is bounded by 40°S to 22.5°S, 107.5°E to 142.5°E. The model domain has a closed boundary along the entire coast and four open boundaries. The 200m isobath is also shown. 28

Figure 2. Original topography (meters) in three-dimensions (from Sandwell and Smith, 1996) with a resolution of two minutes (1/30 degree). Contours depict the shoreline, 200m and 2500m isobaths. 29

Figure 3. Original topography (meters) in two-dimensions (from Sandwell and Smith, 1996) with a resolution of two minutes (1/30 degree). 30

Figure 4. Resolution grid lines with every fifth grid line plotted. (13.7 km by 10.2 km offshore resolution with the highest resolution being 5.7 km by 6 km). 31

Figure 5. Smoothed topography (meters) obtained after applying a one-dimensional robust iterative method and reassigning depths greater than 2500 m to 2500 m. Contours depict the shoreline and the 200 m isobath. 32

Figure 6. Smoothed topography (meters) in two-dimensions obtained after applying a one-dimensional robust iterative method and reassigning depths greater than 2500 m to 2500 m. 33

Figure 7. Plot of the 21 sigma levels. 34

Figure 8. Annual climatological surface temperature (°C) obtained from Levitus and Boyer (1994). 35

Figure 9. Annual climatological surface salinity from Levitus et al. (1994). 36

Figure 10. Annual average wind in m/s from climatological ECMWF winds obtained from Trenberth et al., 1990. 37

Figure 11. Surface velocity error (cm/s) due to the pressure gradient force error on day 10 for Experiment 1. 38

Figure 12a. Surface temperature (°C) and velocity vectors for Experiment 2 on day 39. .39

Figure 12b. Cross-section of temperature (°C) at 25.7°S for Experiment 2 day 39, with a contour interval of two degrees. 40

Figure 12c. Surface temperature (°C) and velocity vectors for Experiment 2 on day 60. .41

Figure 12d. Cross-section of temperature (°C) at 25.7°S for Experiment 2 day 60, with a contour interval of two degrees. 42

Figure 12e. Cross-section of north-south velocities (m/s) at 33.4°S for Experiment 2 day 60, with a contour interval of 2 cm/s. Red is equatorward (north). 43

Figure 12f. Cross-section of north-south velocities (m/s) at 30.4°S for Experiment 2 day 60, with a contour interval of 2 cm/s. Red is equatorward (north). 44

Figure 12g. Cross-section of temperature (°C) at 37.8°S for Experiment 2 day 60, with a contour interval of two degrees. 45

Figure 12h. Cross-section of east-west velocities (m/s) at 128.5°E for Experiment 2 day 60, with a contour interval of 2 cm/s. Red is westward. 46

Figure 13a. Surface temperature (°C) and velocity vectors for Experiment 3 on day 60. The 200m isobath is shown. 47

Figure 13b. Cross-section of temperature (°C) at 25.7°S for Experiment 3 day 60, with a contour interval of two degrees. 48

Figure 13c. Surface elevation (m) and velocity vectors for Experiment 3 on day 60. The 200m isobath is shown. 49

Figure 13d. Cross-section of temperature (°C) at 32°S for Experiment 3 day 60, with a contour interval of two degrees. 50

Figure 13e. Cross-section of north-south velocities (m/s) at 34°S for Experiment 3 day 60, with a contour interval of 5 cm/s. Red is equatorward (north). 51

Figure 13f. Cross-section of east-west velocities (m/s) at 128.3°E for Experiment 3 day 60, with a contour interval of 5 cm/s. Red is westward. 52

Figure 14a. Surface temperature (°C) and velocity vectors for Experiment 4 on day 42. .53

Figure 14b. Cross-section of north-south velocities (m/s) at 25°S for Experiment 4 day 42, with a contour interval of 5 cm/s. Red is equatorward (north). 54

Figure 14c. Cross-section of north-south velocities (m/s) at 34°S for Experiment 4 day 42, with a contour interval of 10 cm/s. Red is equatorward (north). 55

Figure 14d. Cross-section of temperature (°C) at 130.1°E for Experiment 4 day 42, with a contour interval of two degrees. 56

Figure 14e. Cross-section of east-west velocities (m/s) at 131°E for Experiment 4 day 42, with a contour interval of 10 cm/s. Red is westward. 57

Figure 14f. Cross-section of temperature (°C) at 38°S for Experiment 4 day 42, with a contour interval of two degrees. 58

Figure 14g. Surface temperature (°C) and velocity vectors for Experiment 4 on day 60. .59

Figure 14h. Cross-section of temperature (°C) at 130.1°E for Experiment 4 day 60, with a contour interval of two degrees. 60

Figure 15a. Surface temperature (°C) and velocity vectors for Experiment 5 on day 21. The 200m isobath is shown. 61

Figure 15b. Surface temperature (°C) and velocity vectors for Experiment 5 on day 60. The 200m isobath is shown. 62

Figure 15c. Cross-section of north-south velocities (m/s) at 30.7°S for Experiment 5 day 60, with a contour interval of 10 cm/s. Red is equatorward (north). 63

Figure 15d. Cross-section of east-west velocities (m/s) at 129.4°E for Experiment 5 day 60, with a contour interval of 5 cm/s. Red is westward. 64

Figure 15e. Cross-section of north-south velocities (m/s) at 30.7°S for Experiment 5 day 60, with a contour interval of 10 cm/s. Red is equatorward (north). 65

Figure 15f. Cross-section of north-south velocities (m/s) at 38.3°S for Experiment 5 day 60, with a contour interval of 5 cm/s. Red is equatorward (north). 66

Figure 16a. Surface temperature (°C) and velocity vectors for Experiment 6 on day 24. .67

Figure 16b. Surface temperature (°C) and velocity vectors for Experiment 6 on day 30. .68

Figure 16c. Surface temperature (°C) and velocity vectors for Experiment 6 on day 48. .69

Figure 17a. Surface temperature (°C) and velocity vectors for Experiment 7 on day 24. The 200m isobath is shown. 70

Figure 17b. Surface temperature (°C) and velocity vectors for Experiment 7 on day 60. The 200m isobath is shown. 71

Figure 17c. Cross-section of north-south velocities (m/s) at 28.9°S for Experiment 7 day 60, with a contour interval of 5 cm/s. Red is equatorward (north). 72

Figure 17e. Cross-section of temperature (°C) at 28.9°S for Experiment 7 day 60, with a contour interval of 2.5 degrees. 74

Figure 17f. Cross-section of east-west velocities (m/s) at 123°E for Experiment 7 day 60, with a contour interval of 10 cm/s. Red is westward. 75

Figure 17g. Cross-section of east-west velocities (m/s) at 129.4°E for Experiment 7 day 60, with a contour interval of 10 cm/s. Red is westward. 76

Figure 17h. Cross-section of temperature (°C) at 130.1°E for Experiment 7 day 60, with a contour interval of one degree. 77

Figure 17i. Cross-section of north-south velocities (m/s) at 38.3°C for Experiment 7 day 60, with a contour interval of 5 cm/s. Red is equatorward (north). 78

Figure 18a. Satellite image of surface water temperatures off Western Australia in April 2001, showing the warm waters of the Leeuwin Current (red/orange) and the cooler offshore water in green/blue. The white and mottled blue areas are clouds, and the black line represents the edge of the continental shelf (CSIRO, Marine Research). 79

Figure 18b. Satellite image of surface water temperatures in the Great Australian Bight in August 2002, showing the relatively warmer waters of the Leeuwin Current (green) and the cooler offshore water in blue. The white and mottled blue areas are clouds, and the black line represents the edge of the continental shelf (CSIRO, Marine Research). 80

LIST OF TABLES

Table 1. Summary of experimental design. 81

Table 2. Vertical levels and depths used by Levitus and Boyer (1994) and Levitus et al. (1994) 82

Table 3. Values of sigma levels 83

THIS PAGE INTENTIONALLY LEFT BLANK

ACKNOWLEDGMENTS

I would like to thank Professor Mary Batteen, my advisor, for helping me to complete this study. Her enthusiasm, support and guidance were invaluable throughout the last nineteen months. I was very grateful to be able to work on an area that was close to home. I would also like to thank Professor Curt Collins for his thoughtful input and advice as my second reader. For numerical modeling and Macintosh advice, I would like to thank Dr. Don Stark. Thank you to Antonio Martinho for his love of computer programming and for the many hours of assistance he has given with MATLAB and the Princeton Ocean Model. I owe you an espresso or two. Thanks also to Kitch Kennedy. Together we struggled through the initial steps and it would have been more difficult were it not for the cooperative effort. A very big thank you goes to my good friend Kristen Watts for looking after me towards the end and for helping to fulfill the spousal duties that Al was unable to complete.

Most importantly, I would like to thank my wonderful husband, Al Byrne, who let me live on the other side of the world for one year, nine months, eighteen days and seven hours so that I may follow my dreams.

THIS PAGE INTENTIONALLY LEFT BLANK

I. INTRODUCTION

The Leeuwin Current is a thermally driven, anomalous, surface eastern boundary current (EBC). It flows poleward over the continental shelf break (~200 m) off the coast of western Australia to Cape Leeuwin (see Figure 1) and then eastward into the Great Australian Bight (Cresswell and Golding, 1980). There is general agreement (Godfrey and Ridgway, 1985) that the Leeuwin Current is generated by a meridional pressure gradient resulting from the large amount of heating in the equatorial region and excessive cooling near the poleward region that overwhelms the equatorward wind stress. The source for the Leeuwin Current is predominantly an alongshore steric height gradient due to tropical Pacific water from the Indonesian throughflow (Godfrey and Ridgway, 1985; Hirst and Godfrey, 1993), augmented by geostrophic inflow from the west (McCreary et al., 1986; Thompson, 1987). As a result of this strong inflow of subtropical water towards the coast, the Leeuwin Current intensifies poleward (Batteen et al., 1992). The Leeuwin Current flows most predominantly but not exclusively in the austral autumn and winter (Church et al., 1989). The surface poleward current along the Australian west coast is weakest and shallowest between November and January when the equatorward wind stress is at a maximum, with the period of strongest and deepest flow between March and May when the equatorward wind stress is at a minimum.

The Leeuwin Current is unlike other subtropical EBCs. The major subtropical EBCs such as the California, Canary, Peru, and Benguela Currents are wind-driven and characterized by climatologically weak (<10 cm/s), broad (~1000 km wide), cold surface flows towards the equator in the direction of the prevailing winds, a poleward undercurrent, a shallow thermocline (<30 m depth) and high biological production due to vast regional upwelling (Parrish et al., 1983). Observational studies along the coast of western Australia have shown that the Leeuwin Current is characterized by a strong (>150 cm/s at times), narrow (<100 km wide), poleward surface current that flows opposite the prevailing wind direction (Cresswell and Golding, 1980; Godfrey et al., 1986), anomalous warm water at the surface, a deep thermocline (>50 m depth)

(Thompson, 1984), and lower biological production due to vast regions of downwelling (Batteen et al., 1992).

Below the Leeuwin Current, an anomalous equatorward undercurrent is present off western Australia (Church et al., 1989). Smith et al. (1991) stated that the speed of the undercurrent can reach ~30 cm/s between ~250 m and 350 m depth and observed that current meter data from the Leeuwin Current Interdisciplinary Experiment (LUCIE) showed the equatorward current to be narrow and confined to the continental slope between ~250 m and 450 m depth. Although there is evidence of a westward flow of ~20 cm/s centered between ~400 m and 700 m depth off the southern coast at ~116° E (Cresswell and Peterson, 1993), no studies to date have clearly resolved whether there is a westward undercurrent in this region.

The Leeuwin Current enters the Great Australian Bight from the west during late autumn (Herzfeld and Tomczak, 1997) and progresses eastward along the continental shelf break as far as the central Bight (130°E). Church et al. (1989) hypothesized that the current could extend across to Portland (142°E). This eastward component of the Leeuwin Current is weakest during the austral spring and summer, correlating with the time of the weakest poleward current along the west coast. Circulation within the continental shelf of the Great Australian Bight is mainly wind-driven (Bye, 2002). Summer heating of the western Great Australian Bight creates a warm pool of water that advects eastward, inshore of the continental shelf break (Herzfeld, 1997). This warm Great Australian Bight water combined with the Leeuwin Current can create a continuous band of warm water across the Great Australian Bight during the winter months.

A poleward current, known locally as the Zeehan Current, exists off the north-west coast of Tasmania (Figure 1). It flows predominantly during the austral winter at speeds up to 50 cm/s and ~200 m depth. An equatorward undercurrent is present below the Zeehan Current with a speed that can reach ~10 cm/s (Middleton and Platov, 2002).

Positive wind stress curl exists throughout the year over the South Australian Basin and drives a permanent deep sea anticyclonic gyre (Bye, 2002). The equatorward section of the gyre occurs along the western Tasmanian coast and continues westward along the continental slope (Figure 1). The current, known as the Flinders Current, can

exist during both summer and winter (Middleton and Cirano, 2001) and can typically be found between depths of 400 to 600 m, although it can extend up towards the surface and down to depths greater than 800 m. The current is weakest in the east near Portland (~5 cm/s) and stronger in the west near Esperance (>15 cm/s). The Flinders Current is considered a classical western boundary current that exists along a northern boundary. It has been hypothesized to feed the undercurrent to the Leeuwin Current on the west coast of Australia (Middleton and Cirano, 2001).

Previous numerical modeling studies by Batteen et al. (1992) investigated the effects of annual climatological wind forcing and initialized thermohaline gradients on the Leeuwin Current System (LCS), but the study was limited to the coast off western Australia and did not include the influence of topography. Batteen and Butler (1998) examined the effects of continuously forced annual Indian Ocean thermohaline gradients on the LCS and extended the domain to include both the western and southwestern coasts of Australia, as far across as Esperance (122.5°E). Tworek (2000) investigated the effects of seasonal forcing on the LCS with a full primitive equation ocean model but again only considered flat bottom cases. Boedeker (2001) and Kennedy (2002) investigated the role of annual wind forcing, bottom topography and annual thermohaline gradients on the LCS. Both of these studies only included the western coast of Australia and the southern coast as far across as Esperance.

An idealized representation of the Great Australian Bight was modeled to investigate the seasonal cycle of sea surface temperature (Herzfeld and Tomczak, 1997). Middleton and Cirano (2001) used an idealized numerical model to examine the Flinders Current, with simple geometry and topography, and did not include horizontal variations in density. The mean summertime shelf circulation of Australia's southern shelves was examined by Middleton and Platov (2002). The model domain extended from ~120°E across to the western coast of Tasmania and included western Bass Strait. The wintertime shelf and slope circulation was investigated by Cirano and Middleton (2002) over a region extending from ~120°E across to the eastern coast of Tasmania and included the whole of Bass Strait. The latter two studies involved a high resolution numerical model

nested inside of a global circulation model, and incorporated seasonally averaged forcing mechanisms.

This study seeks to extend prior efforts in this area by using a domain that encompasses the western coast of Australia, the Great Australian Bight and the western coast of Tasmania (142.5° E), allowing a better understanding of the LCS. The Princeton Ocean Model (POM), a bottom-following sigma coordinate model, was chosen for this study because it has been widely used to simulate coastal processes associated with continental shelf flows and bottom boundary layer dynamics.

The results of several numerical experiments (Table 1) are explored. Each experiment is run on a beta plane. In Experiment 1 velocity errors produced by the pressure gradient force error, an error inherent in all three-dimensional sigma coordinate models, are determined using horizontally averaged annual climatology with bottom topography and no wind forcing. In Experiment 2 (Experiment 3) the horizontally averaged annual climatology is used with annual wind forcing on a flat bottom (with topography). Experiment 4 (Experiment 5) investigates the effect of thermohaline gradient forcing by using full annual climatology and no wind forcing on a flat bottom (with topography). Experiment 6 (Experiment 7) includes both wind and thermohaline gradient forcing mechanisms on a flat bottom (with topography) to gain an understanding of the combined effect of the forcing mechanisms on the dynamics of the LCS.

Note that the results from experiments with wind forcing only, i.e., Experiments 2 and 3, are more typical of classical EBCs than of the LCS. They are presented to highlight the effect of wind forcing in the absence of a thermohaline gradient. In contrast the final experiment, which includes bottom topography, annual thermohaline gradient and wind forcing, provides the most accurate representation of the LCS.

This study is organized as follows. In section II the numerical model and the specific experimental conditions are described. The results of the numerical experiments are presented in section III, along with a discussion comparing the results to observations. A summary of the study is provided in section IV.

II. MODEL DESCRIPTION

A. DATA SETS

The model domain (Figure 1) encompasses the western and southern coasts of Australia, from 22.5°S to 40°S, and from 107.5°E to 142.5°E. The topographic data of the study region was obtained from the Institute of Geophysics and Planetary Physics, University of California San Diego (Sandwell and Smith, 1996). The data set has a resolution of two minutes (1/30 of a degree) based upon a 30-year compilation of bottom echo soundings by ships. Where the ship data is sparse, altimetry information was used to interpolate soundings.

Annual temperature and salinity values were obtained from Levitus and Boyer (1994) and Levitus et al. (1994). These data sets incorporate a one by one degree horizontal resolution at the vertical levels shown in Table 2.

For wind forcing, climatological wind fields were obtained from the European Centre for Medium Range Weather Forecasts (ECMWF) near-surface wind analyses (Trenberth et al., 1990). The wind data are formulated on a 2.5 by 2.5 degree grid.

All experiments were performed on a beta-plane with a realistic coastline.

B. PRE-PROCESSING

The original topography (Figures 2 and 3) was interpolated to the resolution used in the model, i.e., 13.7 km by 10.2 km offshore, 5.7 km by 10.2 km along the western coast, 13.7 km by 6km along the southern coast and 5.7 km by 6 km around the southwest corner of Australia, with a total of 233 by 298 points. The highest resolution was positioned around the southwest corner of Australia with higher resolution in a north-south band overlapping an east-west band of higher resolution (Figure 4). This was done to minimize the slope parameter (defined by Mellor et al., 1998, as $\frac{|dH|}{2*\overline{H}}$, where $\overline{H}$ is the average depth and dH is the difference in depth between two adjacent cells), which is greatest along the shelf. It was necessary to smooth the topography since over much of

the area the slope parameter was greater than the absolute value of 0.2, which is the suggested maximum value to be used in sigma coordinate models (Mellor et al., 1998).

An improvement on previous models is the introduction of an advanced method to reduce the slope parameter, a one-dimensional robust iterative method (Martinho, 2002). This process has been shown to have the unique advantage of maintaining coastline irregularities, continental shelves, and relative maxima such as seamounts and islands. The first step requires the coastline to be smoothed as large horizontal gradients of the land can cause unwanted instabilities. A two-dimensional (2D) averaging filter is applied to the coastline before the smoothing of the topography to avoid altering the slope parameters after they have been adjusted. The signed slope parameter is then calculated along each grid line in a particular direction over the domain. Where the slope parameter between two adjacent cells is greater than the limit, it is adjusted to the limit value, and then the line is recalculated. When each grid line in the domain has been calculated for that direction, the topography matrix is rotated by 90 degrees and the process is repeated for each direction. This is an iterative process; a change in topography necessary to reduce the slope parameter in one direction may alter the slope parameter in the perpendicular direction to values greater than the limit.

After the smoothing, all depths greater than 2500 m were reassigned to a depth of 2500. Land was assigned a depth of 20 m (to avoid division by zero in the model). The new topography is shown in Figures 5 and 6.

The annual temperature and salinity values were interpolated for the horizontal spatial resolution of the model and for the 21 vertical sigma levels (Table 3 and Figure 7) using a three-dimensional (3D) linear interpolation scheme. The interpolation had to be done separately for the smoothed topography and flat bottom experiments due to the change in vertical levels between these two topographies. The annual temperature and salinity fields at the surface (sigma level one) are shown in Figures 8 and 9, respectively.

The daily seasonal winds were averaged over time in order to obtain the annual non-weighted average wind vector field (Figure 10). The wind vectors were interpolated for the horizontal spatial resolution of the model with a 2D linear interpolation scheme. The components of the wind stress were then calculated.

C. BRIEF MODEL DESCRIPTION

The Princeton Ocean Model (POM), a well documented model (e.g., Blumberg and Mellor, 1987; Mellor, 1996), was used in the model studies. POM is a primitive equation, free surface model with a second moment turbulence closure scheme (Mellor and Yamada, 1982) that, through the use of bottom-following sigma levels, can realistically simulate processes associated with continental shelf flows and bottom boundary layer dynamics in local domains (e.g., bays, estuaries and coastal regions). Recently, the model has been used successfully to simulate decadal processes in entire ocean basins (Ezer and Mellor, 1994, 1997).

As described earlier, the resolution of the horizontal grid varies between a minimum of 5.7 km by 6 km and a maximum of 13.7 km by 10.2 km (Figure 4). The varying grid allows the use of more (fewer) points in regions of large (small) gradients.

The 21 sigma levels used are shown in Figure 7 and Table 3. The sigma values range from zero at the surface to minus one at the bottom with the vertical grid spacing proportional to the ocean depth. The vertical resolution has been chosen to be higher near the surface and the bottom in order to resolve both the surface boundary layer and the bottom boundary layer, which are important in coastal regions. To eliminate the time constraints for the vertical grid related to the higher resolution near the surface, bottom and shallow waters, an implicit vertical time differencing scheme was used.

The prognostic variables of the model are potential temperature, salinity, density, the three components of velocity, surface elevation, turbulent kinetic energy and length scale. The model uses a split time step for the external and internal modes. The external mode solves the equations for the vertically integrated momentum equations. It also provides the sea surface and barotropic velocity components, and has a time step of twelve seconds. The internal mode solves the complete 3D (baroclinic) equations and has a time step of 600 seconds.

A Smagorinsky formulation (Smagorinsky et al., 1965) is used for the horizontal diffusion in which the horizontal viscosity coefficients depend on the grid size, the velocity gradients and a coefficient. In this study a value of 0.2 was assigned to this coefficient, consistent with other POM studies (e.g., Ezer and Mellor, 1997).

D. INITIALIZATION, FORCING AND BOUNDARY CONDITIONS

The model was initialized with annual temperature and salinity values obtained from Levitus and Boyer (1994) and Levitus et al. (1994). Since the model runs reached a quasi-equilibrium state in a relatively short time (~60 days), zero salinity and temperature fluxes were prescribed at the ocean surface. The climatological surface temperature (Figure 8) shows a latitudinal decrease in temperature across the domain. The warmest water can be found next to the coast both along the western and southern coasts. The climatological salinity (Figure 9) shows two local maxima and minima. The first maxima is positioned at the centre of the western edge of the model domain and has a value of ~35.7 psu, and the second can be found around the South Australian Gulfs with a value of ~36.2 psu. The local minima are located to the north of the model domain and to the very south with values of 35.3 psu and 34.9 psu respectively. Note that for the first three experiments, which use horizontally averaged values of annual temperature and salinity, the initial surface temperature and salinity values are 18.5°C and 35.4 psu, respectively.

The model was forced from rest with the annual ECMWF wind fields, which were interpolated for the model grid. Figure 10 shows the wind stress is westerly in the southern region of the model domain, northerly over the Great Australian Bight and south-southeasterly along the west coast. The south-southeasterly winds strengthen with latitude and offshore from the western coast of Australia.

Correct specification of the open boundary conditions is important to achieve realistic results, with no reflections, clamping, spurious currents or numerical alteration of the total volume of water in the model. No general criterion is currently available that can provide the answer to what boundary conditions are the best for a specific model or study. For models with a free surface, such as used here, one of the important criterion is that the boundary conditions should be transparent to the waves. In this model, a gradient boundary condition (Chapman, 1985) that allows geostrophic flow normal to the boundary worked best for the elevation. For the baroclinic velocity components normal to the boundary, an explicit wave radiation scheme based on the Sommerfield radiation condition was used. For inflow situations, the model was forced with annual temperature and salinity values obtained from Levitus and Boyer (1984) and Levitus et al. (1994),

while in outflow situations an advection scheme was used. An advanced volume constraint based on Marchesiello et al. (2001) was also used that reduces the loss of volume at the boundaries to insignificant levels.

For the barotropic velocity components, a Flather radiation plus Roed local solution (FRO) was used. Palma and Matano (2000) showed good results with the FRO solution during boundary condition tests to determine the boundary conditions response to an alongshelf wind stress. Palma and Matano (1998) also showed that the FRO boundary condition demonstrated good reflection properties and results in a test that determined the boundary condition response to the combined action of wind forcing and wave radiation. Their tests were executed with the barotropic version of POM and compared well with benchmark results (no boundary conditions).

THIS PAGE INTENTIONALLY LEFT BLANK

III. RESULTS FROM MODEL SIMULATIONS

A. PRESSURE GRADIENT FORCE ERROR DETERMINATION

In this first experiment, the model was initialized at rest with horizontally averaged annual climatological temperatures and salinities. A realistic coastline and bottom topography were used but no wind or thermohaline forcing was permitted.

With horizontally averaged climatology and no forcing mechanisms, we would expect that nothing will happen, i.e., the initial state of rest should be maintained. Due to pressure gradient force errors, however, this will not be the case and there will be velocities that result from these errors.

Velocity errors induced by the pressure gradient force are unavoidable in 3D sigma-coordinate models. Two types of sigma-coordinate errors exist, the sigma error of the first kind (SEFK) and of the second kind (SESK), as defined by Mellor et al. (1998). The first one goes to zero prognostically by advecting the density field to a new state of equilibrium. The second one, a vorticity error, is the most important because it does not vanish with time, and is present in both 2D and 3D cases.

There are several techniques to reduce the pressure gradient errors:

1. Smoothing the topography can reduce both SEFK and SESK. In particular, the slope parameter should not be greater than the absolute value of 0.2 (Mellor et al., 1998). Greater values can artificially induce currents over 1 m/s.

2. Using the highest possible resolution can reduce the errors, since the pressure gradient error decreases with the square of the horizontal and vertical grid size.

3. Subtracting the horizontally averaged density before the computation of the baroclinic integral reduces the SESK.

4. Using a curvilinear grid that follows the bathymetry reduces the SESK.

This study used the first three techniques. The use of a curvilinear grid was not employed since the first three techniques successfully reduced the error to an acceptable level.

The velocity field for day 10 at sigma level 1 (surface) (Figure 11) shows where the velocity errors are present in the model domain. The maximum velocity errors (~0.004 m/s) are found along the coast where the slope parameter is the greatest. These relatively small velocities are similar to those obtained by Martinho (2001) and indicate that with the use of the three error reduction techniques, the pressure gradient force error has been considerably reduced from values over ~1 m/s to values less than 1 cm/s.

B. WIND FORCING ON A FLAT BOTTOM

In Experiment 2 (see Table 1), the model was initialized with the horizontally averaged annual climatological temperature and salinity. A realistic coastline and flat bottom (constant depth of 2500m) were used, and the model was forced with annual climatological winds. The goal of this experiment was to highlight the role of wind forcing in the Leeuwin Current System (LCS).

As expected, the southerly (northerly) winds along the western (southern) coast have generated an equatorward (westward) surface current along the western (southern) coast (Figure 12c). The surface current is located next to the southern coast and meanders offshore along the western coast.

The equatorward winds along the west coast also induce net offshore surface Ekman transport, generating regions of upwelling evidenced by the cool water along the coast (Figure 12c). Upwelling occurs along the entire western coast of the model domain, although the most intense upwelling is associated with the stronger winds in the north. The coastal upwelling intensifies with time and by day 60 has brought cooler (~16.6°C) water to the surface near Shark Bay (compare Figures 12b and 12d). In addition, the offshore extent of the coastal upwelling has increased with time (e.g., comparing Figures 12a and 12c). As expected, capes and promontories enhance the upwelling regions to the north. Although upwelling is not readily discernible along the southern coast of Australia, slight upwelling is evident along the western Tasmanian coast (e.g., Figure 12g).

A typical cross-section of meridional (zonal) velocity along the western (southern) coast (Figures 12f and 12h, respectively), shows the core of the poleward (eastward) undercurrent at ~150 m (~2500 m) depth with a speed of ~6 cm/s (~2 cm/s), underlying the equatorward (westward) surface current with a core speed of ~6 cm/s (~9 cm/s). Consistent with the planetary beta (β) effect, Figure 12e shows that in time the surface current moves away from the coast, causing the undercurrent to intensify and extend to the surface.

The continued widening of the equatorward coastal jet off the west coast (e.g., compare Figures 12a and 12c) is consistent with the results of McCreary *et al.* (1987) and Batteen *et al*. (1989). They showed that, due to the β effect, the surface coastal jet does not necessarily have to be confined to within a Rossby radius of deformation of the coast. The β effect also allows the existence of freely propagating planetary waves, i.e., Rossby waves (Gill, 1982). The offshore propagation of these waves contributes to the generation of an alongshore pressure gradient field, which can aid the development of sub-surface currents along the eastern boundary. As a result, the β effect changes both the vertical and horizontal structure of the surface and sub-surface currents. As the undercurrent intensifies and shoals, strong vertical and horizontal shear occurs in the upper layers creating baroclinically and barotropically unstable coastal currents. This unstable condition leads to the development of the meanders and filaments evident along the western coast in the model domain.

The results from this experiment resemble the dynamic characteristics associated with classical eastern boundary currents, where wind is the predominant forcing mechanism. Upwelling was produced due to favorable winds; however, these results are not representative of the LCS. Additional experiments will study other factors that distinguish the LCS from other eastern boundary current regions.

C. WIND FORCING OVER TOPOGRAPHY

Experiment 3 (see Table 1) mimics Experiment 2, except that, instead of a flat bottom, topography has been incorporated. A primary goal of Experiment 3 is to

investigate the effects of topographic beta and demonstrate its role in a wind-forced model.

By day 60 (Figure 13a), an equatorward (westward) surface current has developed along the western (southern) coast with speeds of ~60 cm/s (~10 cm/s). Typical cross sections along the western and southern coasts (Figures 13e and 13f respectively) show the core of the surface current centered above the shelf break instead of at the coast, as seen in the flat-bottom case (i.e., Figures 12f and 12h). In Figure 13e (13f) the core of the poleward (eastward) undercurrent is located on the continental slope at ~2400 m (~2400 m) depth with a speed of ~2 cm/s (~3 cm/s). The addition of bottom topography (topographic β) isolates and traps the current along the coast. The balance between the topographic β and planetary β effects is likely responsible for trapping the current over the shelf break. Although the equatorward (westward) surface current is present along the entire western and southern coast of Australia, it is strongest along the west coast of the model domain, as expected due to the stronger winds in this region.

Upwelling is evident near promontories along the entire western coast, although it is not as widespread as in the flat-bottom case (compare Figure 13a with Figure 12c). Consistent with upwelling, relatively cold water ~14°C is discernible at the surface (Figure 13b) and remains trapped over the continental shelf. The deeper upwelling and colder water at the surface in Experiment 3 is consistent with the stronger equatorward current (52.1 cm/s at day 60). The surface elevation in the upwelling regions is lower (Figure 13c) due to the relatively cooler water. The alongshore pressure gradient induces an equatorward, geostrophic current which helps to enhance the wind-forced equatorward surface current. This results in faster velocities than found in the flat-bottom case (Experiment 2). Temperature cross-sections for the north and south west coast (Figures 13b and 13d respectively) show enhancement of upwelling to the north, consistent with the stronger winds to the north. As in the previous experiment, no upwelling is discernible along the southern coast.

This experiment shows that topography can trap and enhance the equatorward surface current. Simultaneously, topography can hinder the development of some upwelling regions (e.g., coastal embayments) even with upwelling favorable winds;

however, in areas where upwelling is present (e.g., off capes) the upwelling can be very intense. Although the results of this experiment are representative of typical eastern boundary current regions, they are not representative of the LCS.

D. THERMOHALINE FORCING ON A FLAT BOTTOM

Experiment 4 (see Table 1) focuses on the thermohaline gradient, which introduces conditions unique to the LCS. The model is initialized with full annual climatology that has not been horizontally averaged. A realistic coastline and flat bottom (constant depth of 2500 m) are used to isolate the combined effect of thermohaline forcing from wind forcing. There is no wind forcing.

In contrast to the previous experiments, a relatively energetic and dynamic current develops (e.g., Figure 14a) with a maximum velocity of ~111 cm/s. The flow is poleward along the entire western coast of Australia, extends eastward around Cape Leeuwin into the Great Australian Bight and continues poleward along the western coast of Tasmania. The strength of the surface current is created by the large alongshore thermohaline gradient, which generates a relatively strong onshore geostrophic inflow. As the inflow nears the coast, it is deflected southward creating a relatively narrow core of warm water along the entire coast of western Australia. As the current rounds Cape Leeuwin, it is steered eastward due to the Coriolis effect (to the left in the Southern Hemisphere).

In addition to strong surface currents, intense undercurrents are established. A typical cross-section of meridional (zonal) velocity along the western (southern) coast (Figures 14c and 14e respectively) show the core of the equatorward (westward) undercurrent at ~500 m (~700 m) depth with a speed of ~30 cm/s (~15 cm/s) underlying the poleward (eastward) surface current with a core speed of ~65 cm/s (~55 cm/s).

The horizontal temperature gradient and the increased strength of the current produce large horizontal shear, resulting in an enhancement of barotropic instability. The relatively strong surface current and the intense undercurrent (e.g., see Figures 14c and 14e) also result in an increase of baroclinic instability. As a result of both barotropic and baroclinic instability, large meanders develop along the west and south-western coast.

Near Cape Leeuwin cold, sub-polar water is entrained west of the main flow resulting in the generation of dipole eddy pairs (e.g., Figure 14g).

Due to the effects of planetary β, the current along the western coast broadens over time. The surface current advects warm (~23°C) water well south of Cape Leeuwin, and advects relatively warm (~18°C) water off the coast in the centre of the Great Australian Bight (Figure 14d).

The generation of a strong, poleward surface current with an equatorward undercurrent is more characteristic of the LCS. The results of the experiment demonstrate the importance of relatively strong climatological thermohaline gradients. While the speed of the surface current is less than observations, the depth and speed of the undercurrent are comparable. Along the northern section of the western coast, however, the model currents are too broad and the eddies are not very well defined.

Between days 42 and 60, current reversals are discernible. At day 42 a cross-section of meridional velocity along the north-western coast (Figure 14b) shows the core of the relatively broad poleward current located offshore with a speed ~12 cm/s. A strong equatorward undercurrent at ~300 m depth with a speed ~15 cm/s extends to the surface inshore of the poleward current. By day 60 (Figure 14g), however, the equatorward current dominates the surface flow with a speed of ~45 cm/s in the northern region. The current reversal has prevented the advection of warm water into the Great Australian Bight, with the coastal surface temperature in the centre of the Bight remaining ~18°C (Figure 14h) by day 60.

A current reversal after day 42 is consistent with the effects of planetary β. As previously noted, the poleward current broadens over time as the planetary β effect widens the current. In time, the poleward current leaves the coast and exists offshore. The equatorward undercurrent subsequently shoals and becomes the dominant surface coastal flow. The results of this experiment by day 60 no longer resemble the LCS, as the surface current is equatorward (due to planetary β effects) rather than poleward.

E. THERMOHALINE FORCING OVER TOPOGRAPHY

Experiment 5 (see Table 1) mimics Experiment 4, except instead of a flat bottom, topography was added. The goals of Experiment 5 are to isolate the effects of topographic β and to demonstrate its role in a thermohaline-forced model.

A poleward (eastward) current has developed by day 60 (Figure 15b) along the west (southern) coast with a maximum velocity of ~89 cm/s located off the south-western corner of Australia. A typical cross-section of meridional velocity along the western (southern) coast (Figures 15c and 15d respectively) shows the core of the poleward (eastward) surface current with a speed of ~45 cm/s (~30 cm/s). The surface current is centered over the shelf break. The core of the equatorward (westward) undercurrent is located over the continental slope at ~500 m (~550 m) depth with a speed of ~7 cm/s (~6 cm/s). Along the western coast of Tasmania, a typical cross section of meridional velocity (Figure 15f) slows the core of a poleward surface current centered over the shelf break with a velocity of ~17 cm/s. The corresponding equatorward undercurrent is located over the continental slope at ~350 m depth with a speed of ~4 cm/s.

The strength of the surface current is created by the large north-south thermohaline gradient. The thermohaline gradient generates a strong onshore geostrophic inflow. As the inflow nears the coast, it is deflected southward creating a narrow core of warm water along the entire coast of western Australia. Coriolis force steers the surface current around Cape Leeuwin and across the Great Australian Bight. Continual onshore flow augments the surface flow throughout the model's duration to enable the surface flow to continue along the entire coast such that poleward surface flow is discernable along the western coast of Tasmania. Relatively warm sub-tropical water is advected by this surface flow such that by day 60, the sea surface temperature in the centre of the Bight has increased by ~1°C to a value of ~19°C (Figure 15e).

The vertical shear caused by the strong, poleward surface current and equatorward undercurrent creates large meanders in the surface current, noticeable by day 21 (Figure 15a), particularly along the western coast. Eddies also develop along the western and south-western coasts, so that by day 60 (15b) there are numerous eddies in different stages of development. Near Cape Leeuwin cold, sub-polar water has been entrained west

of the main flow generating dipole eddy pairs. These detached eddies subsequently propagate westwards as they are no longer under the influence of topography.

The addition of bottom topography (topographic β) isolates and traps the unique thermohaline gradient driven, poleward current all along the coast. Topography aids the development of realistic eddies and dipole pairs, and prevents the undercurrent from becoming the dominant surface current (as observed in Experiment 4). There is also a reduction in the speed of the currents. For example, while the maximum speed of the surface current in the flat bottom case was ~111 cm/s, Experiment 5 never exceeded values of ~89 cm/s. The maximum speeds of the model are expected to be less than observations as the model only uses annual forcing, and seasonal forcing is recognized to play a significant role in the LCS. Overall, the results of this experiment more closely resemble the distinct dynamical features that set the LCS apart from classical eastern boundary currents.

F. WIND AND THERMOHALINE FORCING ON A FLAT BOTTOM

The final flat bottom experiment, Experiment 6 (see Table 1) uses both wind and thermohaline forcing. In particular, the model is initialized with full annual temperature and salinity climatology. A realistic coastline and flat bottom (constant depth of 2500 m) are used. Annual climatological wind forcing is added to determine the net result of both wind forcing and thermohaline gradient mechanisms.

Similar to the flat bottom thermohaline forcing case (Experiment 4), by day 24 (Figure 16a) a warm, poleward (eastward) surface current has developed along the entire western (southern) coast with a maximum velocity of ~99 cm/s. The current is not as strong as in Experiment 4 as the effects of wind and thermohaline forcings tend to oppose each other. Typical cross-sections of velocity and temperature (not shown) contain similar results to those in Experiment 4.

By day 30 (Figure 16b), the poleward surface current has moved offshore (consistent with the β effect), causing the equatorward undercurrent to intensify and extend to the surface. As a result, the surface current is predominantly equatorward along the western coast by day 48 (Figure 16c). The equatorward winds along the western coast

likely enhance the inshore equatorward flow causing the apparent current reversal to occur earlier than in Experiment 4.

The generation of a strong poleward surface current in this experiment at day 24 is characteristic of the LCS. By day 48, however, the subsequent dominating equatorward surface current bares no resemblance to observations in the LCS. This is due to the dominance of the planetary β effect.

G. WIND AND THERMOHALINE FORCING OVER TOPOGRAPHY

The final experiment, Experiment 7 (see Table 1), includes all of the forcing mechanisms and most closely resembles the LCS in the annual sense. In particular, the model is initialized with full annual temperature and salinity climatology. A realistic coastline and bottom topography are used, and the model is forced with annual climatological winds.

A narrow, poleward (eastward) current has developed along the entire coast by day 60 (Figure 17b) with a maximum velocity of ~72 cm/s. A typical cross-section of meridional (zonal) velocity along the western (southern) coast (Figures 17c and 17g respectively) shows the core of the surface current with a speed of ~25 cm/s (~25 cm/s). The surface current is centered over the shelf break due to the trapping effect of topographic β. The core of the equatorward (westward) undercurrent is located over the continental slope at ~500 m (~500 m) depth with a speed of ~15 cm/s (~10 cm/s). Westward intensification of the undercurrent is discernible along the southern coast (e.g., compare cross-sections of east-west velocities from the middle (Figure 17g) and eastern (Figure 17f) ends of the Great Australian Bight). The speed of the undercurrent in the center of the Bight is ~10 cm/s. At the western end of the Bight, the undercurrent has attained a speed of ~15 cm/s.

Along the western coast of Tasmania, a typical cross-section of meridional velocity (Figure 17i) shows the core of a poleward surface current centered over the shelf break with a velocity of ~15 cm/s. The corresponding equatorward undercurrent is located over the continental slope at ~300 m depth with a speed of ~4 cm/s.

In regions where the continental shelf is wider (Figure 17b), such as near 29°S, the main surface current is found to extend as far as ~100 km offshore over the shelf break (e.g., Figure 17c). This allows the wind forcing to dominate the flow inshore of the main current, generating an equatorward surface current directly at the coast. This equatorward flow subsequently leads to localized areas of upwelling distinguished by slightly cooler waters along the coast, as seen by the rising of the temperature contours (Figure 17d) over the shelf.

The strong surface current advects relatively warm sub-tropical water polewards along the western coast and into the Great Australian Bight (Figure 17b). For example, the sea surface temperature increases by ~0.5°C over the first 60 days in the centre of the Bight (~130°E) over the shelf break to a value of ~18.5°C (Figure 17g). By comparing Figures 17g and 15e, it can be seen that there is a larger increase in sea surface temperature in the Bight consistent with the absence of wind forcing in Experiment 5.

The vertical shear caused by the strong, poleward surface current and equatorward undercurrent creates large meanders in the surface current, noticeable by day 24 (Figure 17a), particularly along the western coast. Eddies develop along the western and south-western coasts, so that by day 60 (Figure 17b) there are numerous eddies in different stages of development. Near Cape Leeuwin cold, sub-polar water is entrained west of the main flow generating dipole eddy pairs. Detached eddies propagate westwards as they are no longer under the influence of topography. The wind forcing, which opposes the poleward thermohaline induced current, helps to generate better defined eddies.

The results of this final experiment show relatively realistic features of the LCS including a poleward (eastward) surface current, equatorward (westward) undercurrent, meanders and eddies, as well as regions of localized upwelling. Unlike classical eastern boundary currents, the thermohaline gradients dominate over the opposing wind forcing to drive a poleward (eastward) surface current along the entire coast. The wind forcing influences the development of better defined eddies and enhances the equatorward flow along the western coast in regions where the poleward surface current is further offshore (e.g., off 29°S). Bottom topography is responsible for trapping the currents over the

continental slope and shelf break, thus preventing the equatorward sub-surface current from dominating the surface flow.

H. DISCUSSION

Since Experiment 7 includes all of the forcing mechanisms of the LCS, it is useful to qualitatively compare the final results of the model simulation with observational data to determine if the model developed a current system representative of the LCS. Because the study is not based on actual data but instead is a process-orientated study, direct comparisons to observational data cannot be made; however the dynamics of the model can be investigated to determine if they are qualitatively similar to observations of the LCS.

The results from Experiment 7, day 60 (Figure 17b) will be used in the comparison. The general features of the Leeuwin Current apparent in the satellite images (Figures 18a and 18b) are similar to the results found in the final model experiment. The strong thermohaline gradient creates an onshore geostrophic flow, which then forms a narrow poleward current advecting warm sub-tropical waters southward around Cape Leeuwin and into the Great Australian Bight. The satellite images show evidence of meanders, jets and eddies with varying length scales that are consistent with the model results. Studies have shown that the LCS has large spatial variations due to intensification of instabilities (Batteen and Butler, 1998; Pearce and Griffiths, 1991). Current velocity speeds of ~72 cm/s at day 60 of Experiment 7 are of a similar magnitude, although less than the surface current measurements of greater than 100 cm/s observed by the R/V *Franklin* at Cape Leeuwin (Cresswell and Peterson, 1993). The maximum speeds of the model are expected to be less than observations as the model only uses annual forcing, and seasonal forcing is recognized to play a significant role in the magnitudes of currents in the LCS. Although not apparent from the satellite images, the velocity of the currents along the southern coast compare well with previous studies (Cresswell and Peterson, 1993; Middleton and Cirano, 2001). The westward undercurrent was typically located at a depth of ~500 m with a speed of ~10 cm/s and is representative of the Flinders Current. The results of the model also showed a poleward surface current along the western coast of Tasmania that is consistent with description of the Zeehan Current given by Middleton

and Platov (2002). Overall the model results for this study are supported by their resemblance to both satellite images and previous studies of the LCS.

A final comparison of all the experiments is made to determine the role of each forcing mechanism in generating the LCS. For this comparison the results of all experiments (excluding Experiment 1, the pressure gradient force error) will be analyzed. The obvious dominant forcing mechanism for the LCS is the thermohaline gradient with its strong, poleward component. The gradient sets up an onshore geostrophic flow that is forced into a strong, narrow, poleward surface current as it approaches the coast. The flow is steered down the coast and develops meanders and eddies as it reaches Cape Leeuwin. In regions where the Leeuwin Current leaves the coast, the undercurrent intensifies and extends to the surface, and the wind forcing can enhance the equatorward flow inshore, which is upwelling favorable. The southerly wind opposes the main surface poleward current and generates considerable shear, aiding in the development of better defined eddies.

As the poleward surface current rounds Cape Leeuwin it is steered eastward consistent with the Coriolis effect and extends across the Great Australian Bight, advecting relatively warm sub-tropical water. Although the advection of warmer water does not occur after the Great Australian Bight, the eastward current is discernable at the eastern end of the Bight and continues poleward along the western coast of Tasmania.

While wind and thermohaline forcing are the main driving mechanisms for the current, topography also plays an important role. Without topography, the results from the flat bottom experiments show broad currents, which do not accurately represent the LCS. The planetary β effect is likely responsible for widening the current, and, in some cases, for causing the surface current to be pulled away from the coast. In the flat bottom case, the current is steered by the coastline. The topographic β effect is responsible for trapping the current over the shelf break. The current is steered by the shelf break, and can leave the coast as it follows the shelf break (~200 m depth contour) southward past Cape Leeuwin and eastward into the Great Australian Bight.

A comparison of the wind only experiments, with and without topography, shows that topography reduces the upwelling due to the wind forcing that is present along the

entire west coast in the flat-bottom experiment and enhances localized areas just north of Cape Leeuwin, in an area ~29°S and off Shark Bay (~26.5ºS) The presence of upwelling in these areas is important to the biological productivity of the region, which is important to the fishing and tourism industries.

THIS PAGE INTENTIONALLY LEFT BLANK

IV. SUMMARY

The objective of this process-oriented study was to build on previous studies by using a model domain that encompasses the western coast of Australia, the Great Australian Bight and the western coast of Tasmania (142.5°E), to investigate the roles of wind forcing, thermohaline gradients, and bottom topography in the Leeuwin Current System (LCS). The results of several numerical experiments (see Table 1) using the Princeton Ocean Model (POM), a bottom-following sigma coordinate model, were explored. The POM was chosen for this study because it has been widely used to simulate coastal processes associated with continental shelf flows and bottom boundary layer dynamics. In all experiments a beta-plane was used. The results of Experiment 1 were used to determine the pressure gradient force error created by the addition of bottom topography to the model. Experiment 2 (Experiment 3) investigated the effect of annual wind forcing over a flat bottom (topography). Experiment 4 (Experiment 5) examined the role of annual temperature and salinity gradients over a flat bottom (topography). Experiment 6 (Experiment 7) was run with both annual wind forcing and annual temperature and salinity gradients over a flat bottom (topography).

Experiment 1 was used to determine the pressure gradient force error and was run with no wind or thermohaline gradient forcing. It showed the velocity errors inherent in a sigma coordinate model could be reduced from ~1 m/s to ~0.004 m/s, by day 10, using three techniques. The techniques used were: 1) smoothing the topography, 2) using the highest possible resolution, particularly along the shelf break, and 3) subtracting the area-averaged density before computation of the baroclinic integral. The results showed that the highest velocities induced by the pressure gradient force error were directly related to regions where the slope parameter was the largest, i.e. over the shelf and slope regions.

In Experiment 2 the wind forcing, in the absence of a thermohaline gradient, forced a weak equatorward current. The model results produced classical eastern boundary current features including upwelling, meanders, and along the west coast, a wide surface equatorward current and a poleward undercurrent. Upwelling was evident along the entire west coast of Australia and the western coast of Tasmania, but was most intense near Shark Bay.

Experiment 3 explored the role of wind forcing, without climatology, over bottom topography. Topography had the effect of trapping the equatorward (westward) current along the coast, increasing its maximum velocity when compared to the flat bottom case (Experiment 2). Upwelling was evident along the entire west coast. Although topography limited the zonal extent of upwelling, the intensity of the upwelling was increased. For example, relatively cool water of 14°C was upwelled near Shark Bay.

Experiment 4 removed the wind forcing and introduced temperature and salinity gradients over a flat bottom. Due to the effects of the thermohaline gradient, a strong, broad, poleward (eastward) surface current more characteristic of the LCS developed. A corresponding equatorward (westward) undercurrent was located along the entire coast. Planetary beta (β) effects created westward propagation of the surface current increasing its offshore extent, although by day 42 the current was pulled too far offshore. With the absence of a forcing mechanism at the coast, the equatorward undercurrent intensified and extended to the surface becoming the dominant surface flow along the west coast. Warm, sub-tropical waters were advected southward around Cape Leeuwin and into the Great Australian Bight until the surface current reversed. This experiment also generated meanders and eddies along the western and southern coasts.

In Experiment 5, the thermohaline gradient forcing was isolated over bottom topography. The dominating forcing mechanism in the LCS was found to be the thermohaline gradient, creating a strong poleward (eastward) surface current over the shelf break. A corresponding equatorward (westward) undercurrent was located over the continental slope along the entire coast. Similar to Experiment 3, the addition of topography opposed the planetary β effect and trapped the current along the coast creating a narrow surface current. The shelf break steered the current southward along the western coast, around Cape Leeuwin into the Great Australian Bight and southward along the western Tasmanian Coast. The trapped coastal current had greater instabilities than in the flat bottom experiments resulting in more meanders, offshoots and eddies.

Experiment 6 combined the effects of wind forcing and the thermohaline gradient. The results closely resembled those of Experiment 4, showing that the thermohaline gradient forcing initially establishes a strong, poleward (eastward) surface flow with a

corresponding equatorward (westward) undercurrent along the entire coast. After a period of time, the planetary β effect increases the offshore extent of the surface current and allows the equatorward undercurrent to become the dominant surface flow along the west coast.

Experiment 7 provided the best representation of the LCS because it included wind, temperature and salinity climatology, and bottom topography. In terms of location, this experiment generated the most realistic poleward (eastward) surface current and equatorward (westward) undercurrent along the entire coast. The results of this experiment show that, in an annual sense, the effects of thermohaline gradients dominate and set the system apart from classical eastern boundary currents. The major role of the wind was to slow the speed of the poleward surface current and enhance the generation of eddies. The wind also created localized upwelling regions along the coast where the poleward flow left the coastline. Finally, the wind forcing advected sub-polar water northward, which frequently became entrained by current meanders and subsequently formed the cold core half of dipole eddies. Bottom topography was shown to play an important role in strengthening and trapping the currents near the coast, in intensifying eddies off capes and in preventing the undercurrent from becoming the dominant surface flow.

Overall, Experiment 7, the most complete experiment of the study, compared well with observations and previous studies, and provided the most accurate representation of the LCS. Although, in the annual sense, the wind is an insignificant factor compared to the thermohaline gradient, further research using seasonal winds and seasonal thermohaline forcing is recommended due to the seasonal nature of the observed Leeuwin Current System.

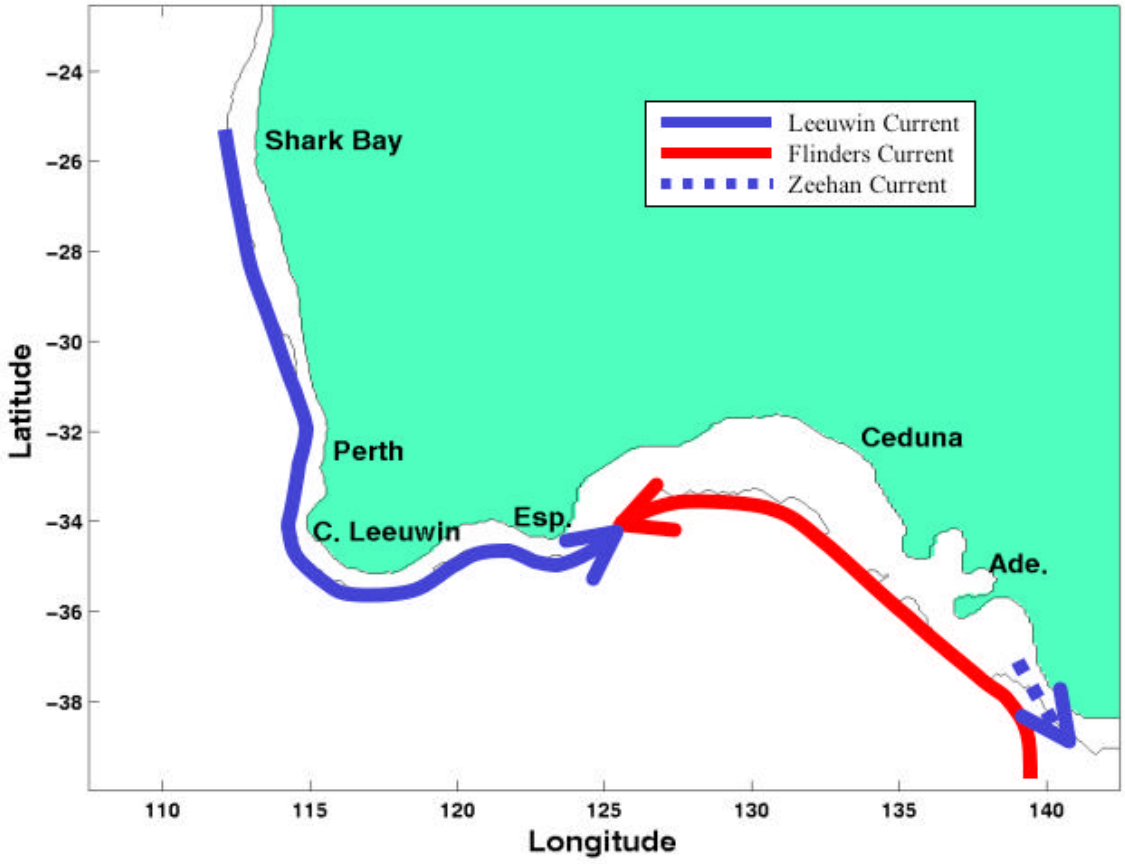

Figure 1. The model domain for the Leeuwin Current System (LCS) is bounded by 40°S to 22.5°S, 107.5°E to 142.5°E. The model domain has a closed boundary along the entire coast and four open boundaries. The 200m isobath is also shown.

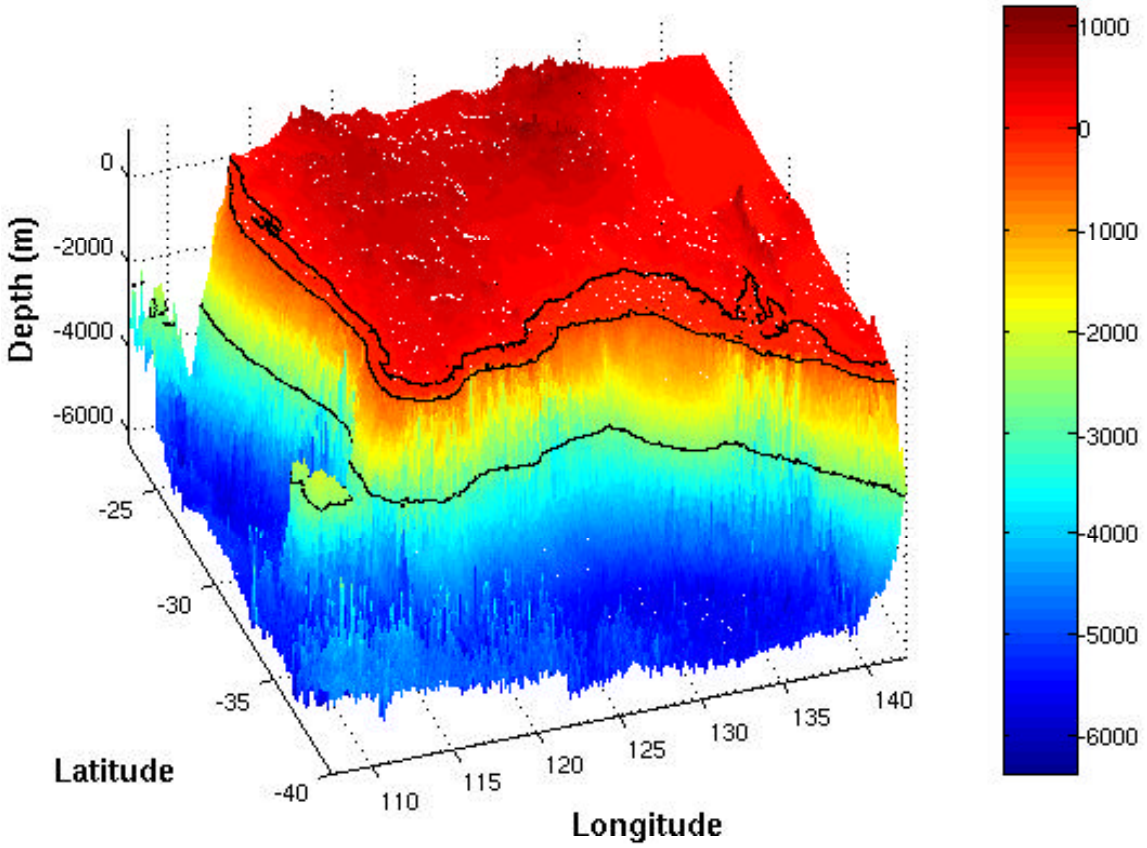

Figure 2. Original topography (meters) in three-dimensions (from Sandwell and Smith, 1996) with a resolution of two minutes (1/30 degree). Contours depict the shoreline, 200m and 2500m isobaths.

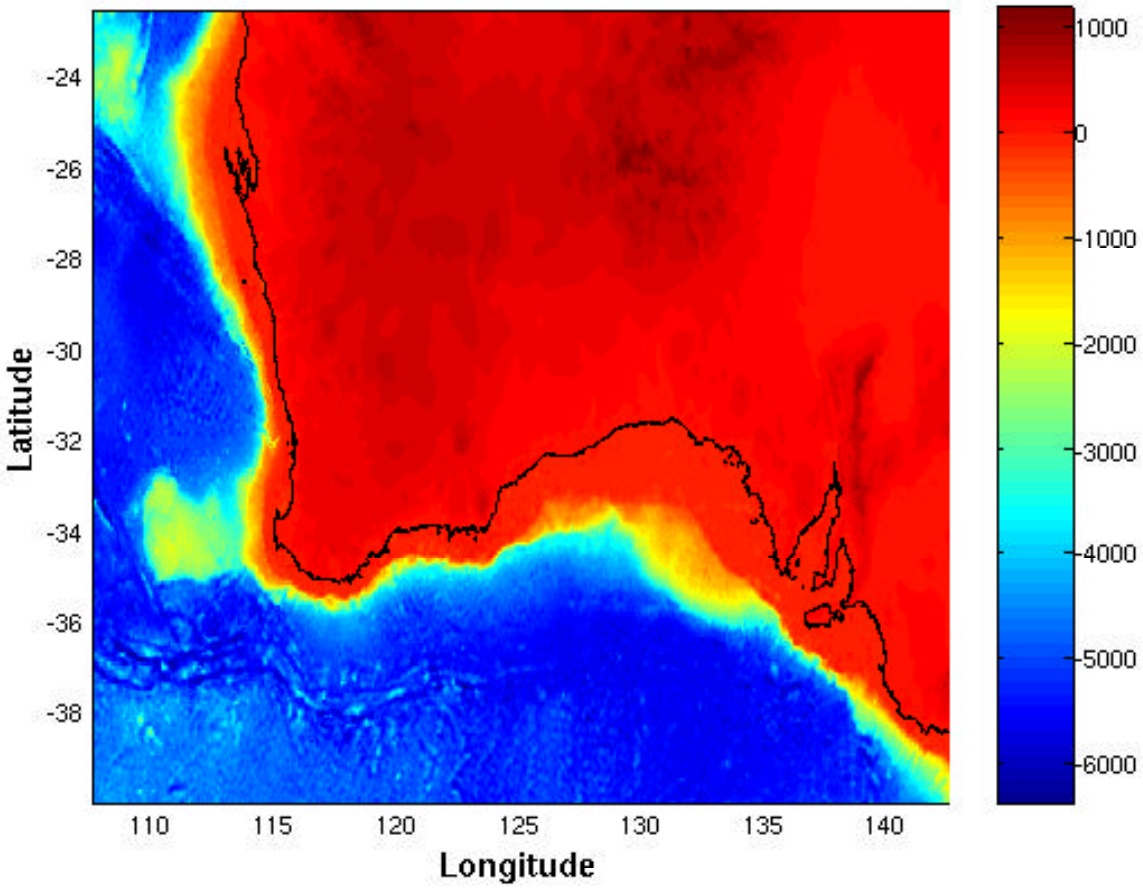

Figure 3. Original topography (meters) in two-dimensions (from Sandwell and Smith, 1996) with a resolution of two minutes (1/30 degree).

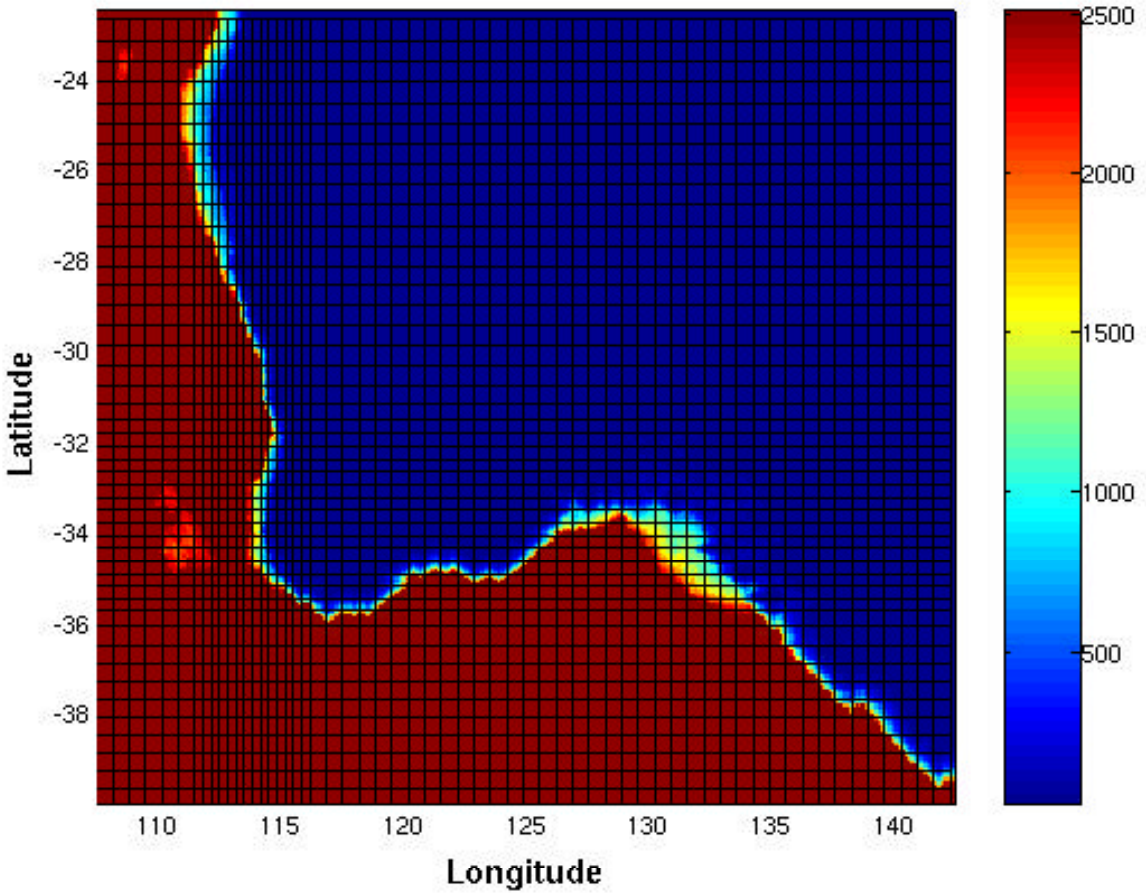

Figure 4. Resolution grid lines with every fifth grid line plotted. (13.7 km by 10.2 km offshore resolution with the highest resolution being 5.7 km by 6 km).

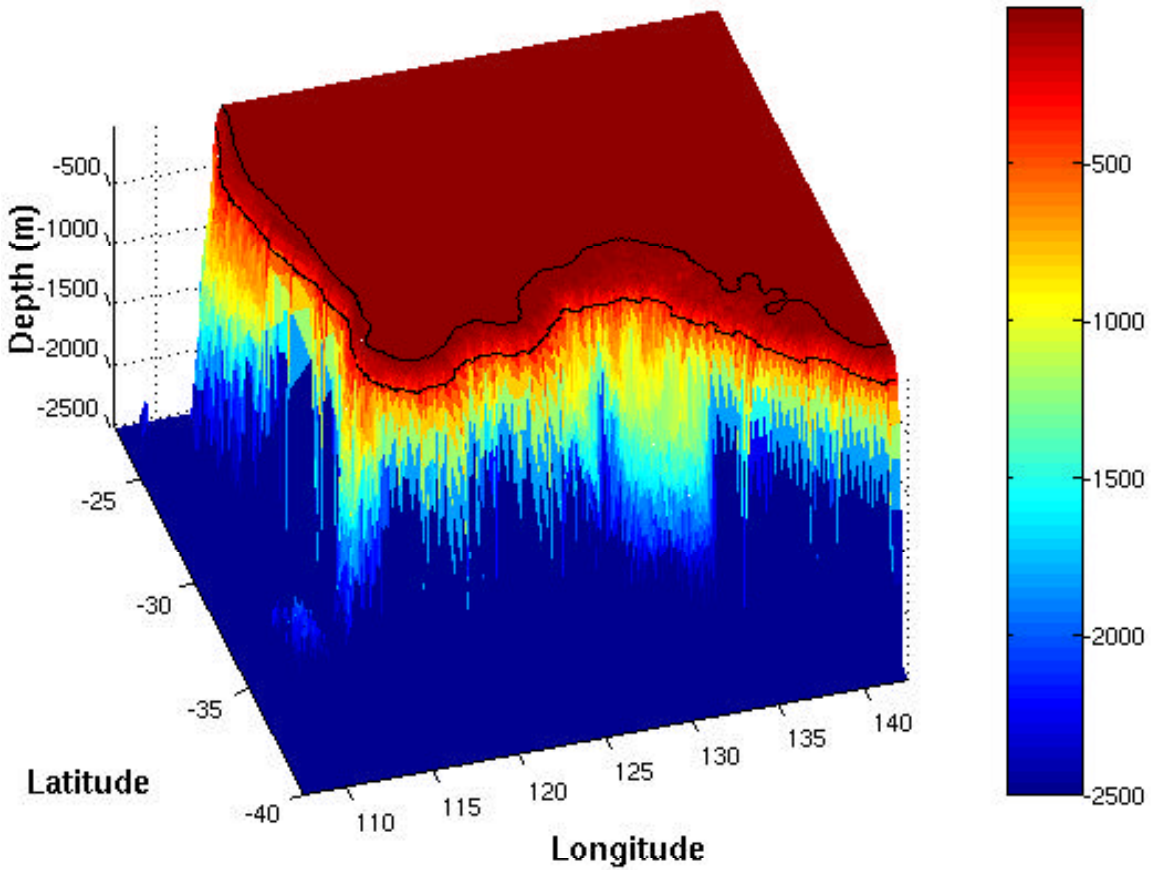

Figure 5. Smoothed topography (meters) obtained after applying a one-dimensional robust iterative method and reassigning depths greater than 2500 m to 2500 m. Contours depict the shoreline and the 200 m isobath.

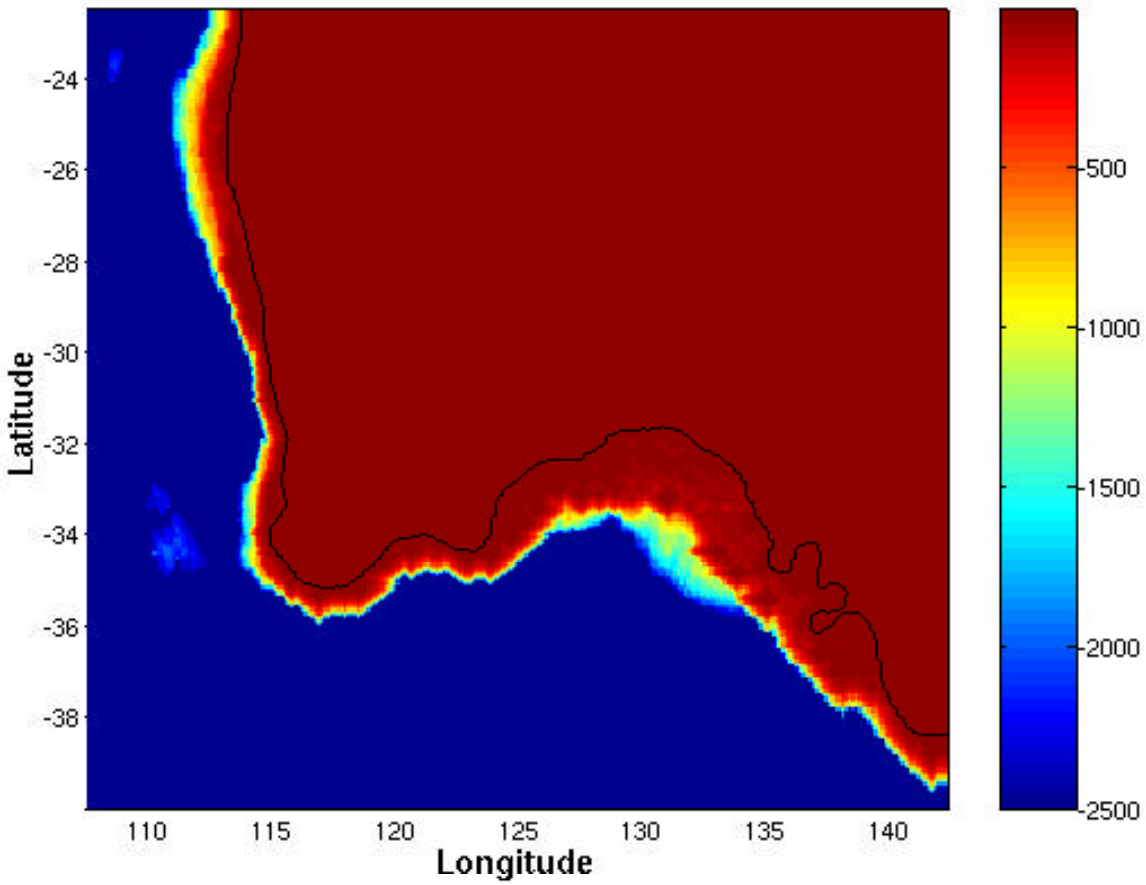

Figure 6. Smoothed topography (meters) in two-dimensions obtained after applying a one-dimensional robust iterative method and reassigning depths greater than 2500 m to 2500 m.

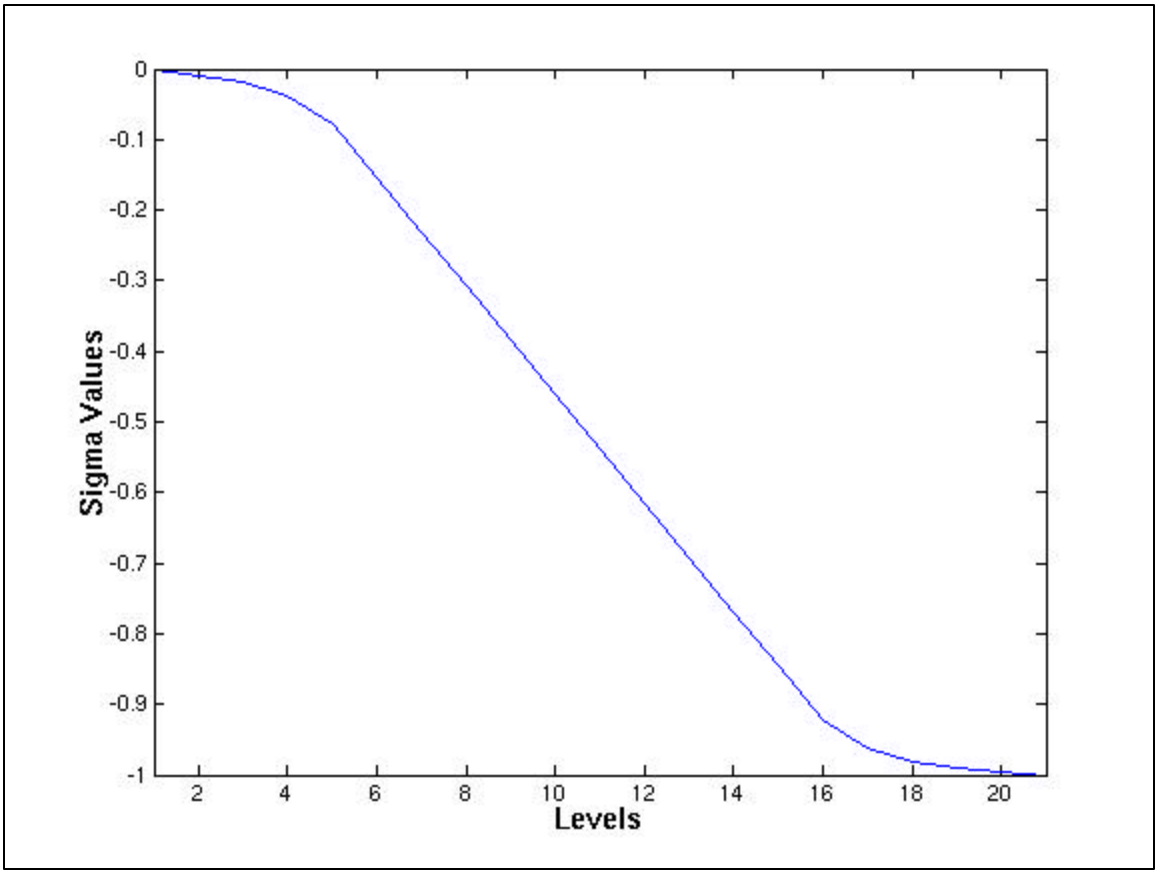

Figure 7. Plot of the 21 sigma levels.

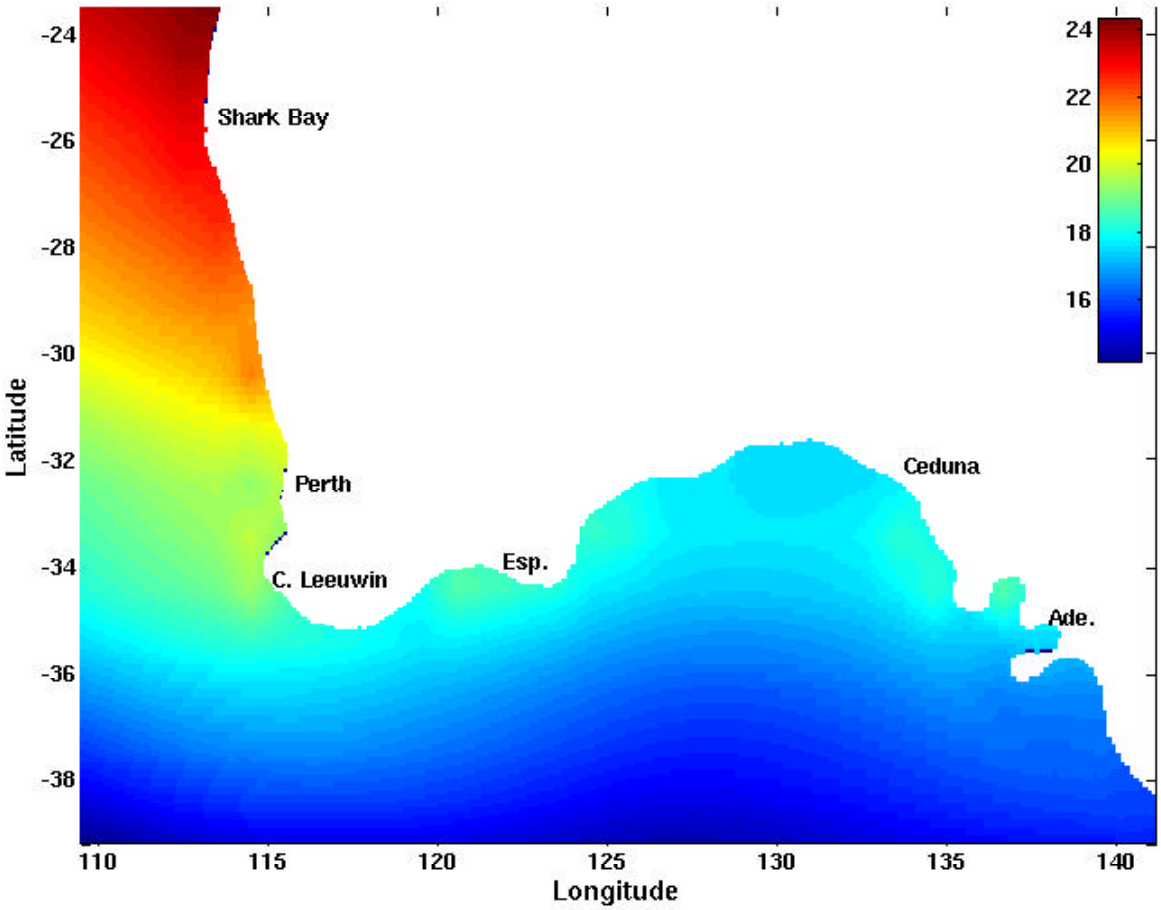

Figure 8. Annual climatological surface temperature (°C) obtained from Levitus and Boyer (1994).

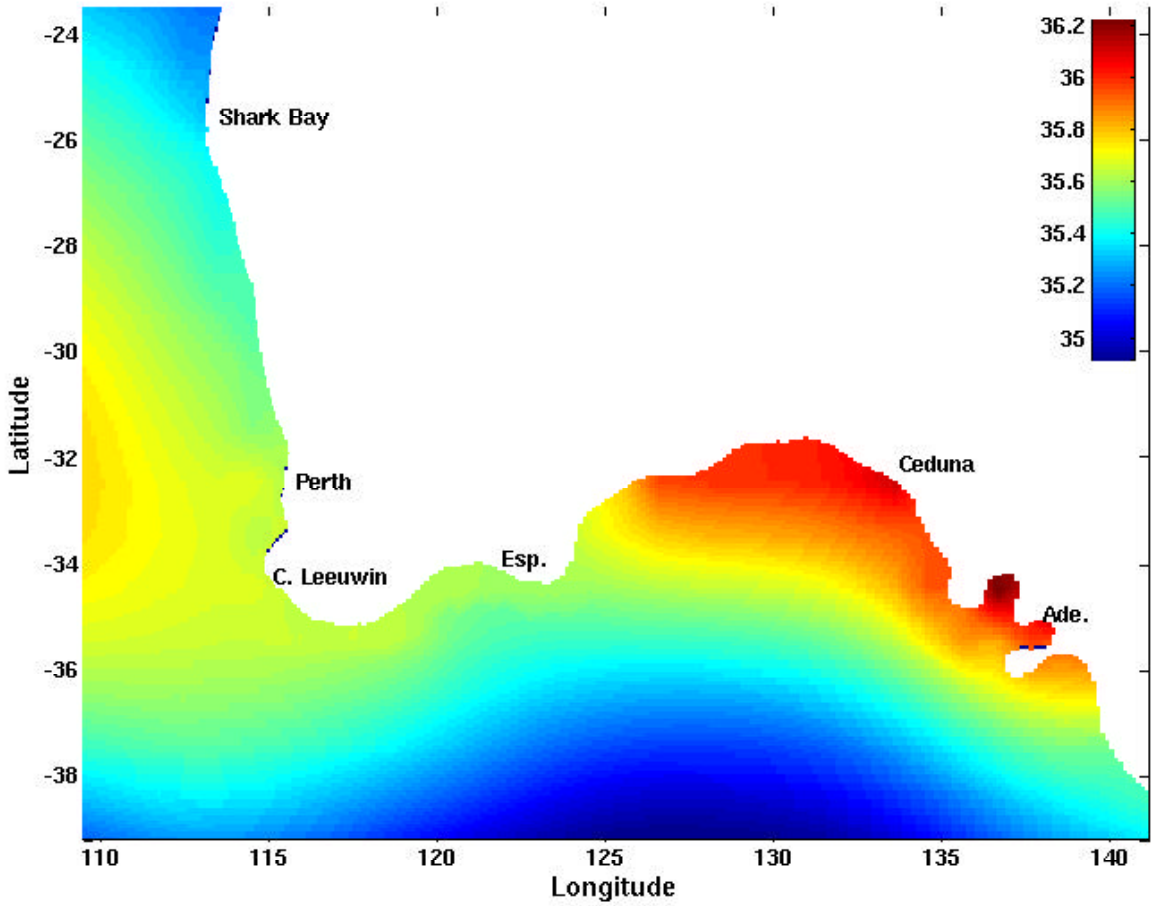

Figure 9. Annual climatological surface salinity from Levitus et al. (1994).

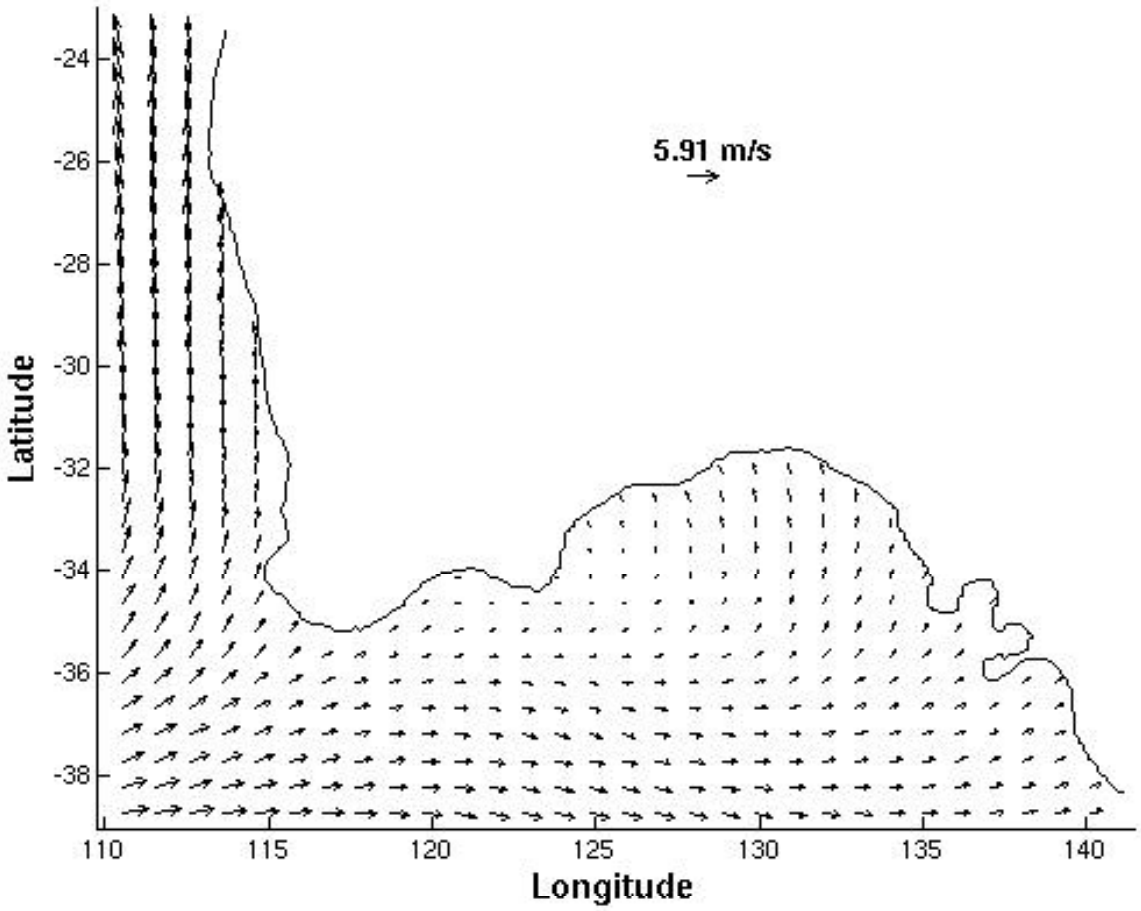

Figure 10. Annual average wind in m/s from climatological ECMWF winds obtained from Trenberth et al., 1990.

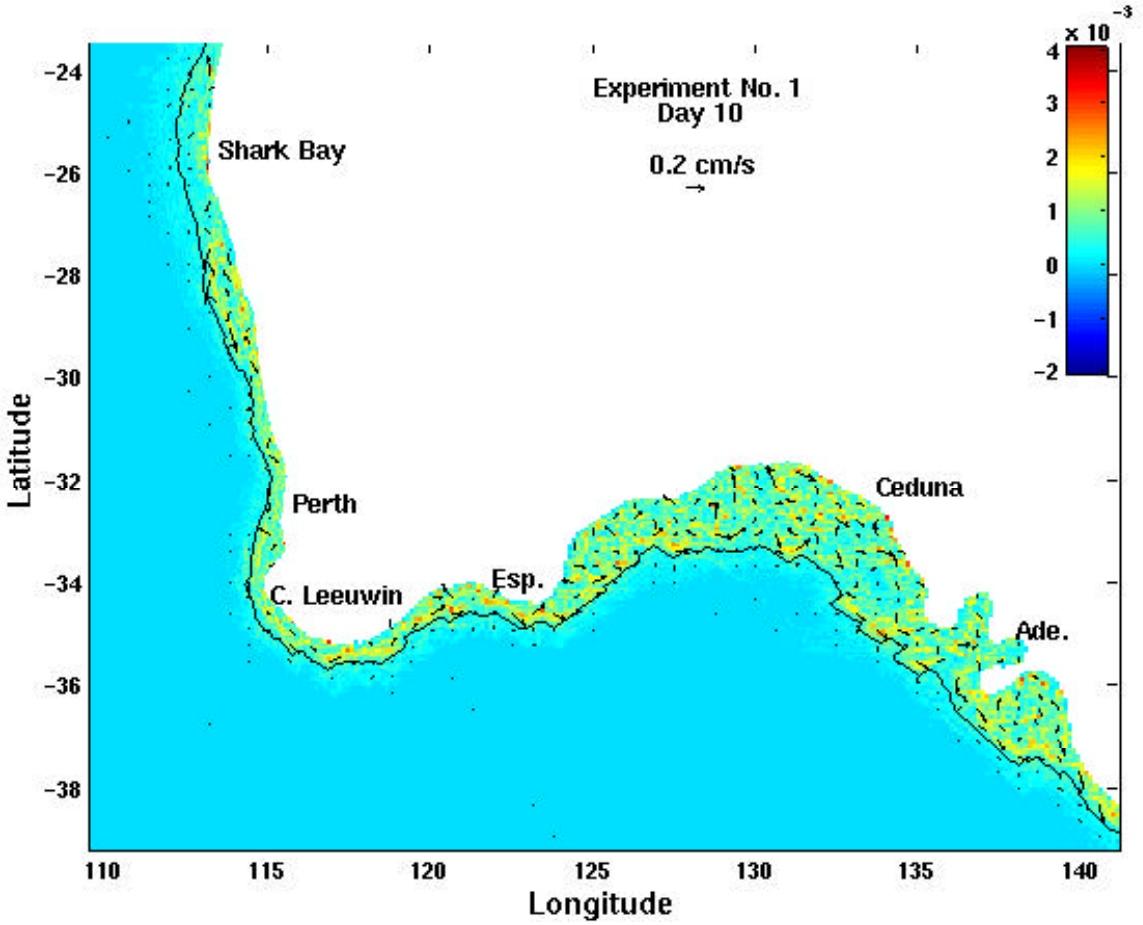

Figure 11. Surface velocity error (cm/s) due to the pressure gradient force error on day 10 for Experiment 1.

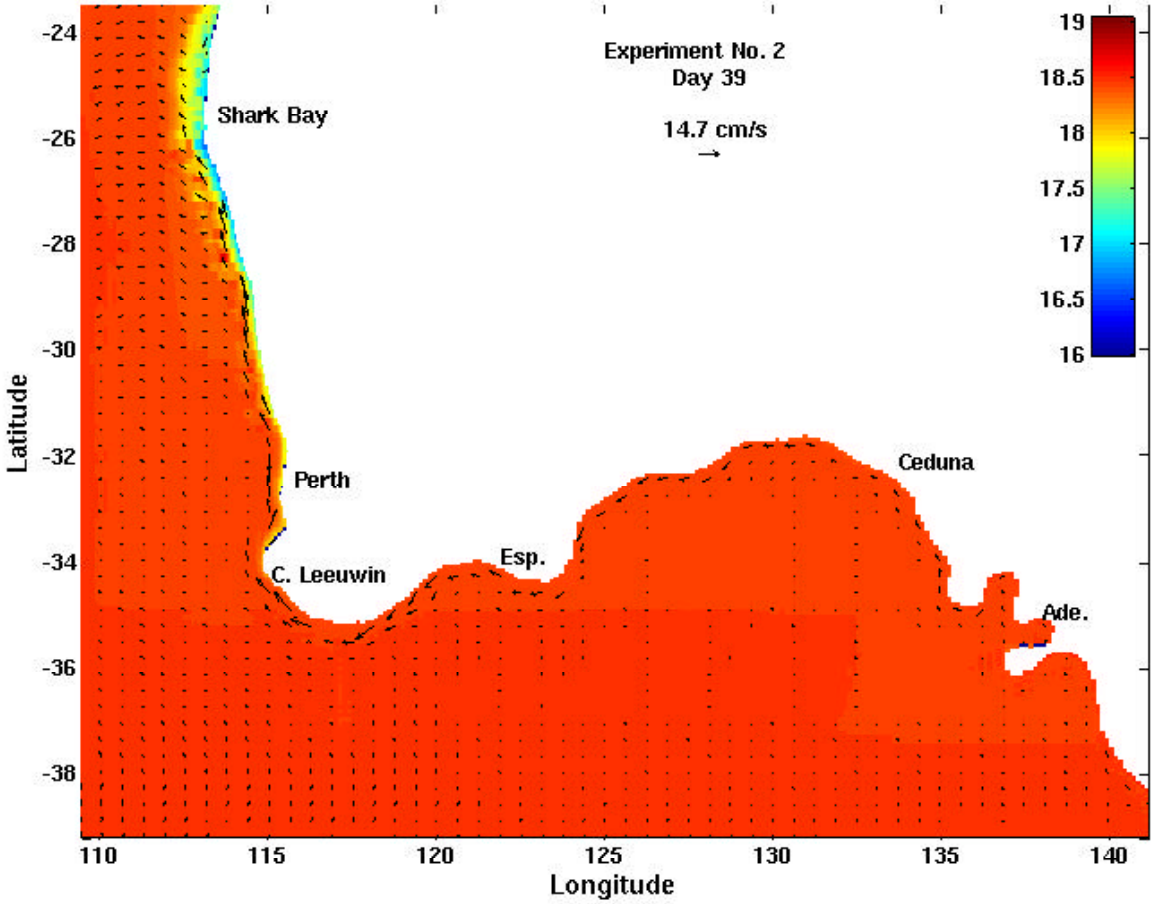

Figure 12a. Surface temperature (°C) and velocity vectors for Experiment 2 on day 39.

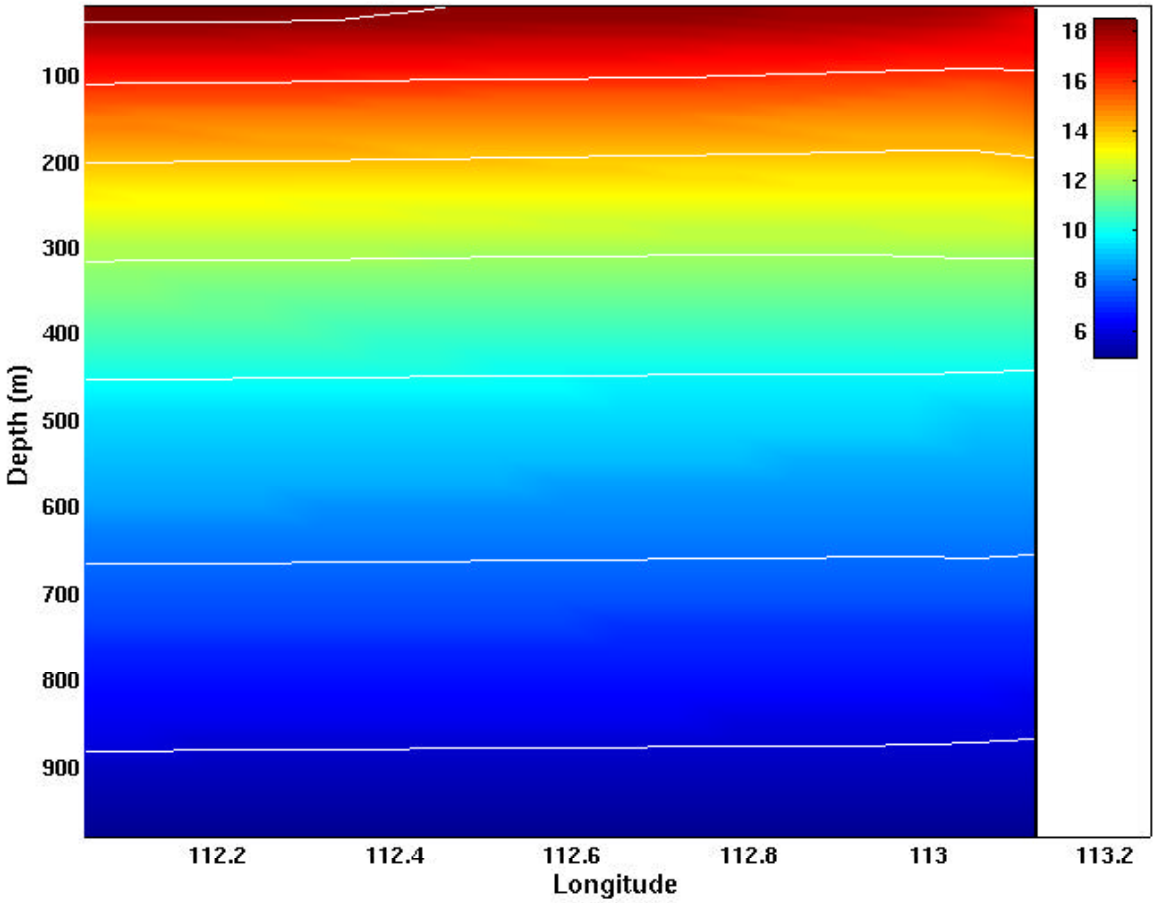

Figure 12b. Cross-section of temperature (°C) at 25.7°S for Experiment 2 day 39, with a contour interval of two degrees.

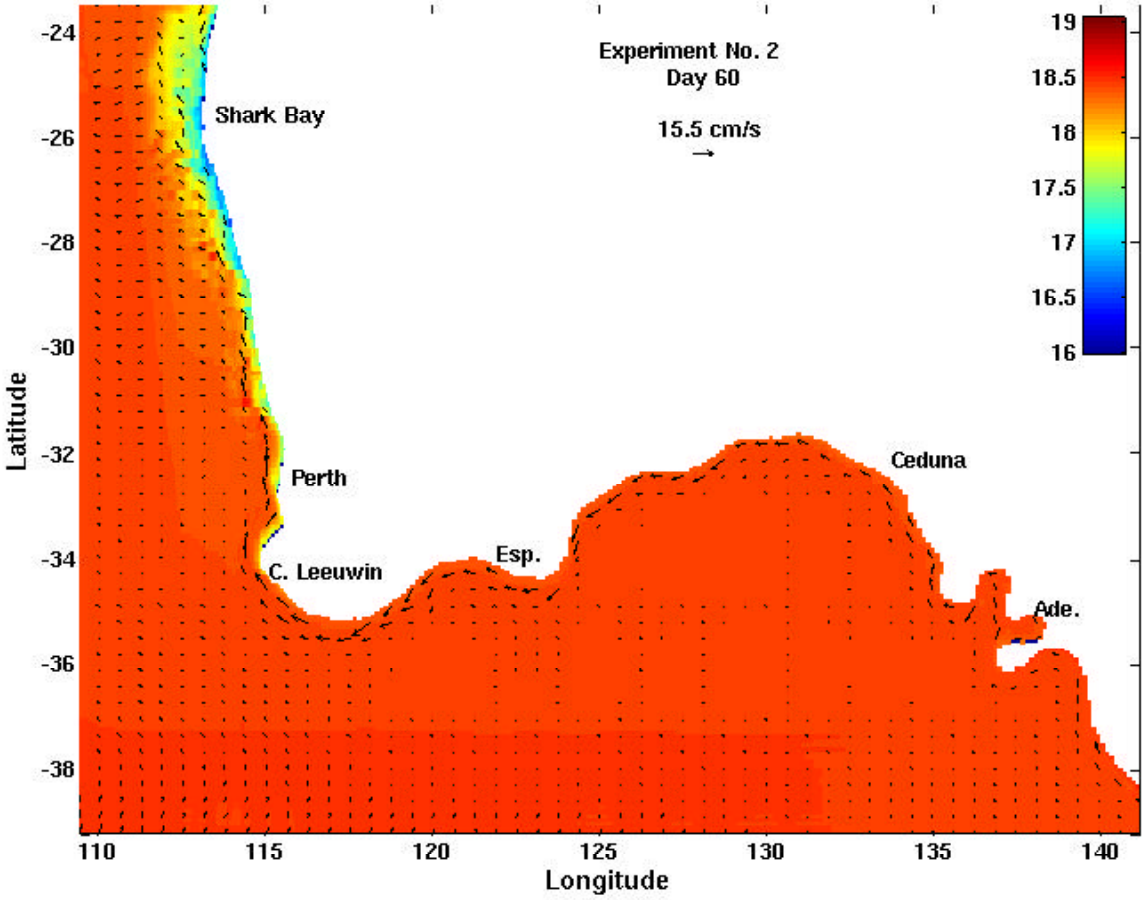

Figure 12c. Surface temperature (°C) and velocity vectors for Experiment 2 on day 60.

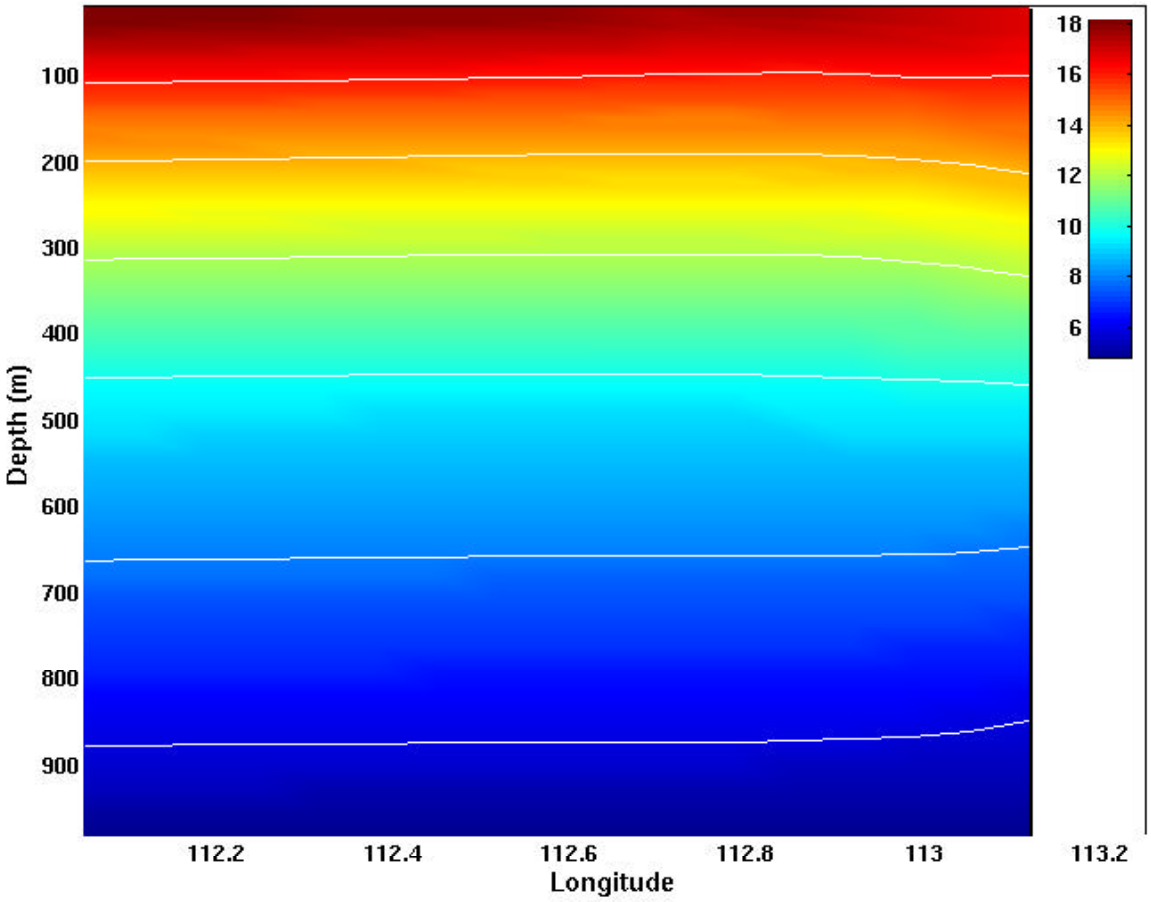

Figure 12d. Cross-section of temperature (°C) at 25.7°S for Experiment 2 day 60, with a contour interval of two degrees.

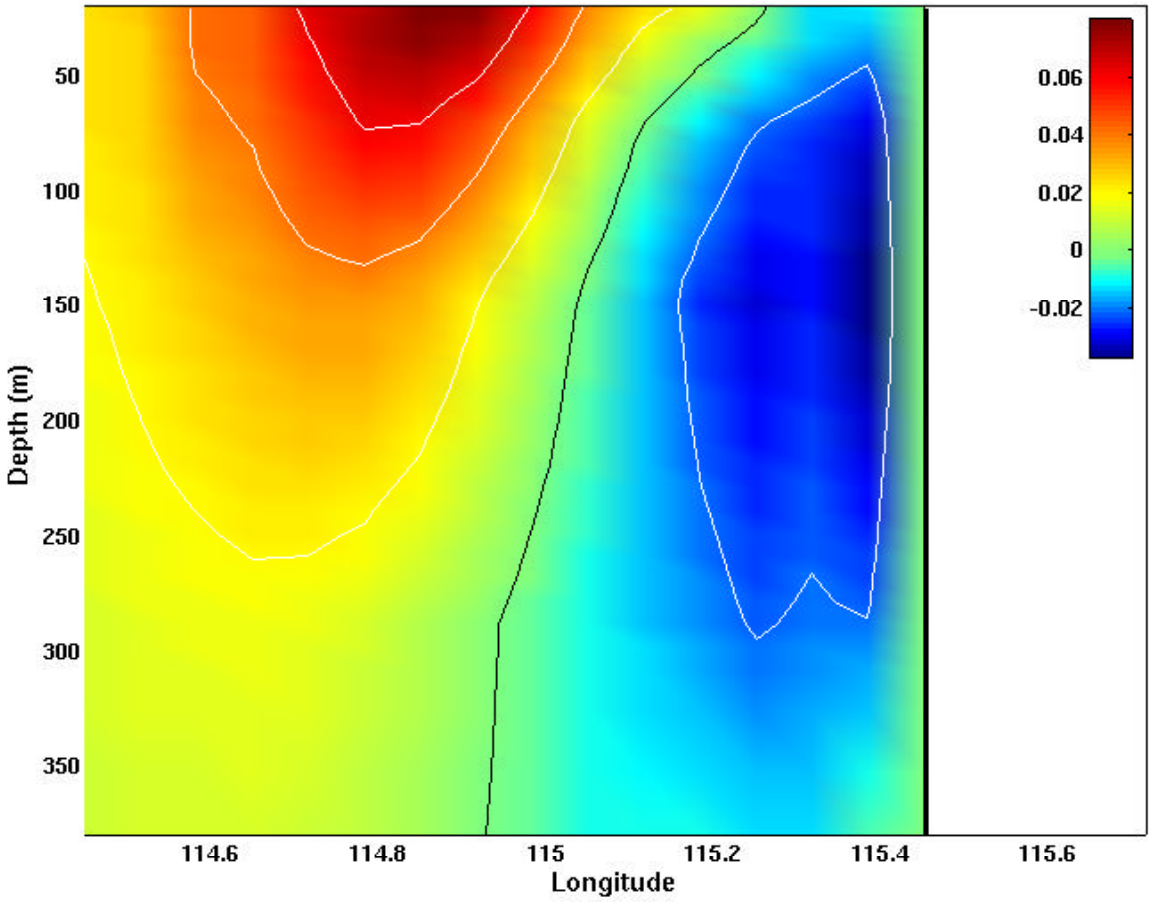

Figure 12e. Cross-section of north-south velocities (m/s) at 33.4°S for Experiment 2 day 60, with a contour interval of 2 cm/s. Red is equatorward (north).

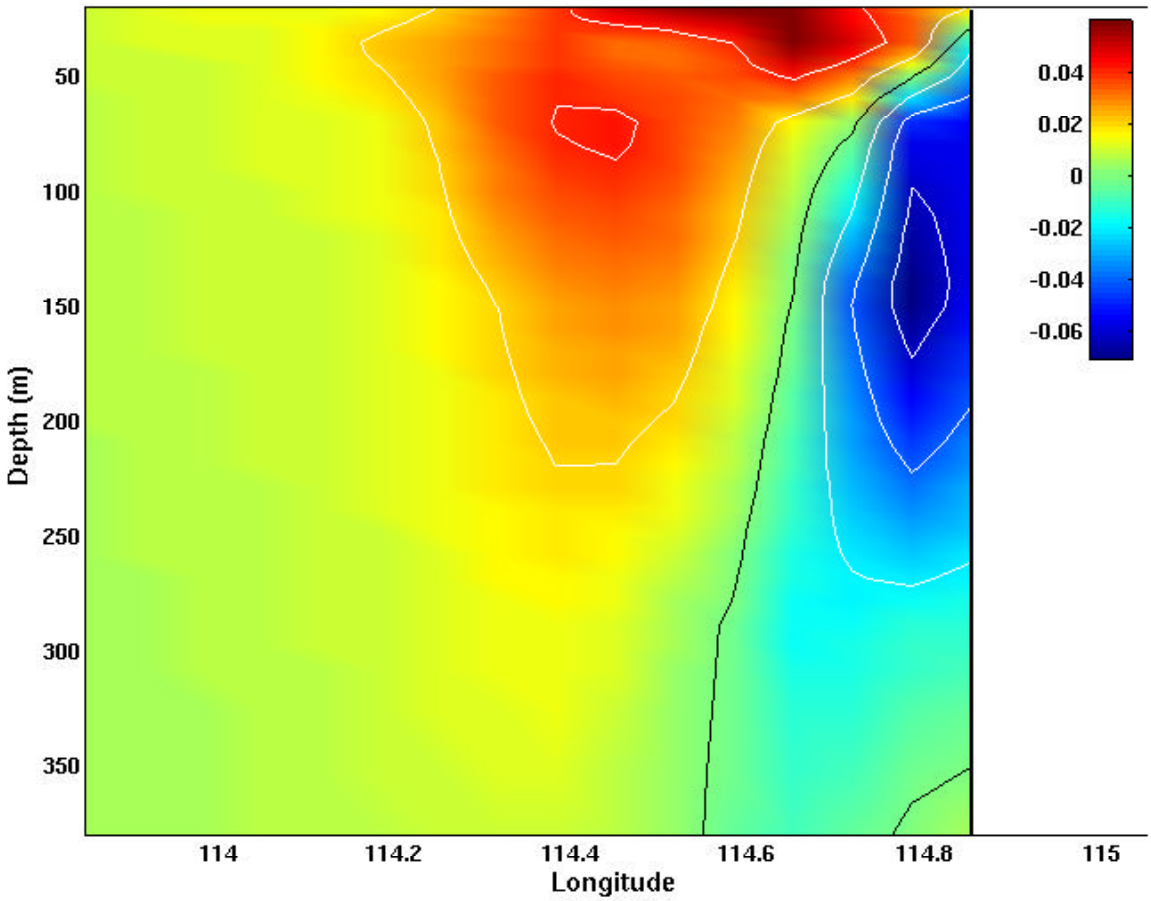

Figure 12f. Cross-section of north-south velocities (m/s) at 30.4°S for Experiment 2 day 60, with a contour interval of 2 cm/s. Red is equatorward (north).

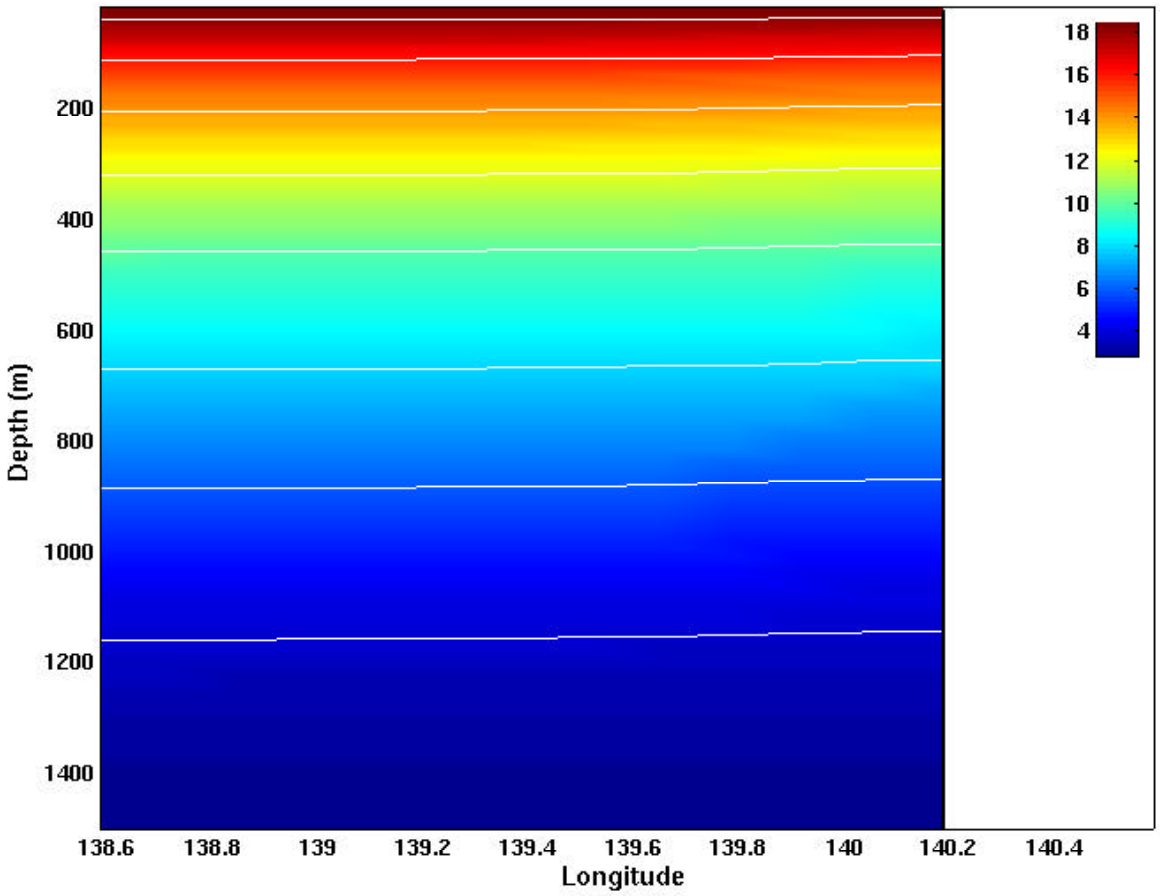

Figure 12g. Cross-section of temperature (°C) at 37.8°S for Experiment 2 day 60, with a contour interval of two degrees.

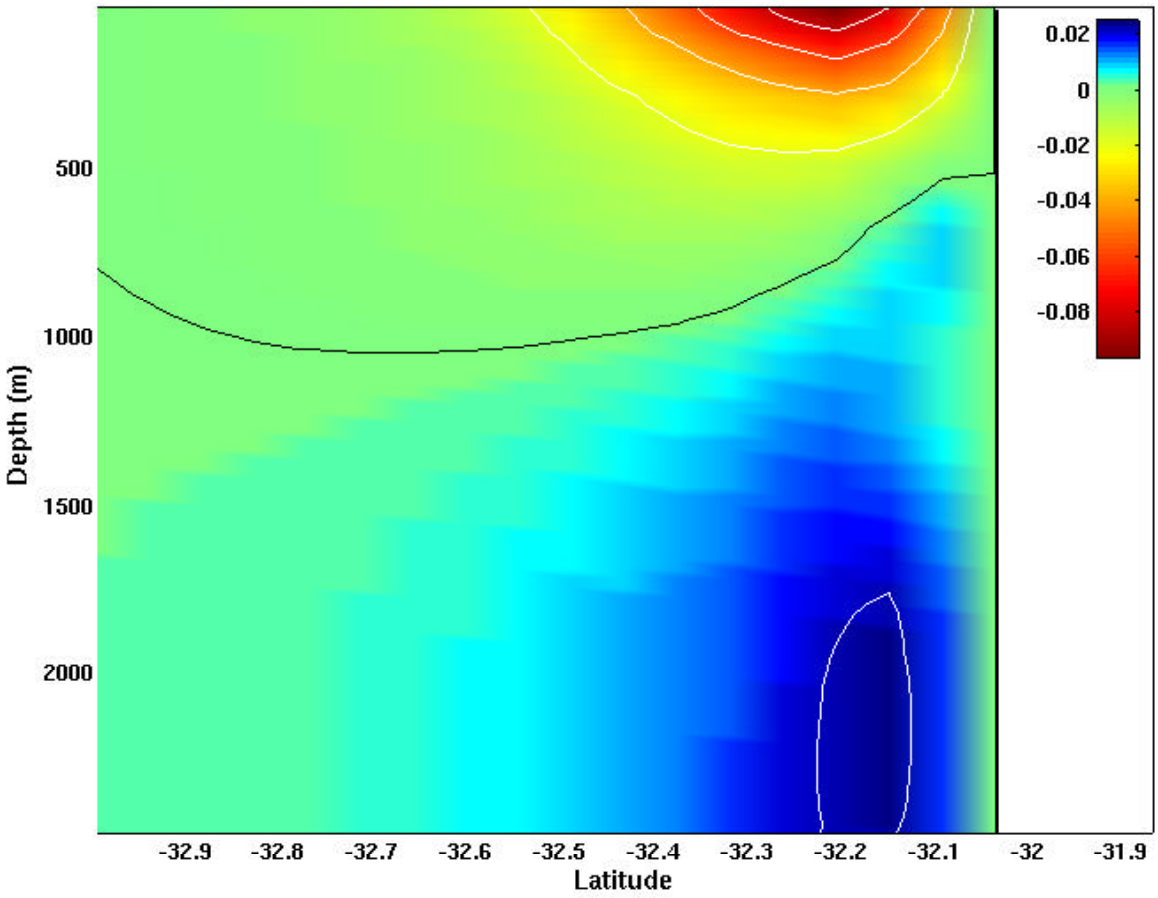

Figure 12h. Cross-section of east-west velocities (m/s) at 128.5°E for Experiment 2 day 60, with a contour interval of 2 cm/s. Red is westward.

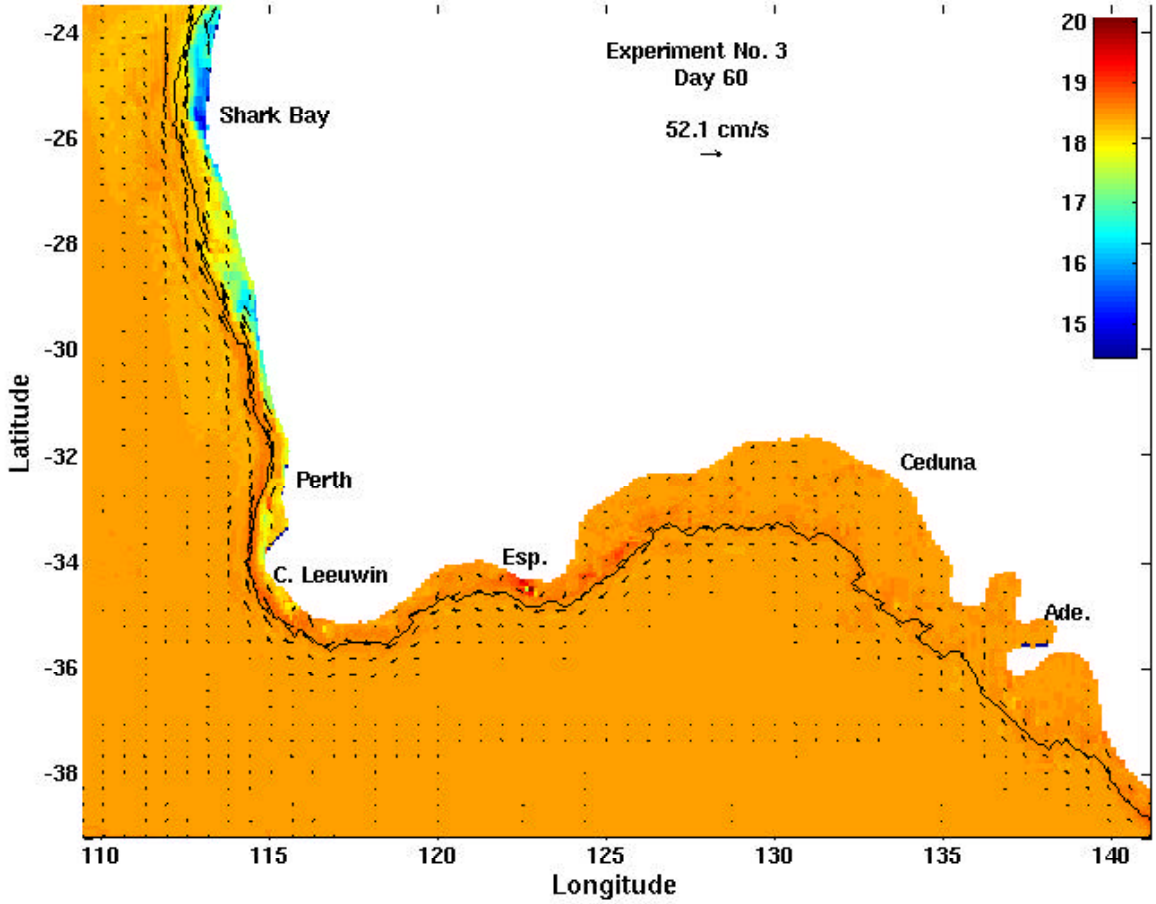

Figure 13a. Surface temperature (°C) and velocity vectors for Experiment 3 on day 60. The 200m isobath is shown.

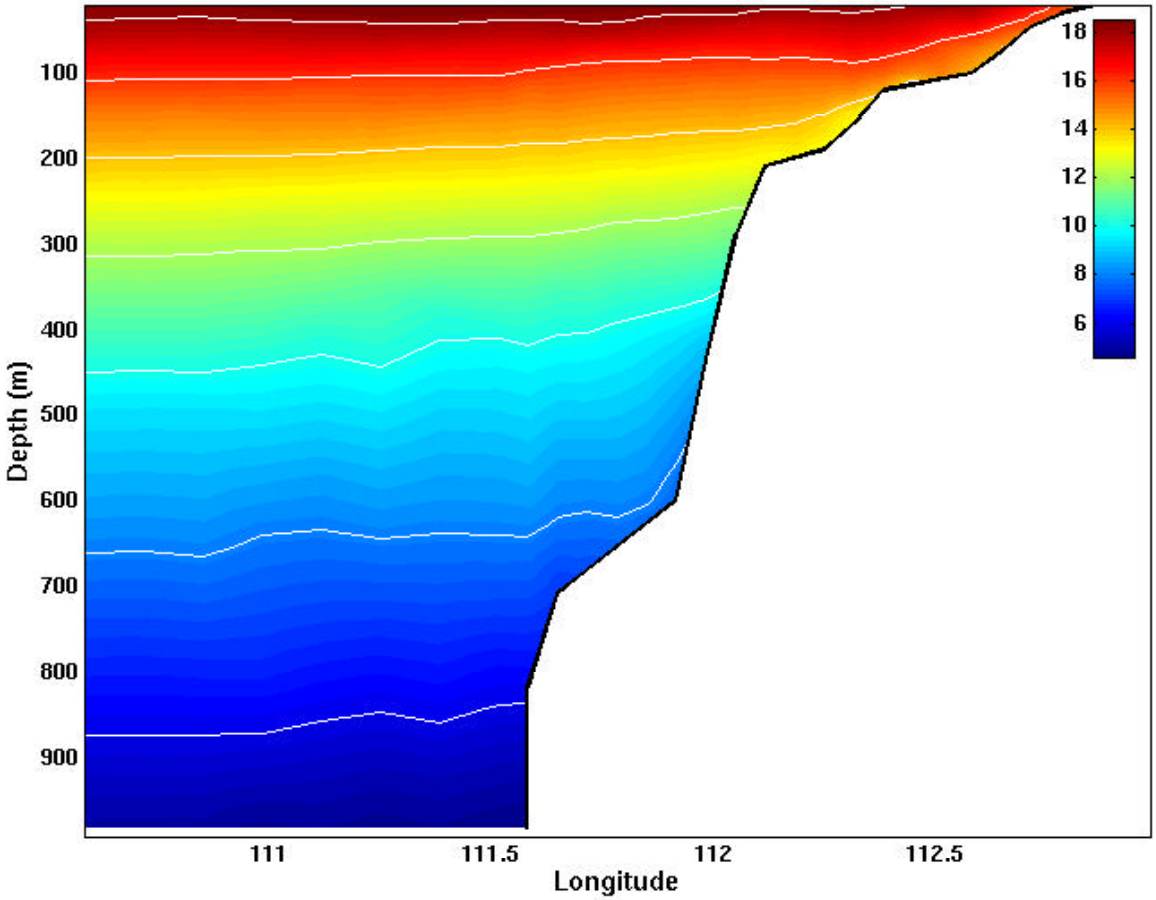

Figure 13b. Cross-section of temperature (°C) at 25.7°S for Experiment 3 day 60, with a contour interval of two degrees.

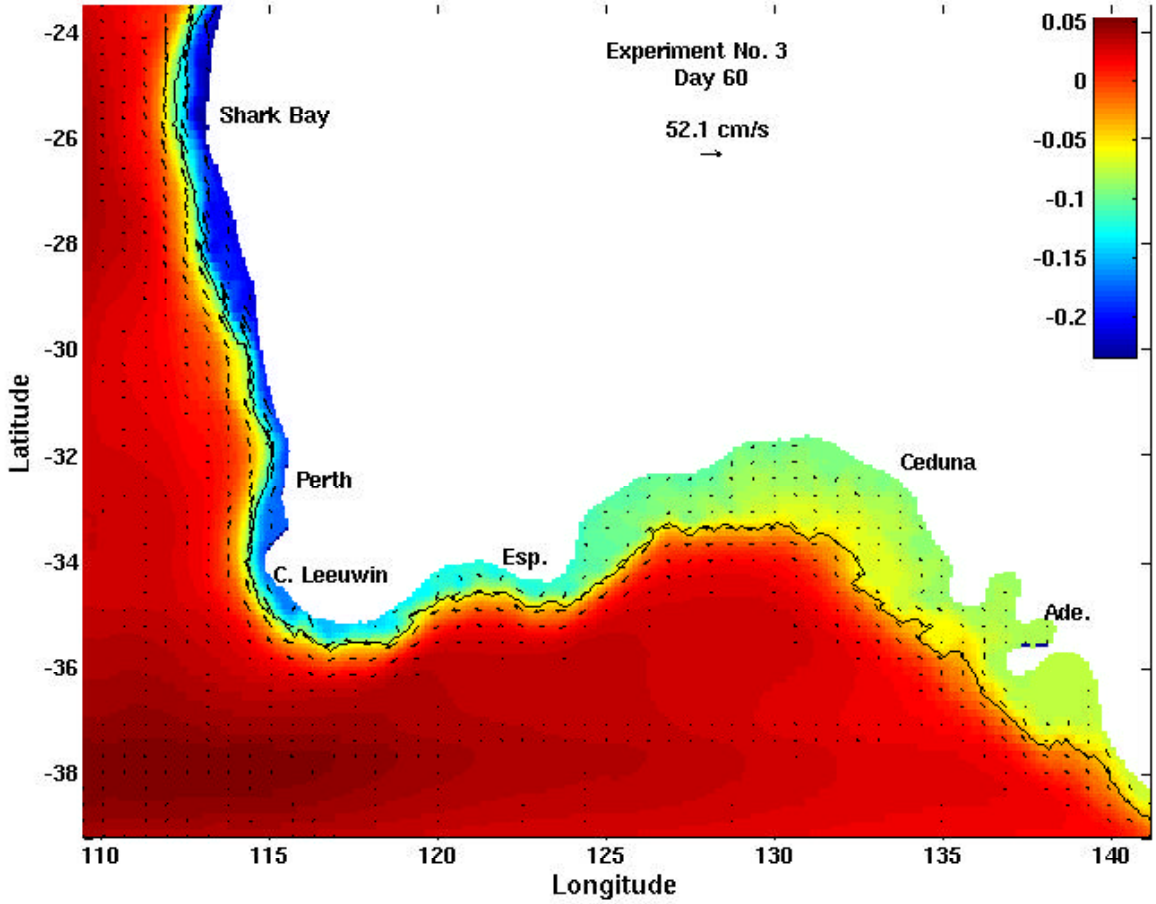

Figure 13c. Surface elevation (m) and velocity vectors for Experiment 3 on day 60. The 200m isobath is shown.

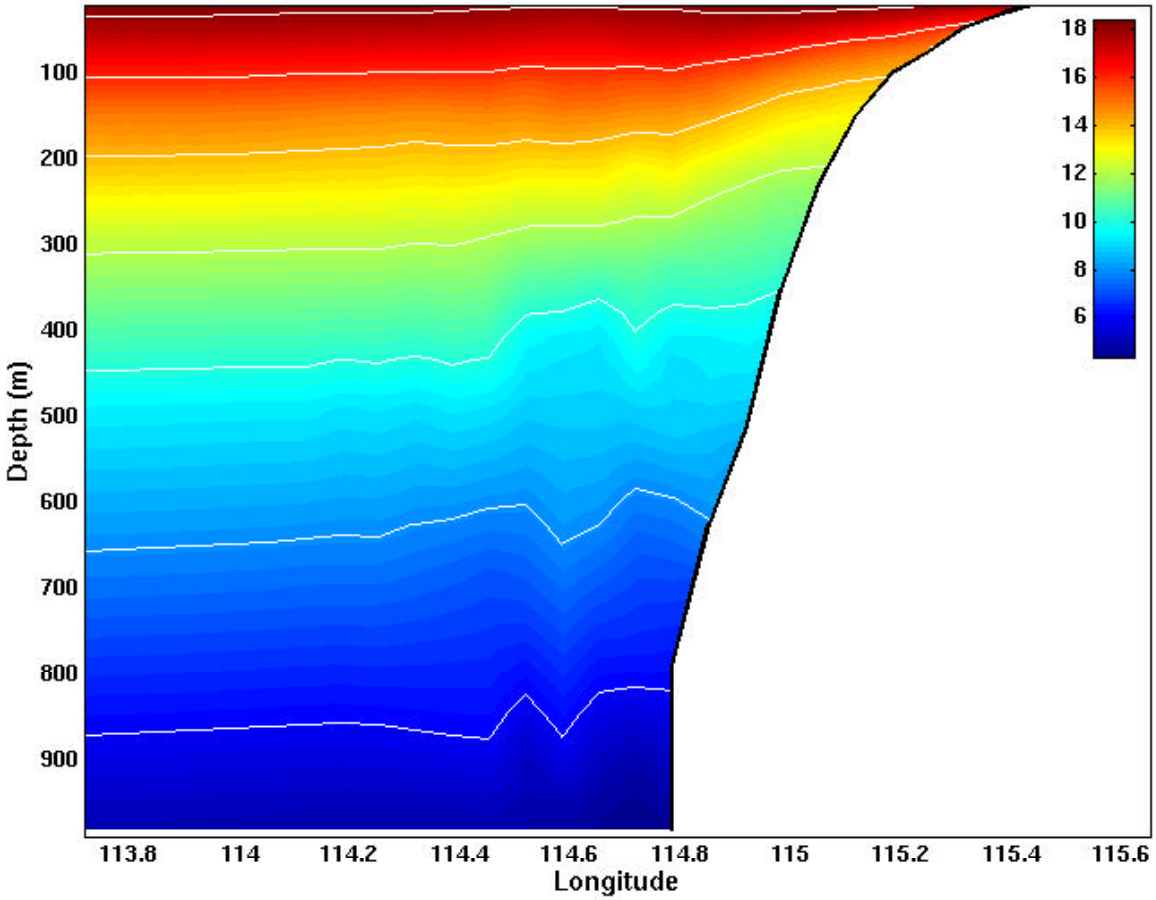

Figure 13d. Cross-section of temperature (°C) at 32°S for Experiment 3 day 60, with a contour interval of two degrees.

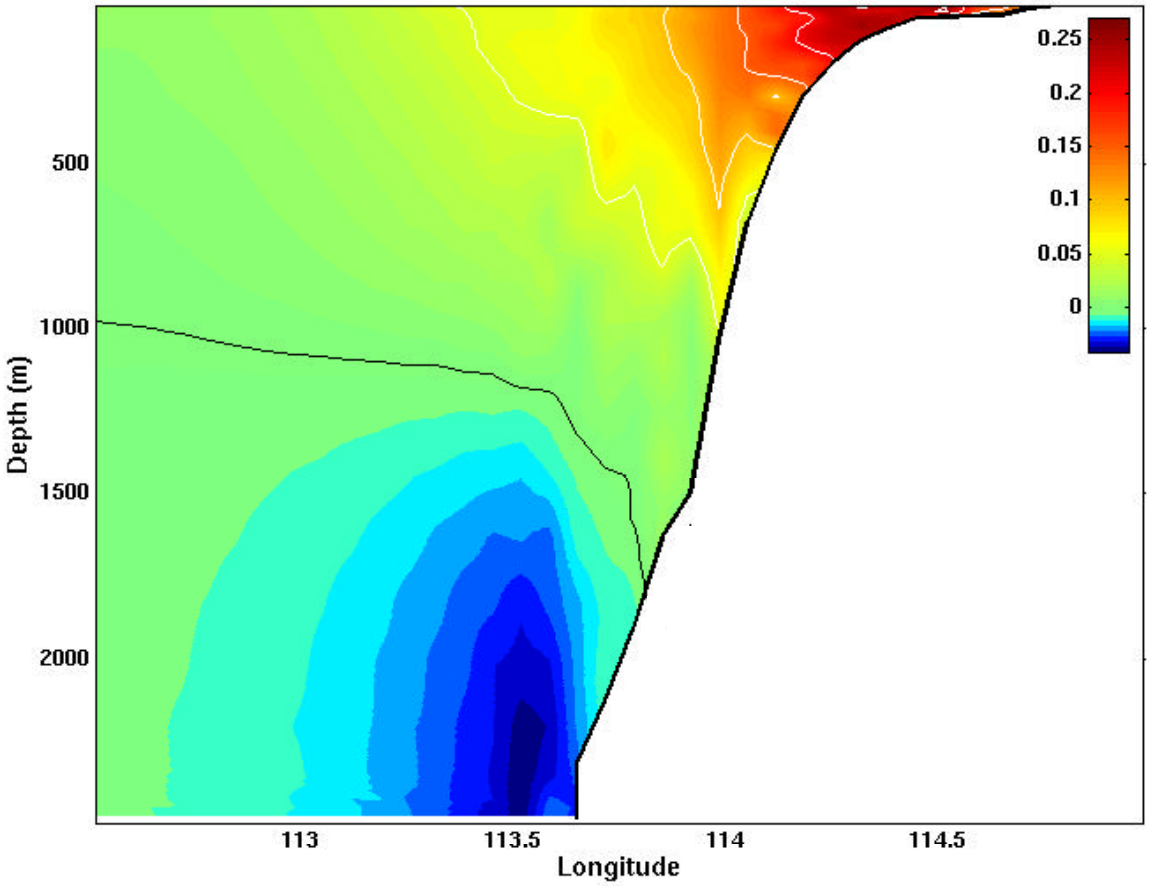

Figure 13e. Cross-section of north-south velocities (m/s) at 34°S for Experiment 3 day 60, with a contour interval of 5 cm/s. Red is equatorward (north).

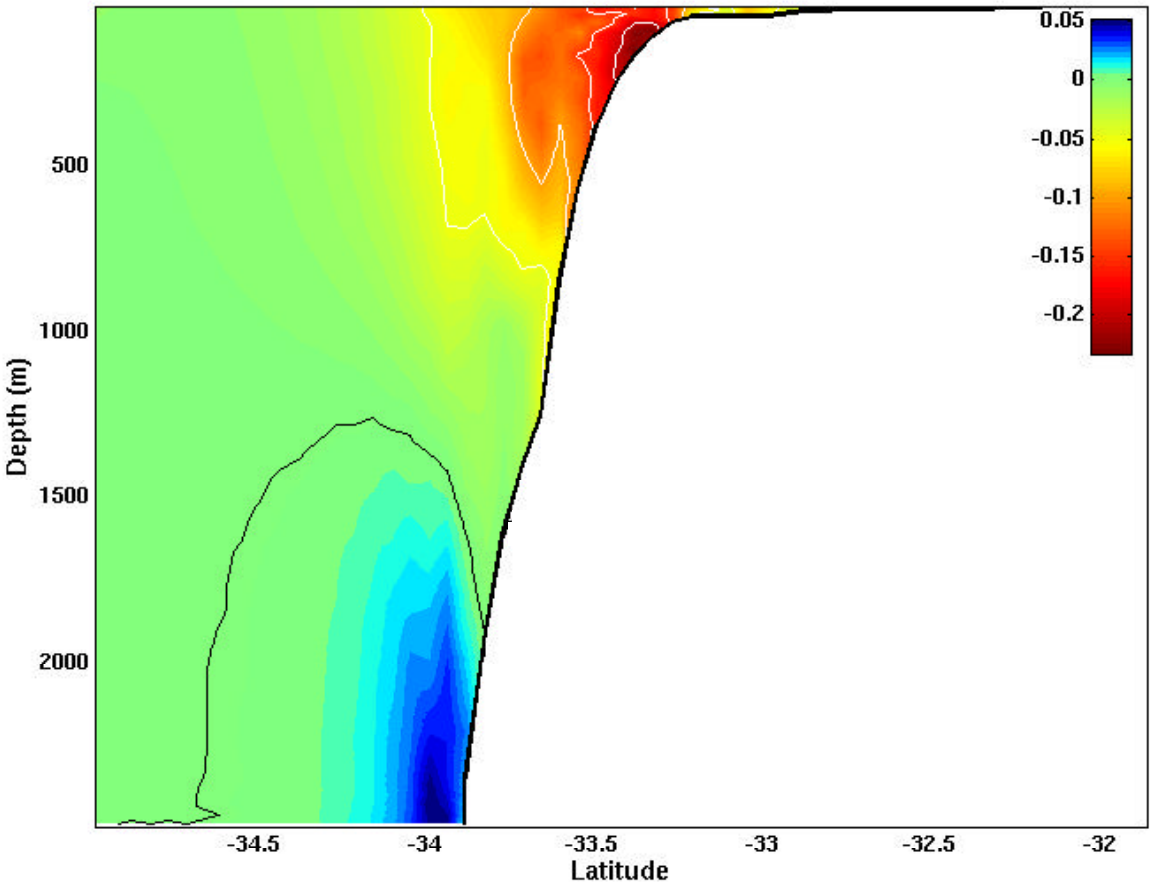

Figure 13f. Cross-section of east-west velocities (m/s) at 128.3°E for Experiment 3 day 60, with a contour interval of 5 cm/s. Red is westward.

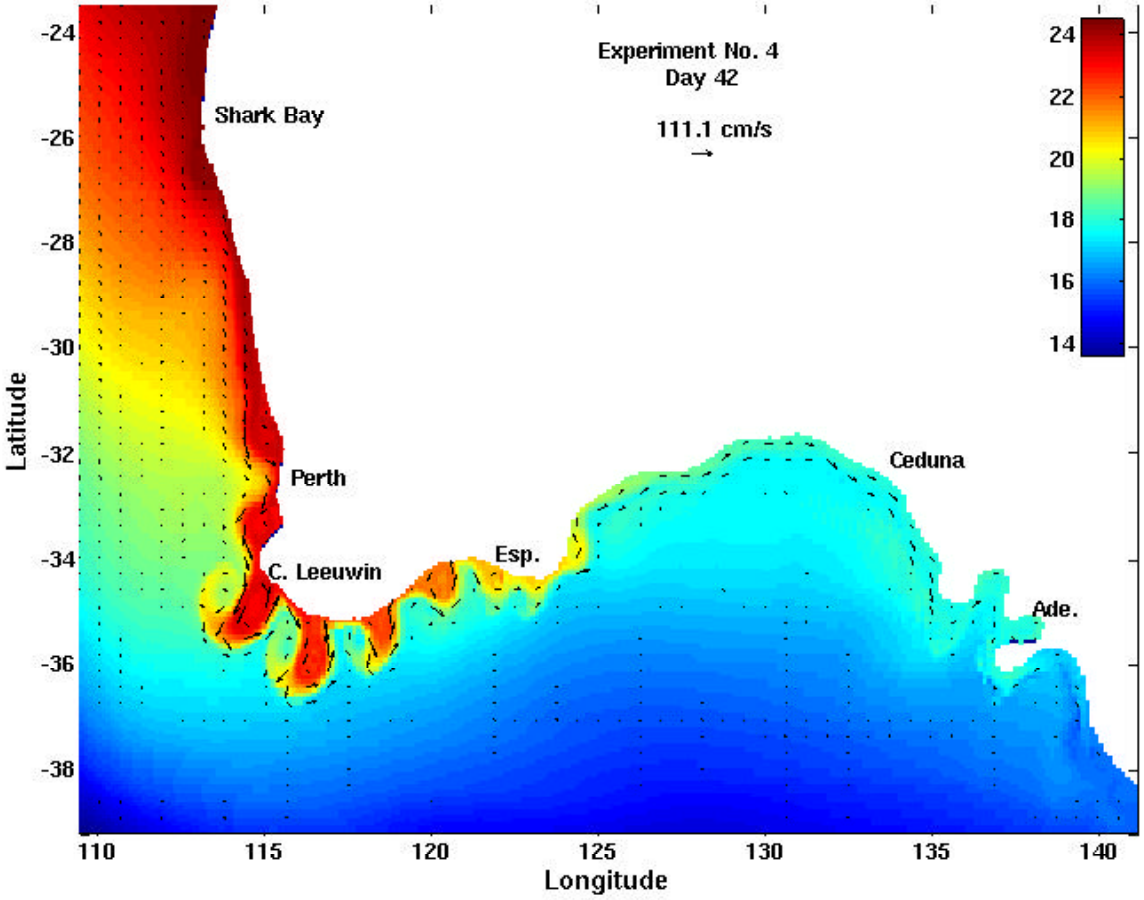

Figure 14a. Surface temperature (°C) and velocity vectors for Experiment 4 on day 42.

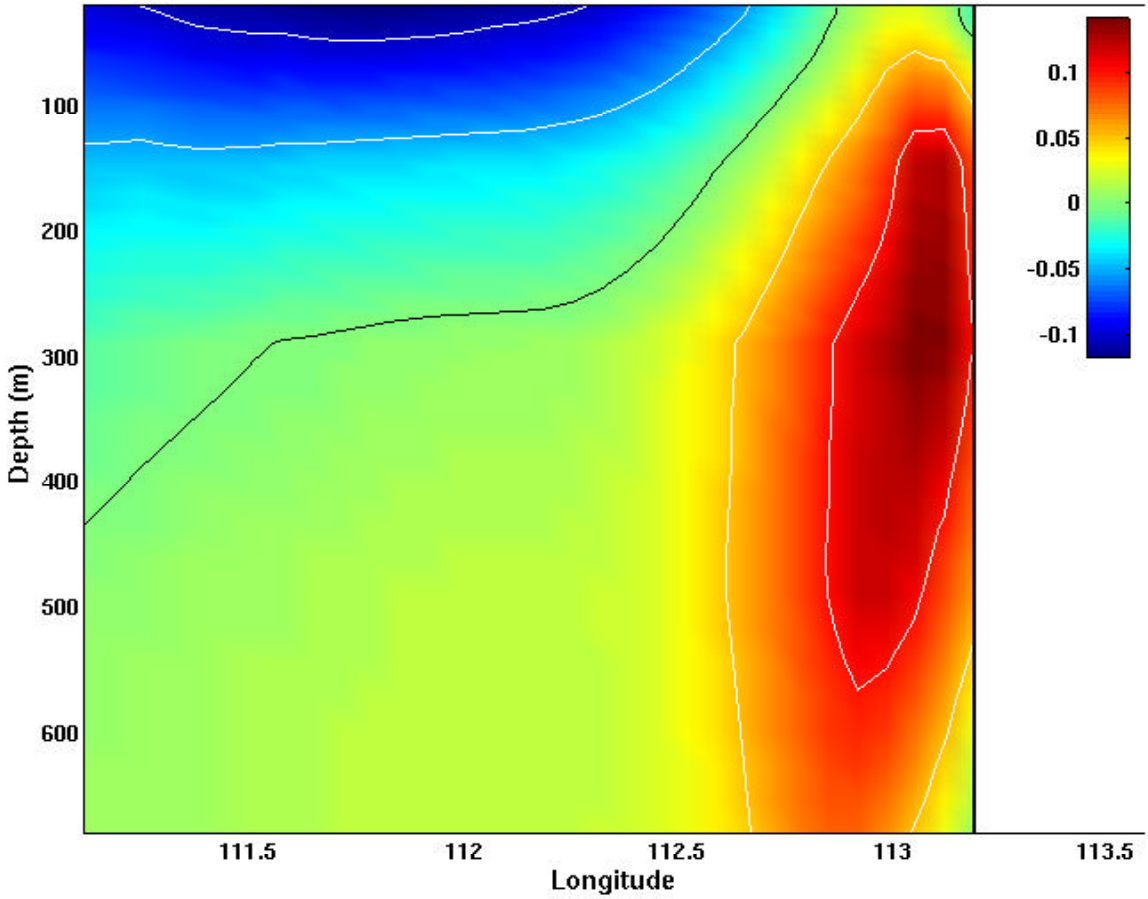

Figure 14b. Cross-section of north-south velocities (m/s) at 25°S for Experiment 4 day 42, with a contour interval of 5 cm/s. Red is equatorward (north).

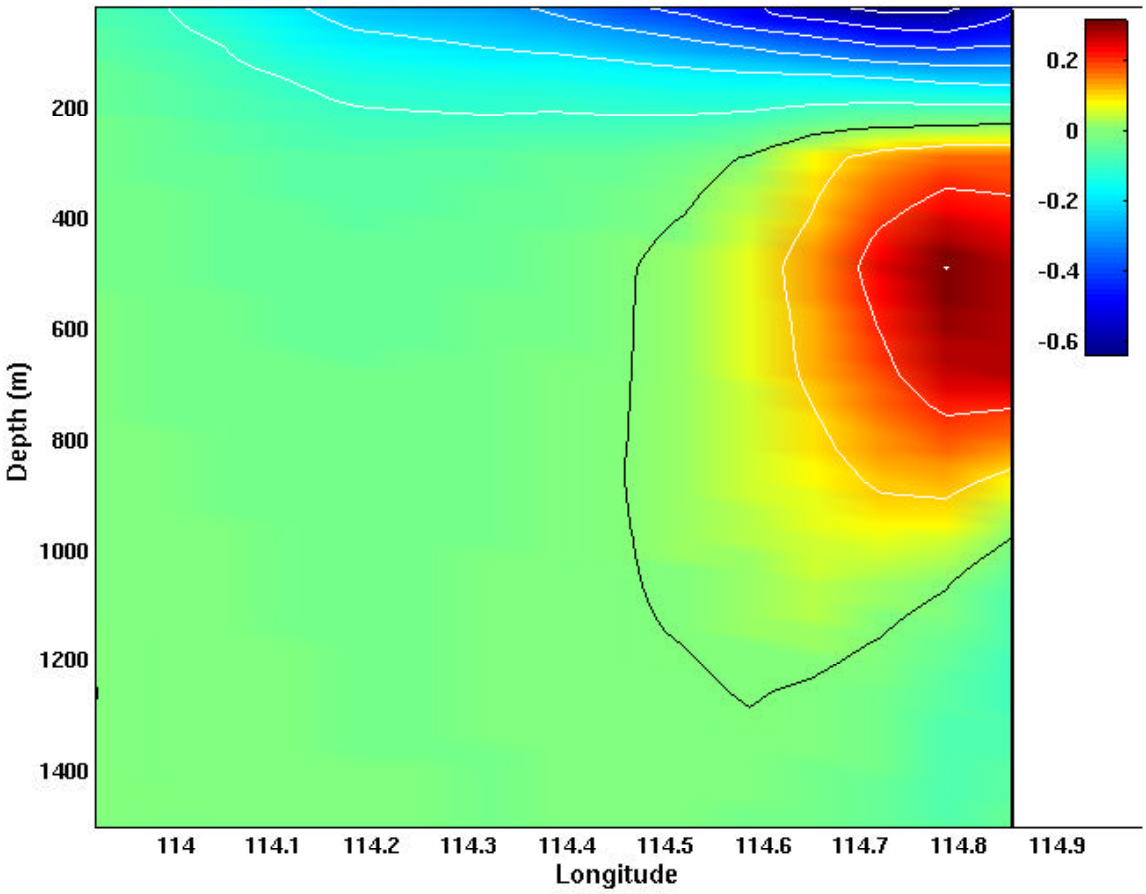

Figure 14c. Cross-section of north-south velocities (m/s) at 34°S for Experiment 4 day 42, with a contour interval of 10 cm/s. Red is equatorward (north).

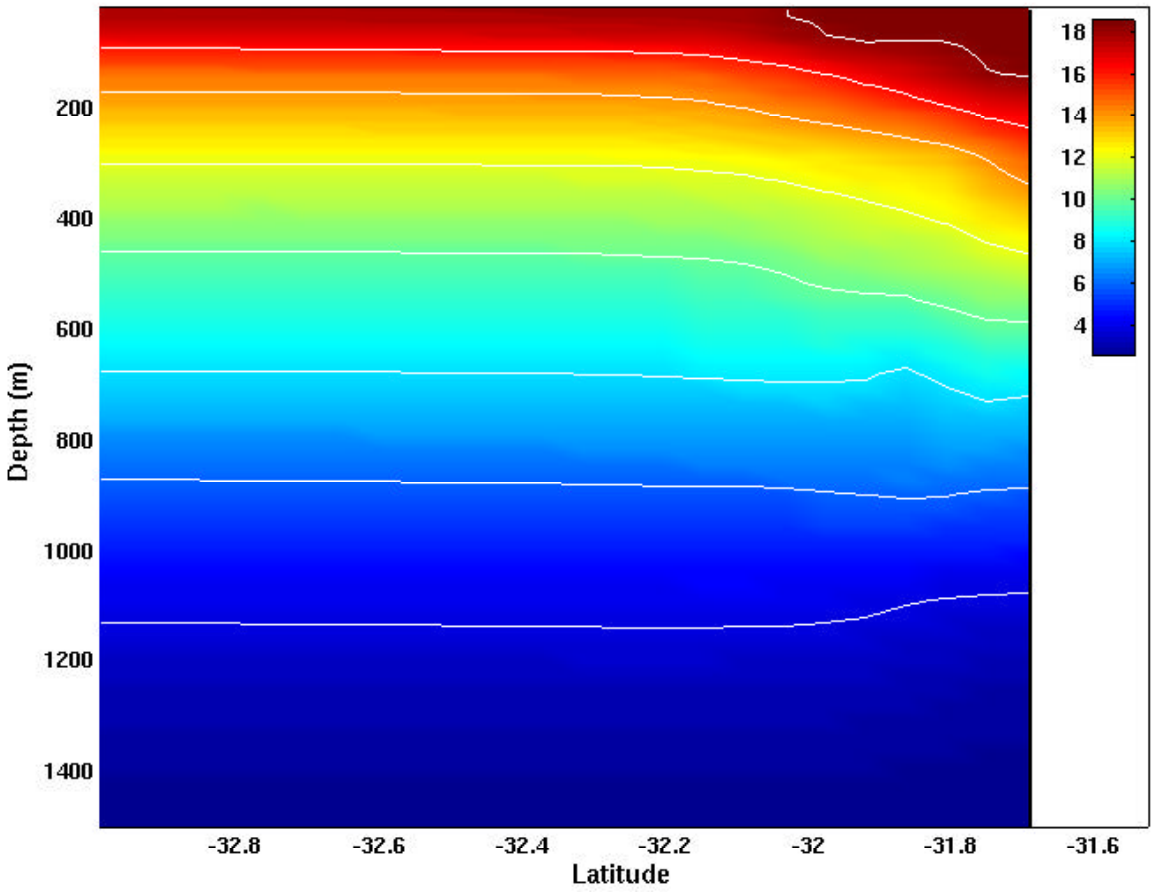

Figure 14d. Cross-section of temperature (°C) at 130.1°E for Experiment 4 day 42, with a contour interval of two degrees.

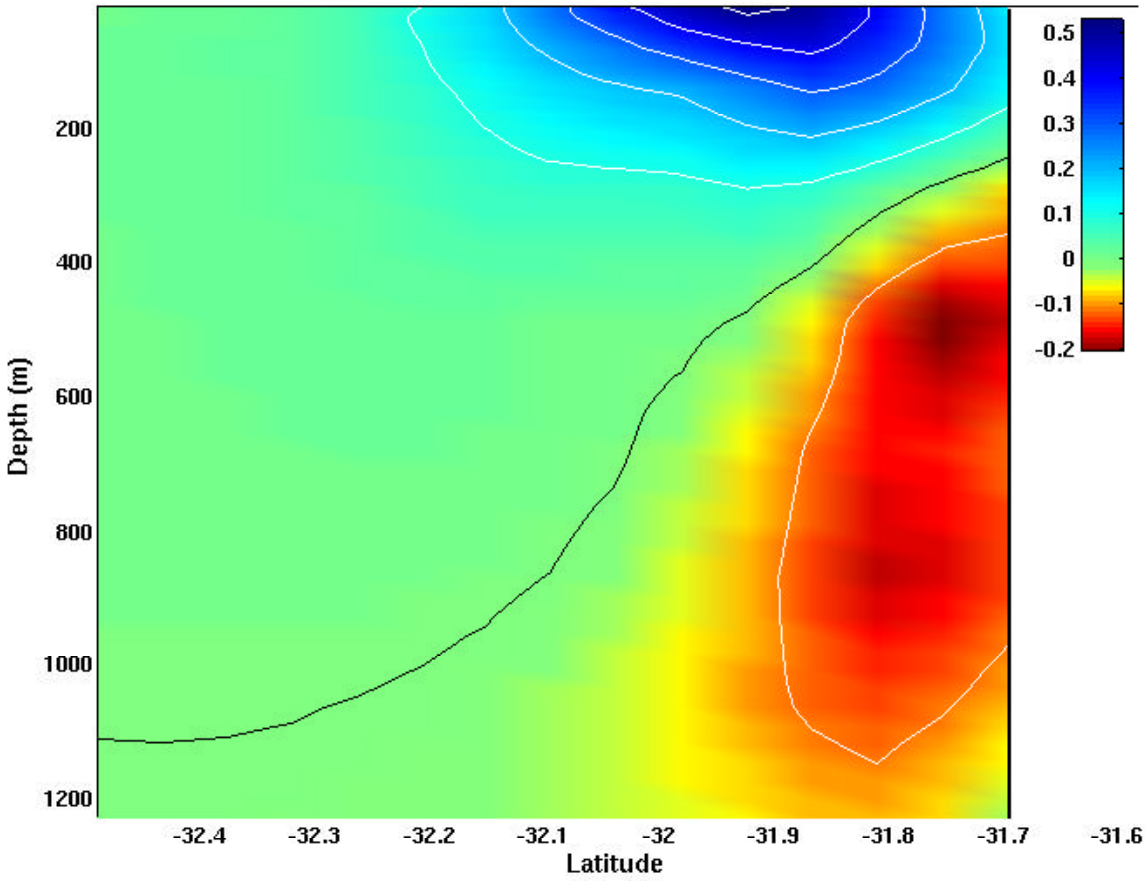

Figure 14e. Cross-section of east-west velocities (m/s) at 131°E for Experiment 4 day 42, with a contour interval of 10 cm/s. Red is westward.

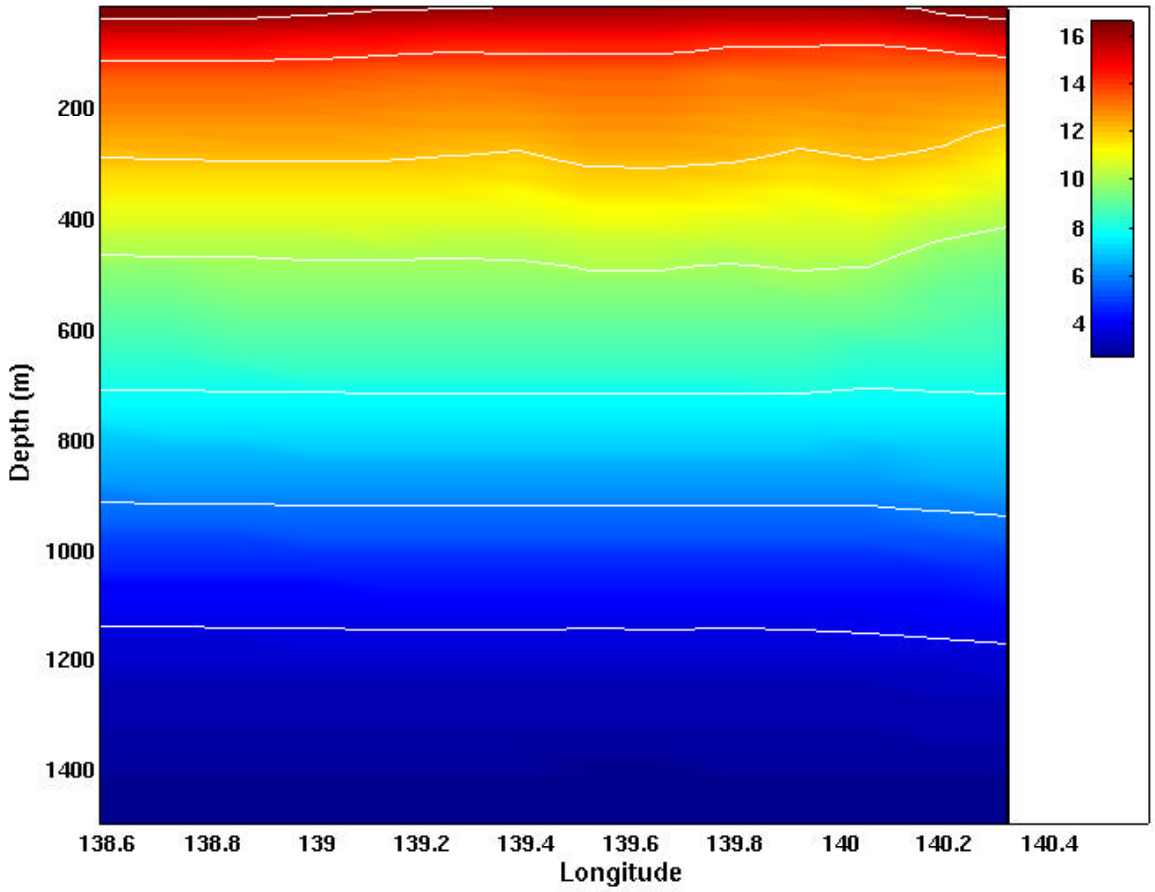

Figure 14f. Cross-section of temperature (°C) at 38°S for Experiment 4 day 42, with a contour interval of two degrees.

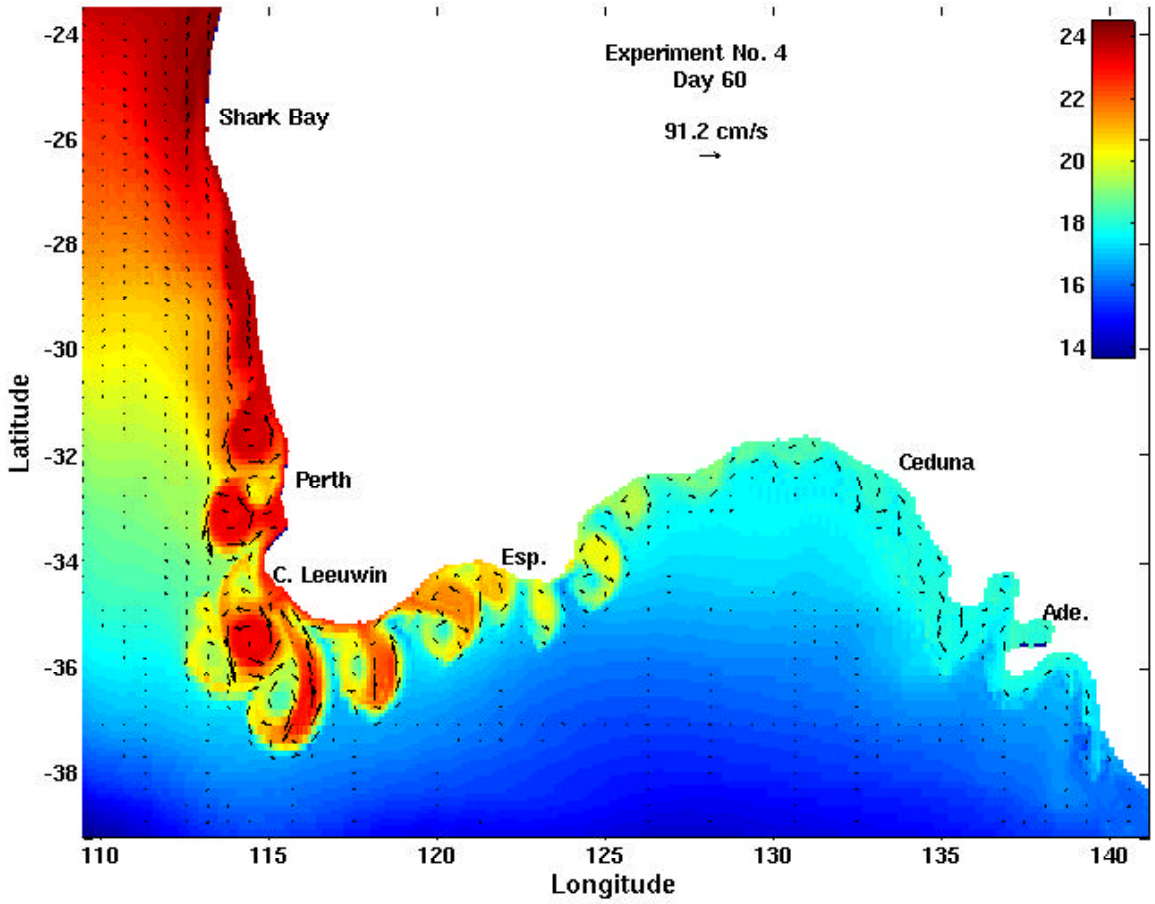

Figure 14g. Surface temperature (°C) and velocity vectors for Experiment 4 on day 60.

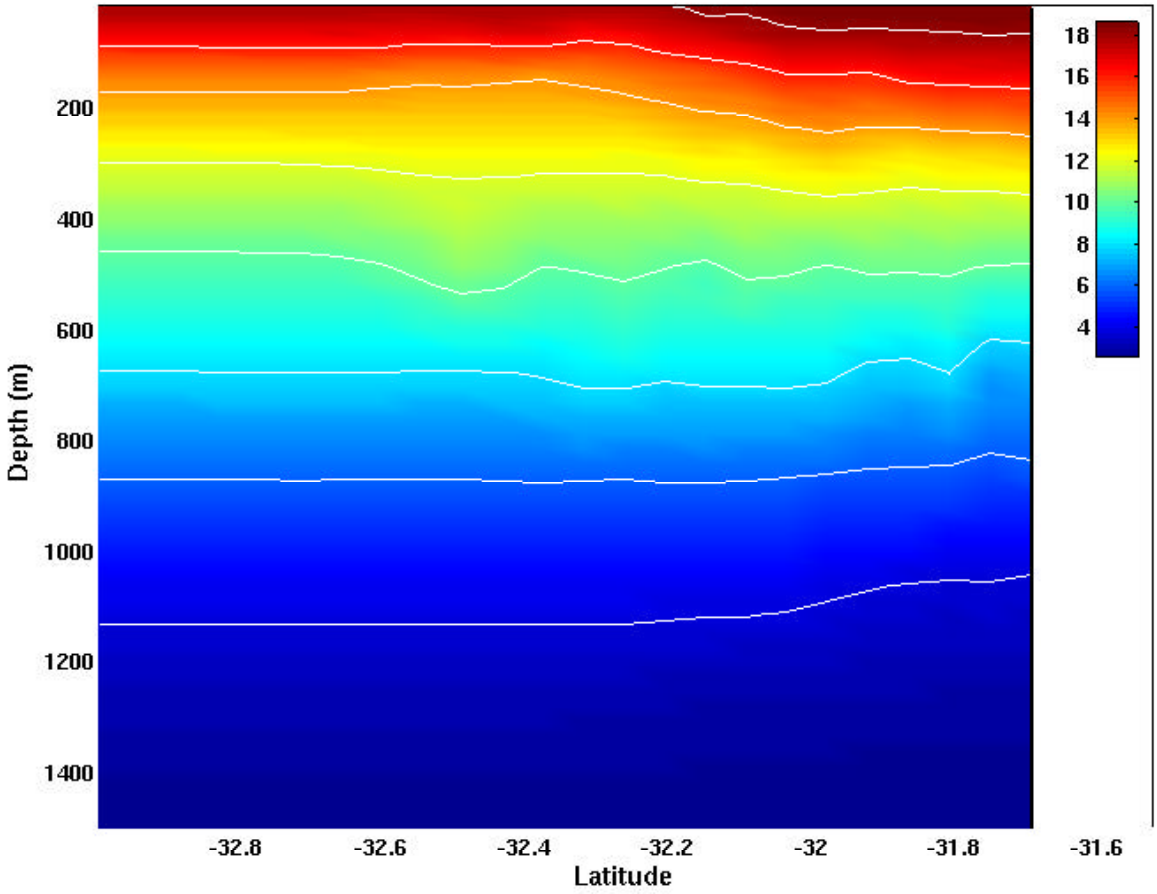

Figure 14h. Cross-section of temperature (°C) at 130.1°E for Experiment 4 day 60, with a contour interval of two degrees.

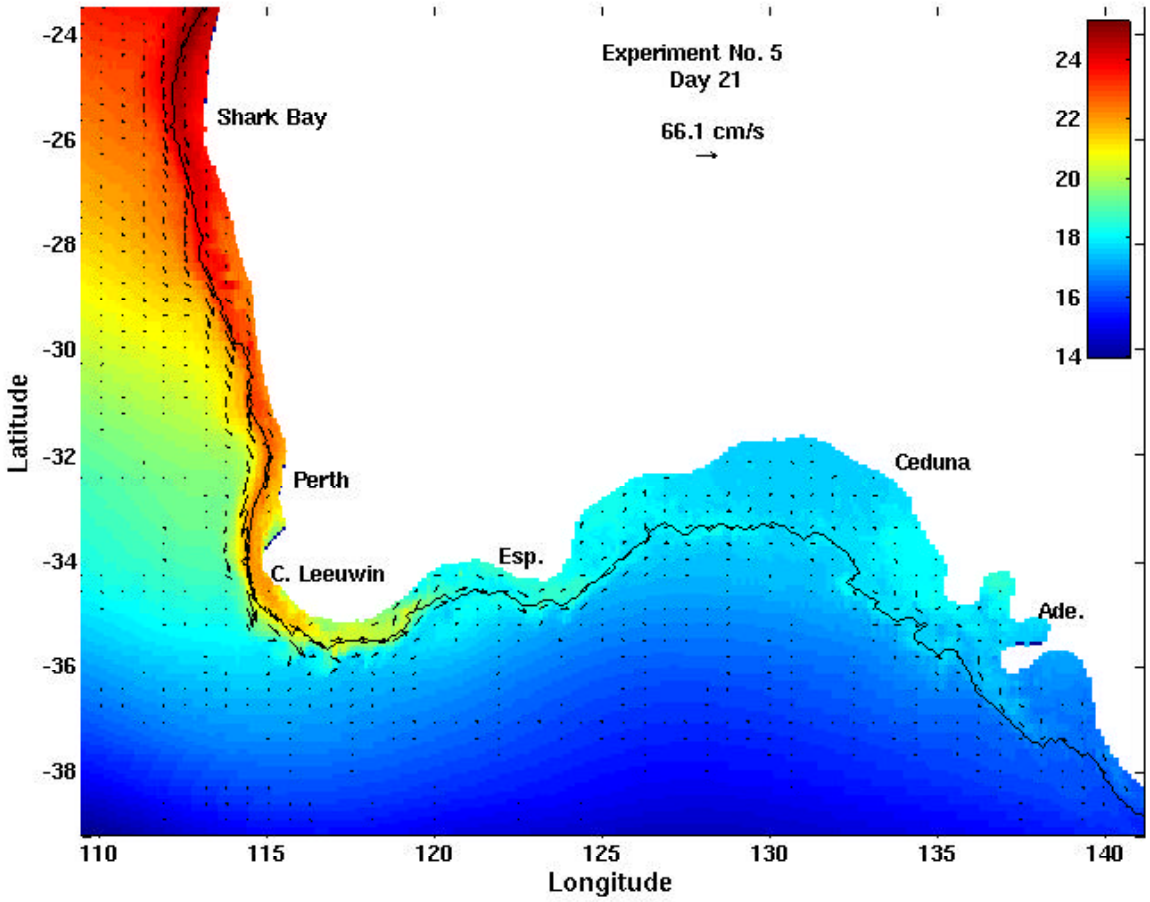

Figure 15a. Surface temperature (°C) and velocity vectors for Experiment 5 on day 21. The 200m isobath is shown.

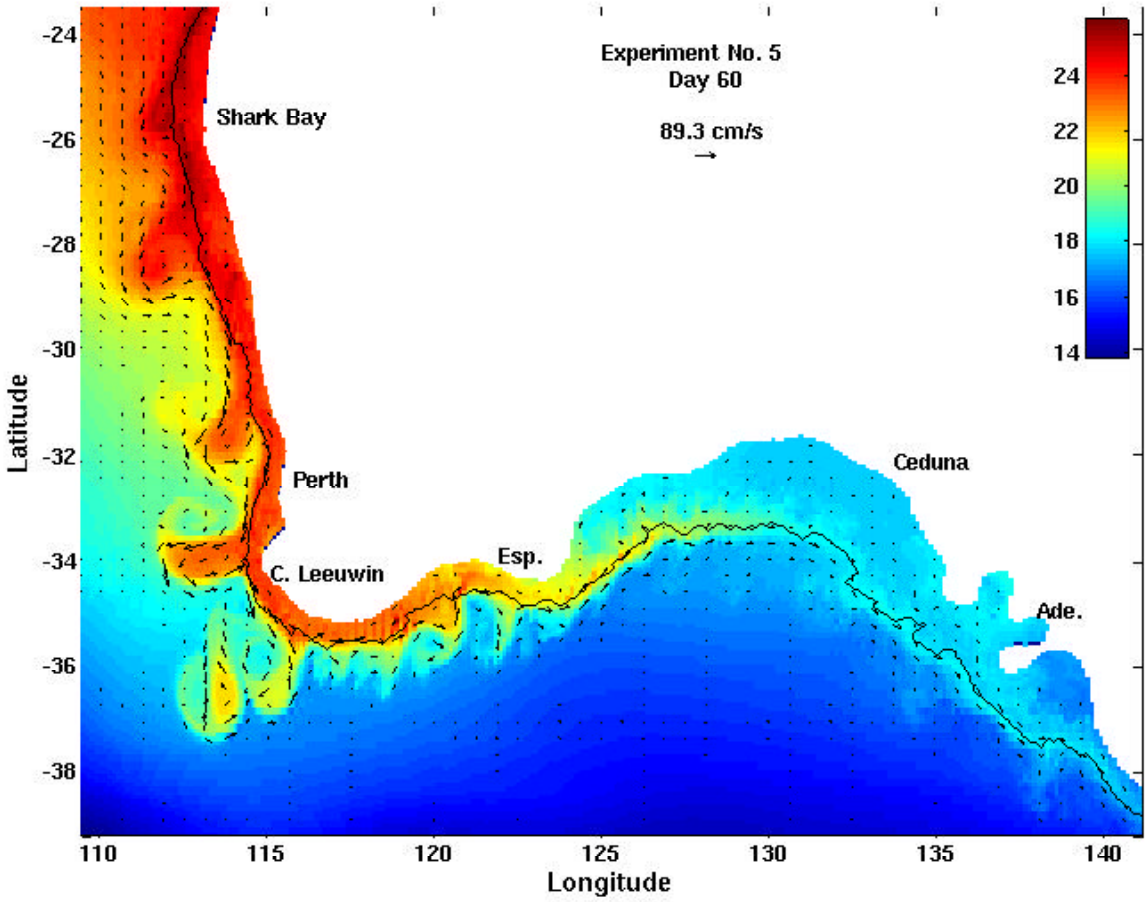

Figure 15b. Surface temperature (°C) and velocity vectors for Experiment 5 on day 60. The 200m isobath is shown.

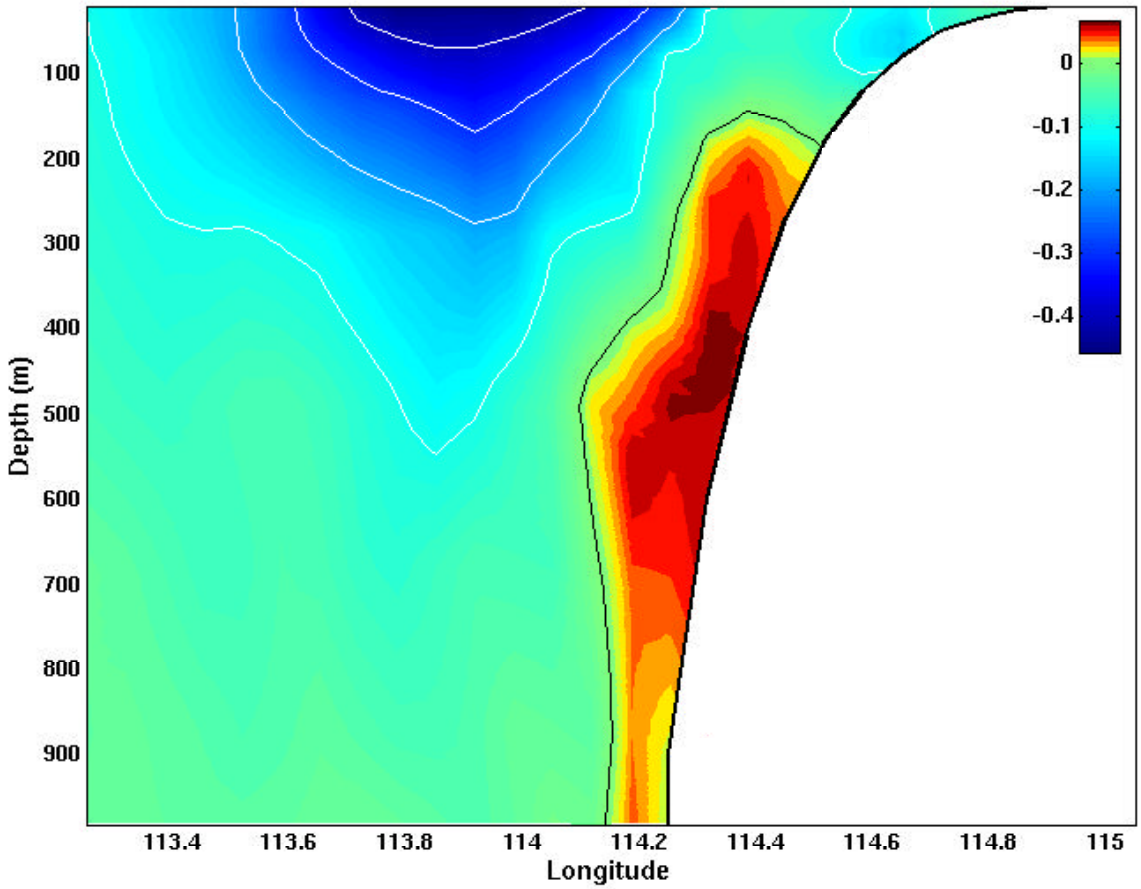

Figure 15c. Cross-section of north-south velocities (m/s) at 30.7°S for Experiment 5 day 60, with a contour interval of 10 cm/s. Red is equatorward (north).

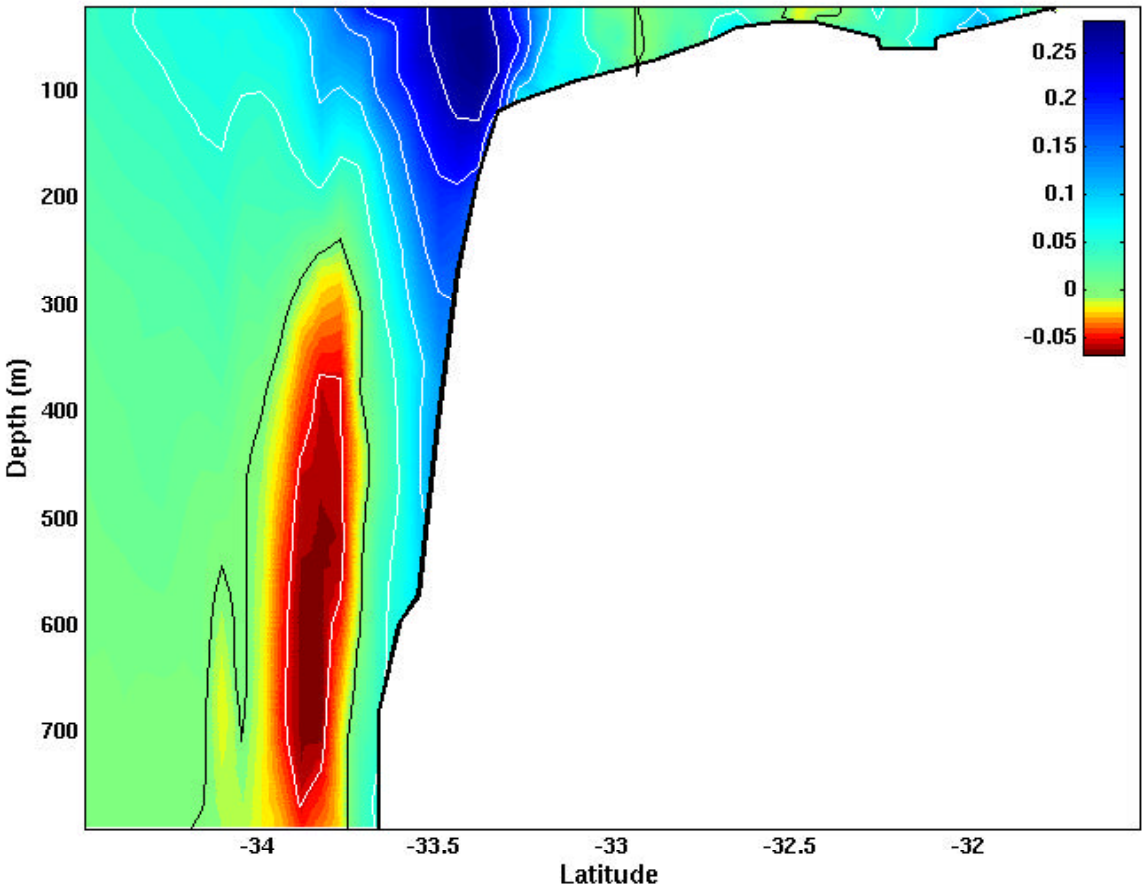

Figure 15d. Cross-section of east-west velocities (m/s) at 129.4°E for Experiment 5 day 60, with a contour interval of 5 cm/s. Red is westward.

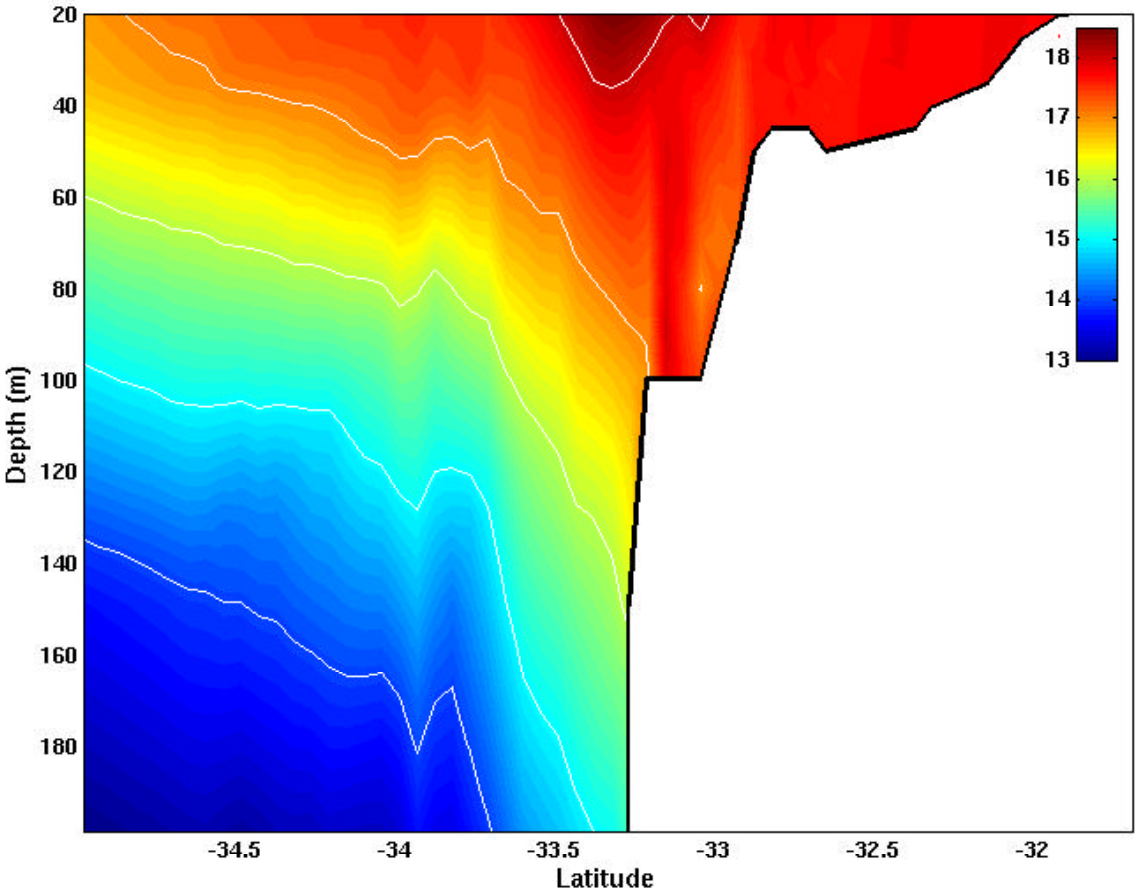

Figure 15e. Cross-section of north-south velocities (m/s) at 30.7°S for Experiment 5 day 60, with a contour interval of 10 cm/s. Red is equatorward (north).

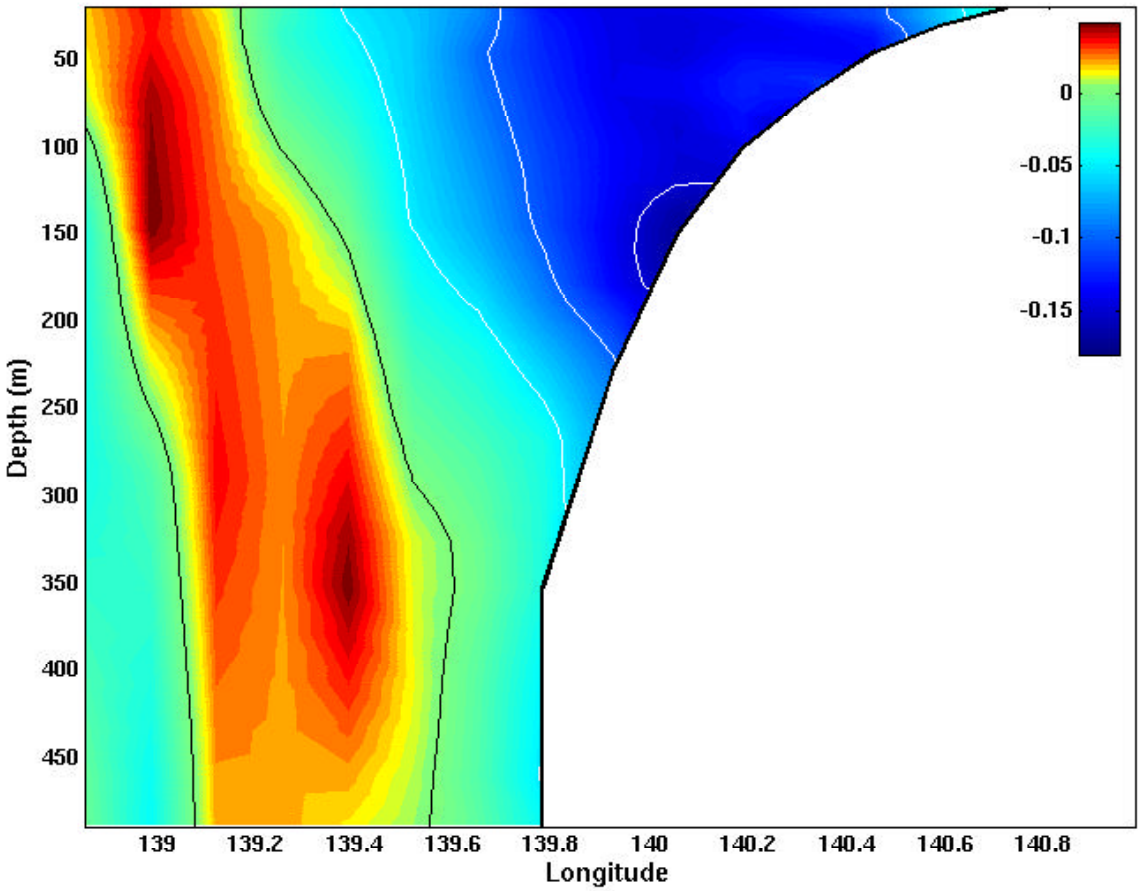

Figure 15f. Cross-section of north-south velocities (m/s) at 38.3°S for Experiment 5 day 60, with a contour interval of 5 cm/s. Red is equatorward (north).

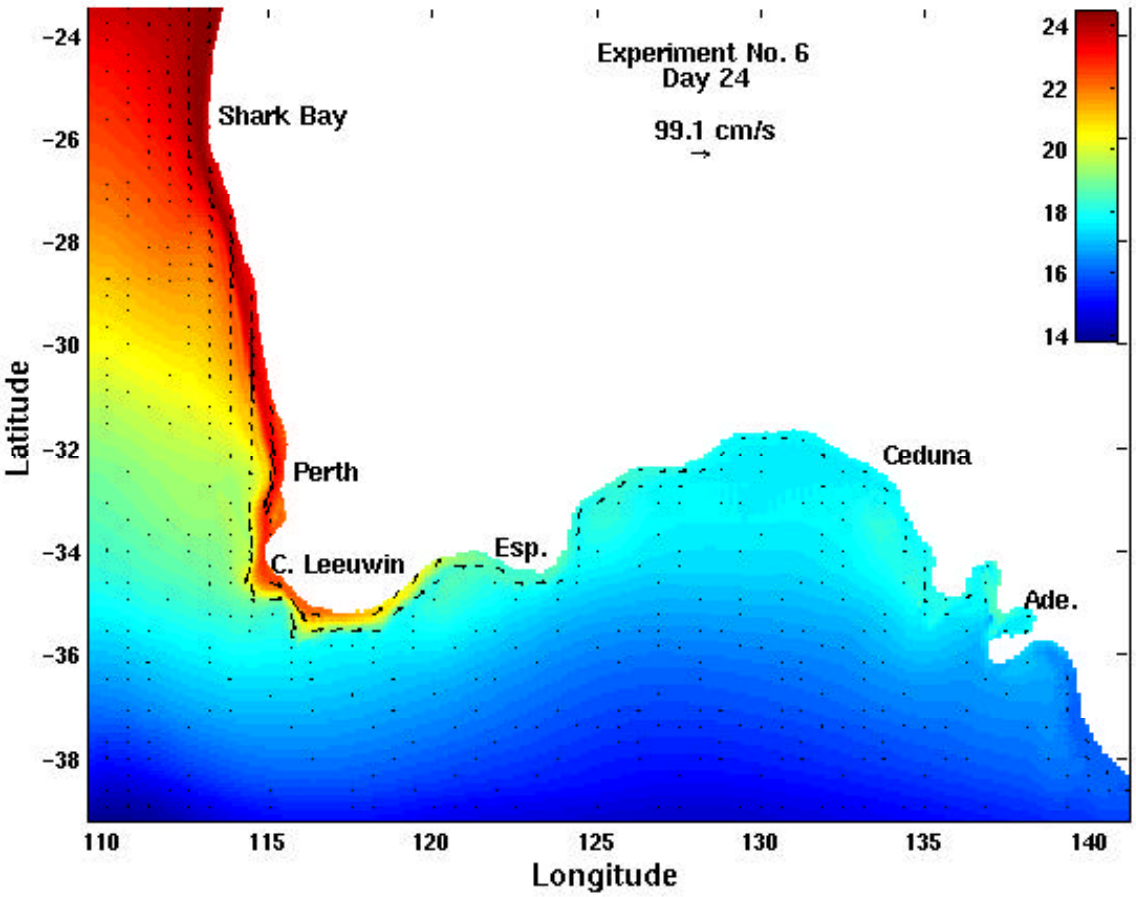

Figure 16a. Surface temperature (°C) and velocity vectors for Experiment 6 on day 24.

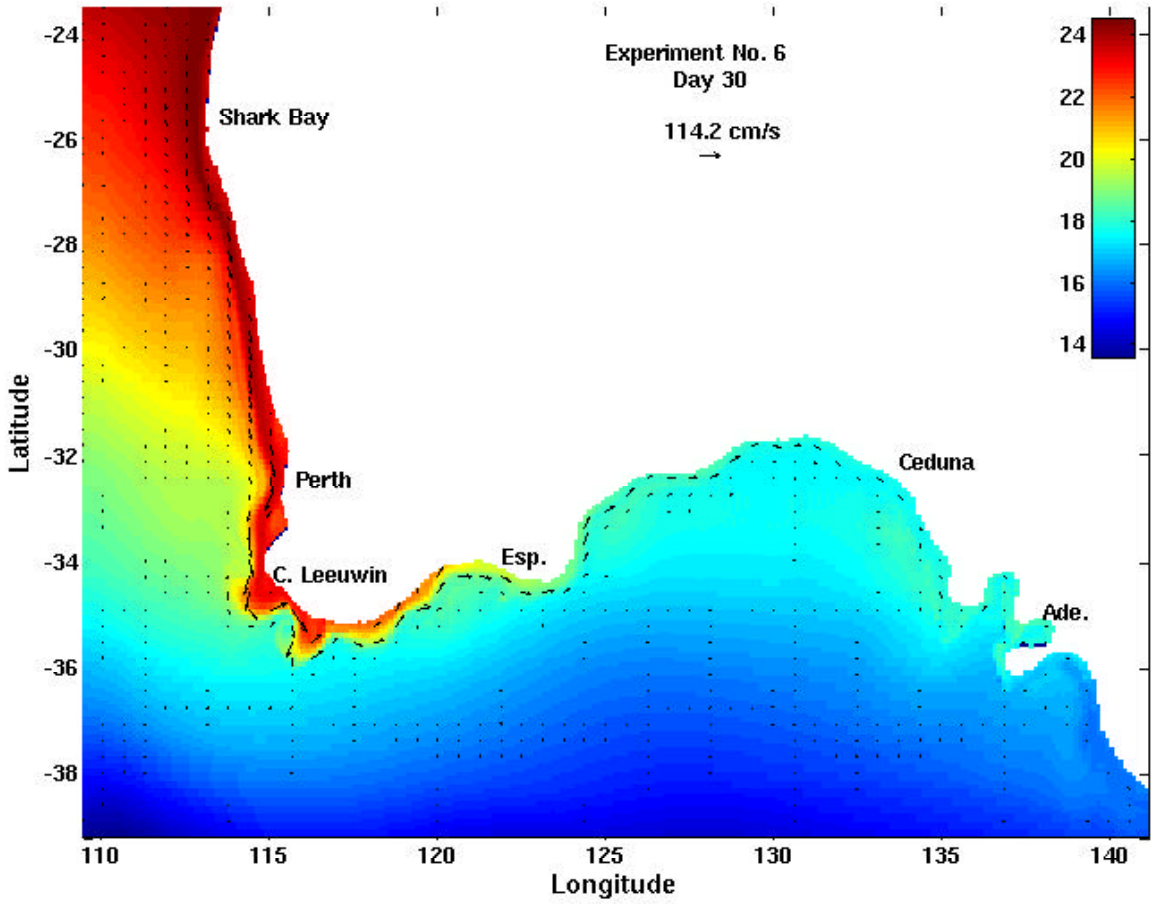

Figure 16b. Surface temperature (°C) and velocity vectors for Experiment 6 on day 30.

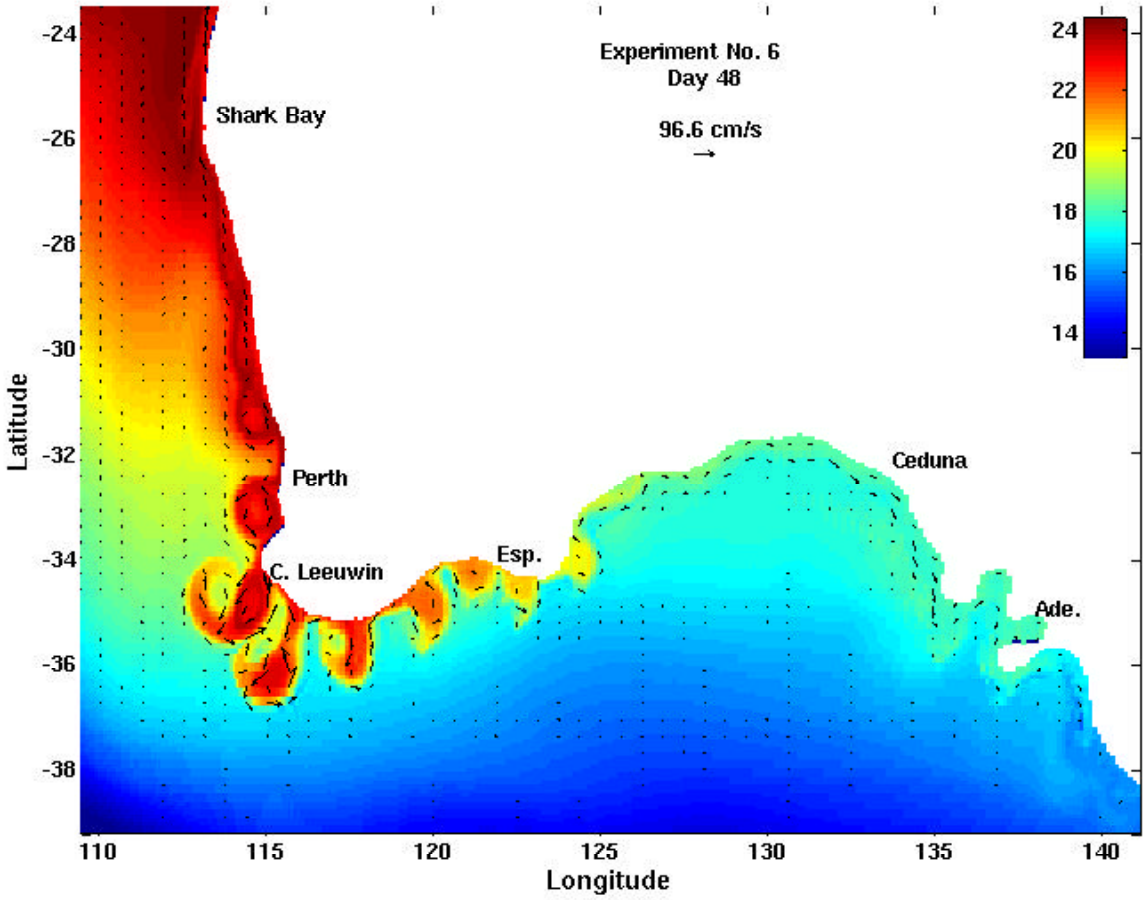

Figure 16c. Surface temperature (°C) and velocity vectors for Experiment 6 on day 48.

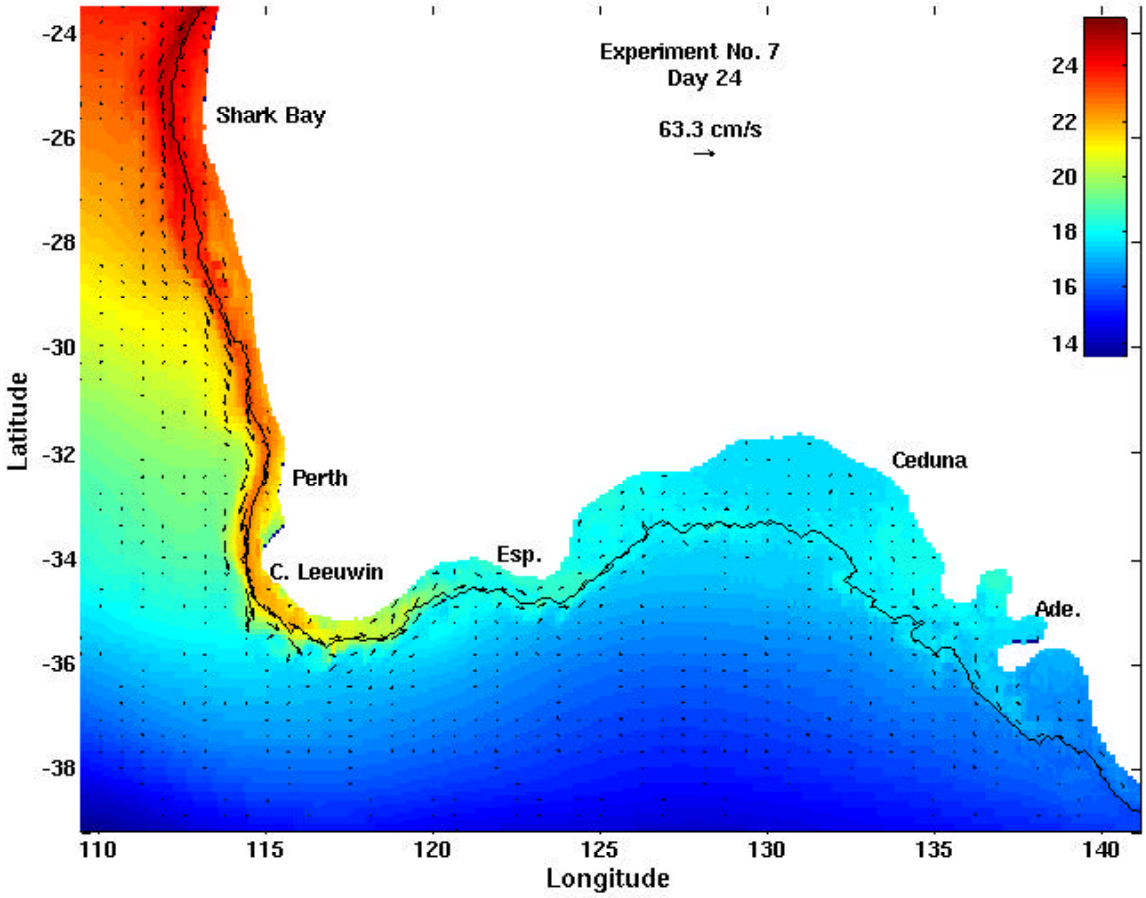

Figure 17a. Surface temperature (°C) and velocity vectors for Experiment 7 on day 24. The 200m isobath is shown.

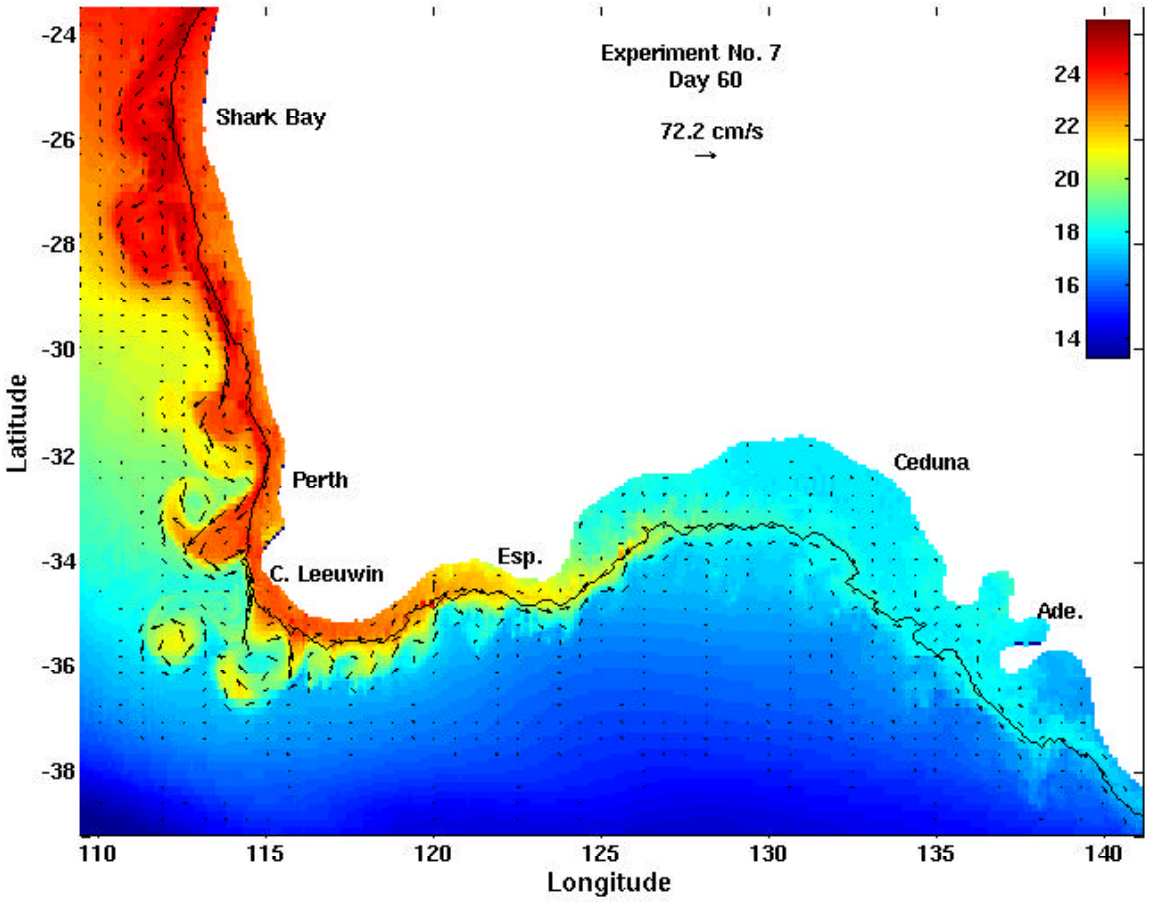

Figure 17b. Surface temperature (°C) and velocity vectors for Experiment 7 on day 60. The 200m isobath is shown.

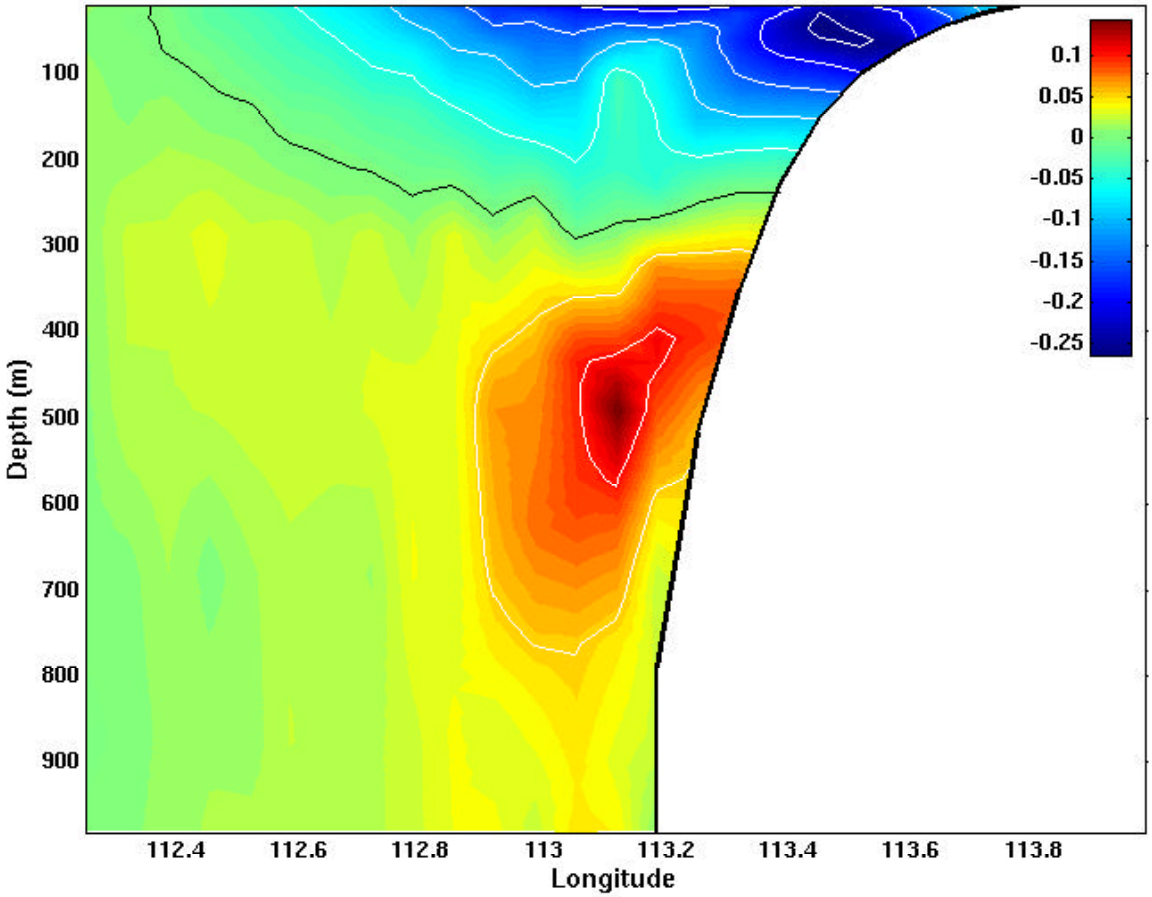

Figure 17c. Cross-section of north-south velocities (m/s) at 28.9°S for Experiment 7 day 60, with a contour interval of 5 cm/s. Red is equatorward (north).

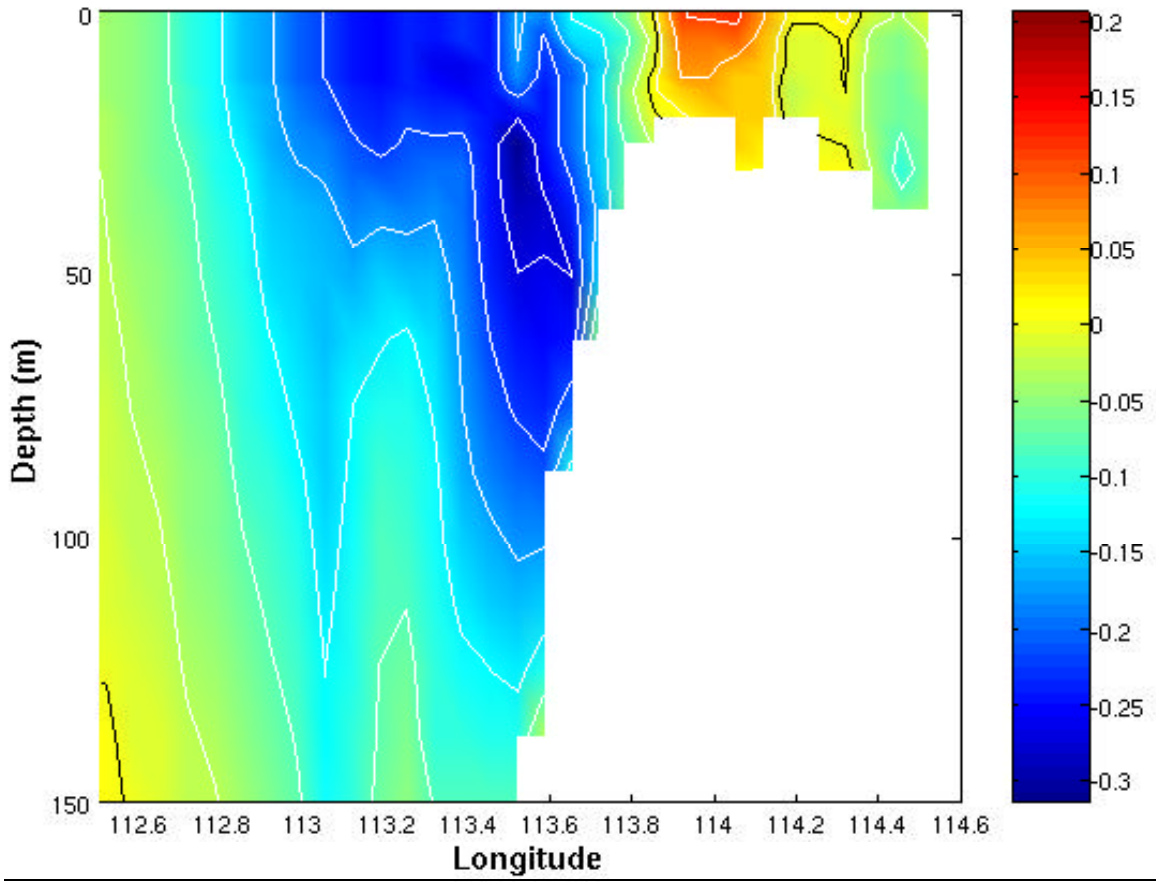

Figure 17d. Cross-section of north-south velocities (m/s) at 28.9°S for Experiment 7 day 60, with a contour interval of 5 cm/s. Red is equatorward (north).

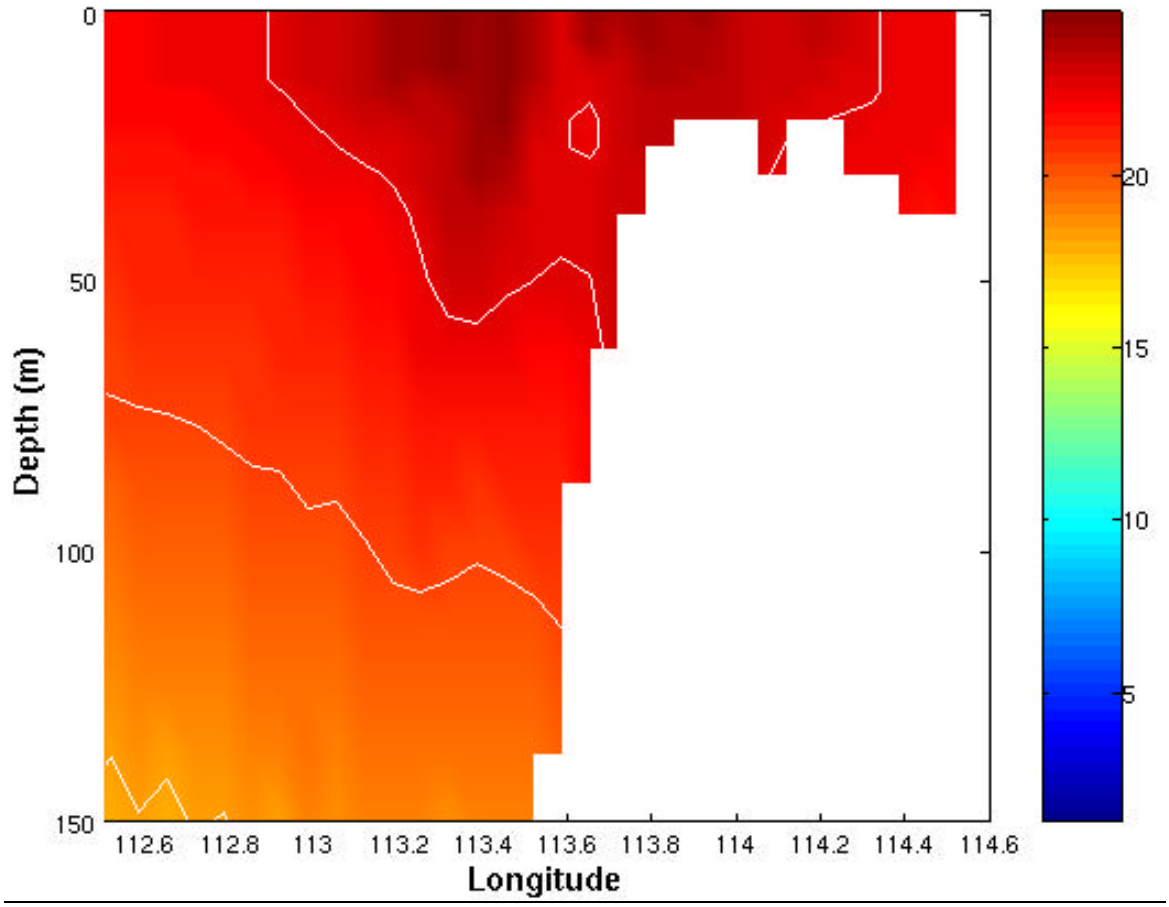

Figure 17e. Cross-section of temperature (°C) at 28.9°S for Experiment 7 day 60, with a contour interval of 2.5 degrees.

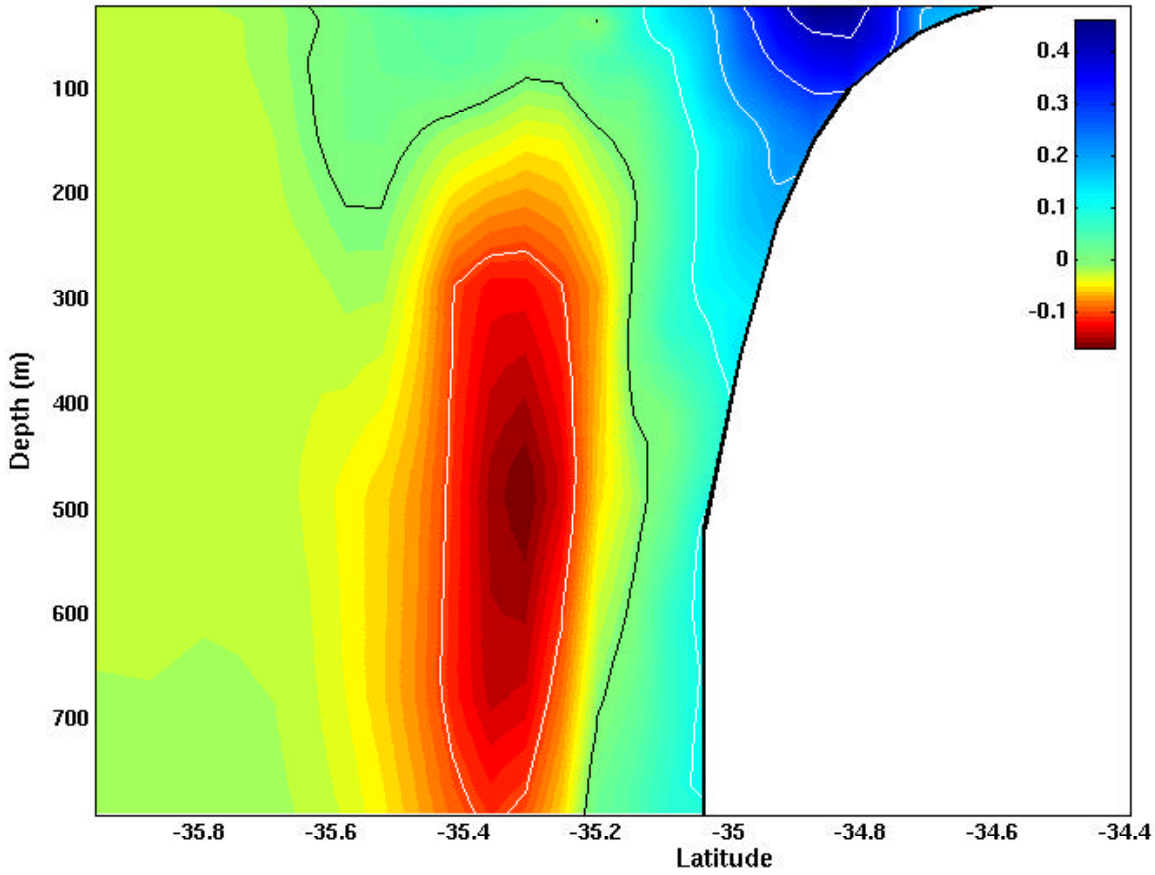

Figure 17f. Cross-section of east-west velocities (m/s) at 123°E for Experiment 7 day 60, with a contour interval of 10 cm/s. Red is westward.

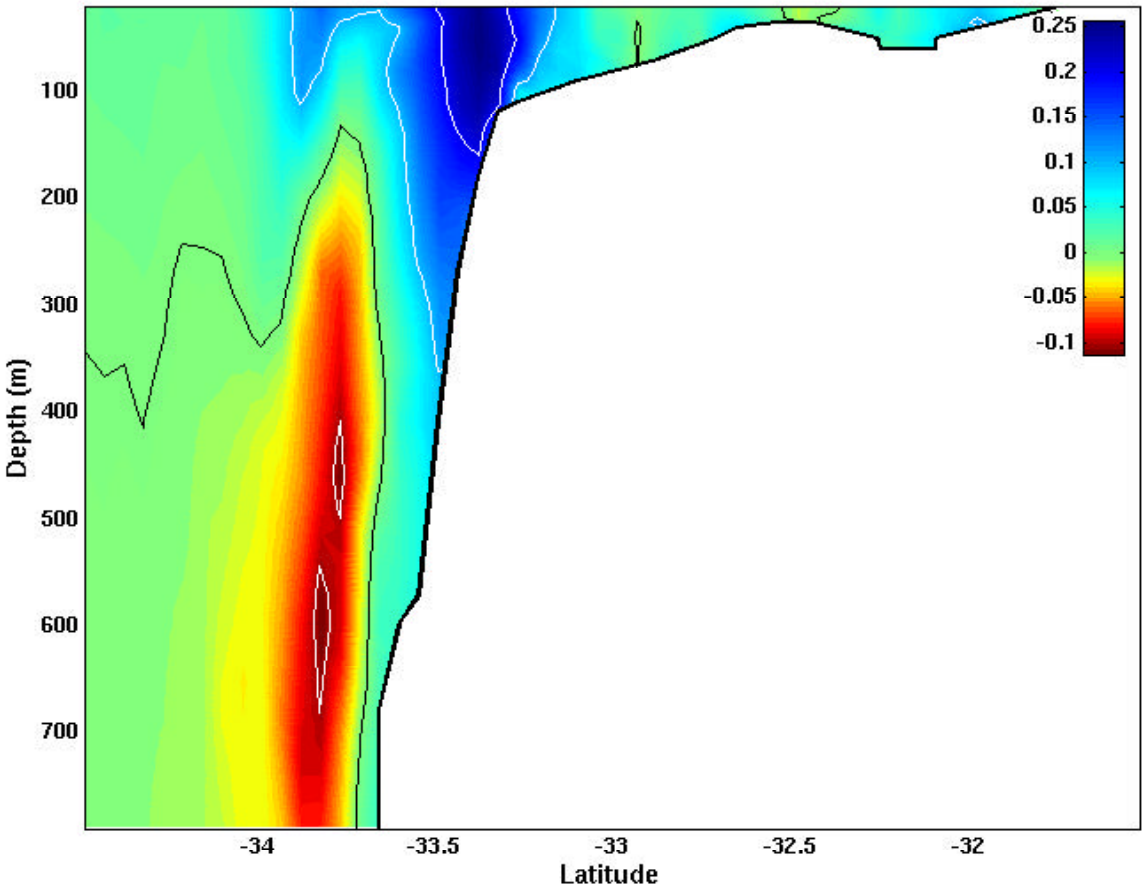

Figure 17g. Cross-section of east-west velocities (m/s) at 129.4°E for Experiment 7 day 60, with a contour interval of 10 cm/s. Red is westward.

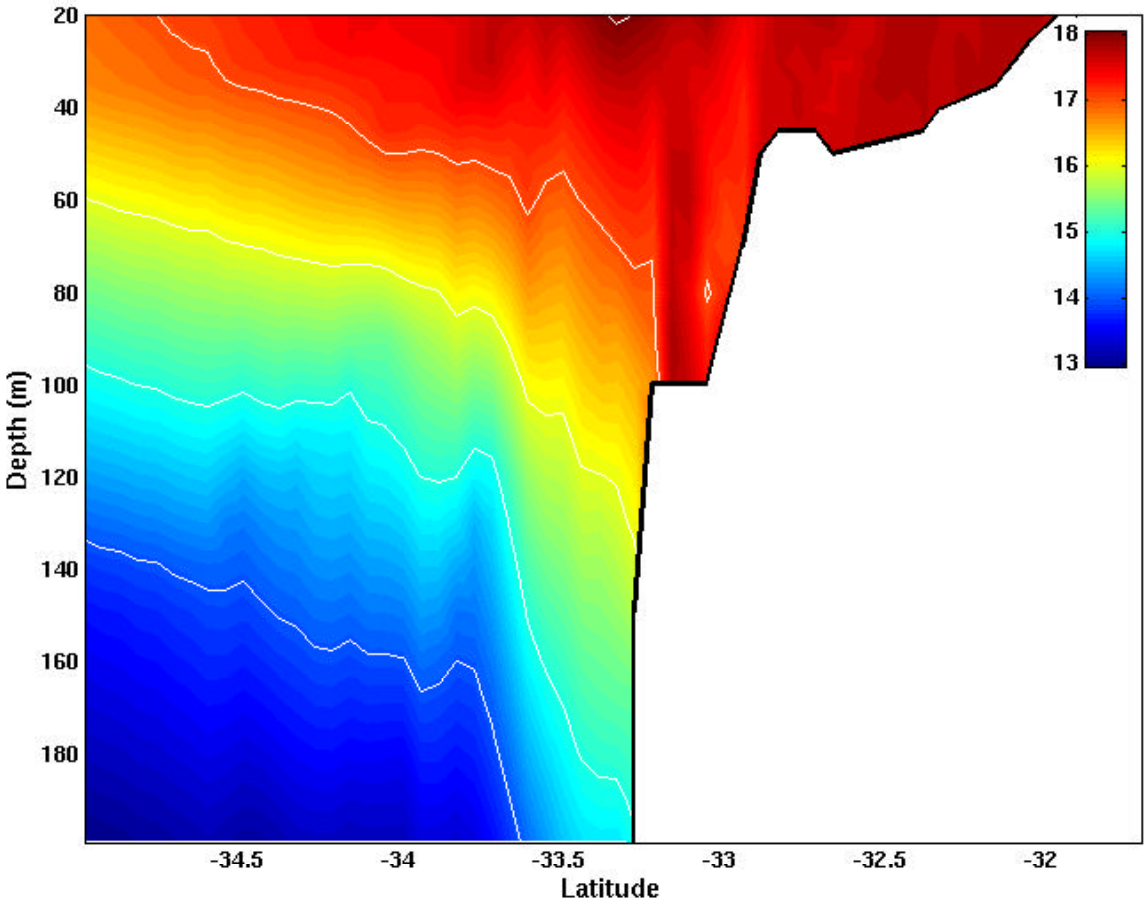

Figure 17h. Cross-section of temperature (°C) at 130.1°E for Experiment 7 day 60, with a contour interval of one degree.

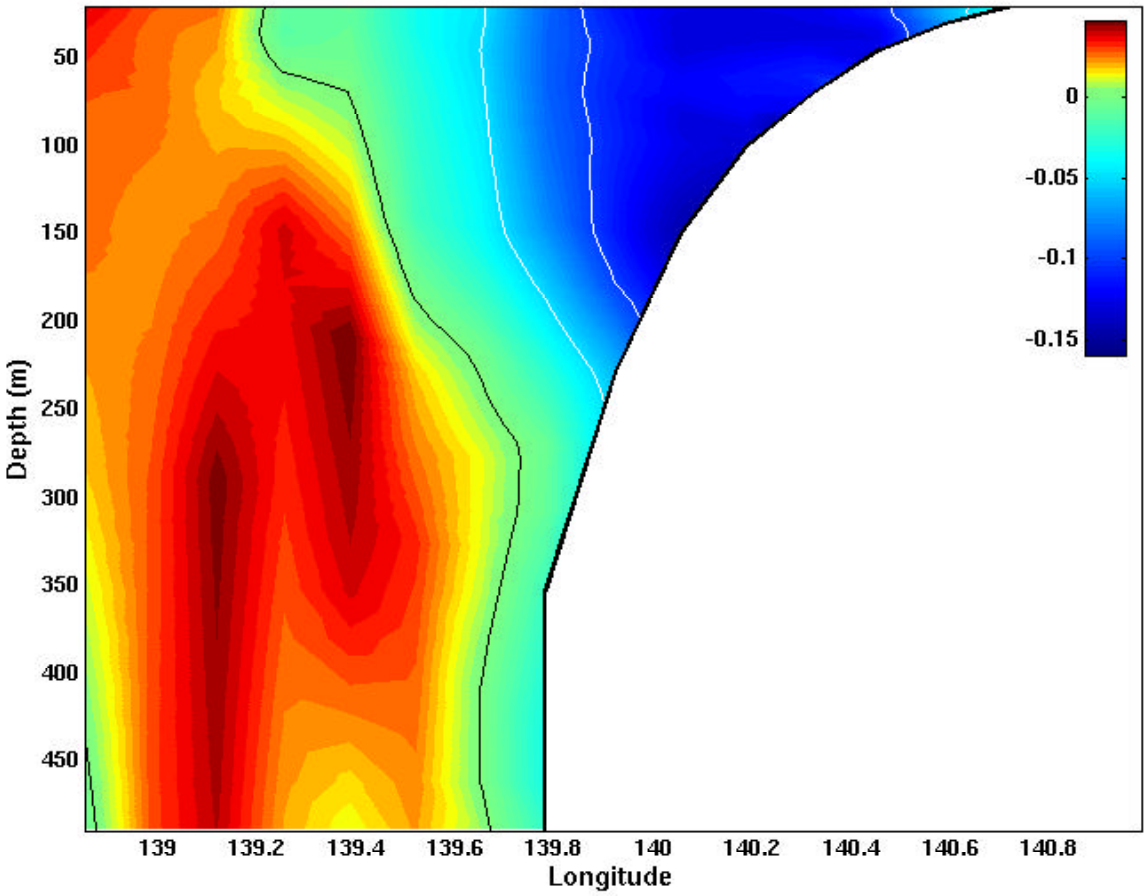

Figure 17i. Cross-section of north-south velocities (m/s) at 38.3°C for Experiment 7 day 60, with a contour interval of 5 cm/s. Red is equatorward (north).

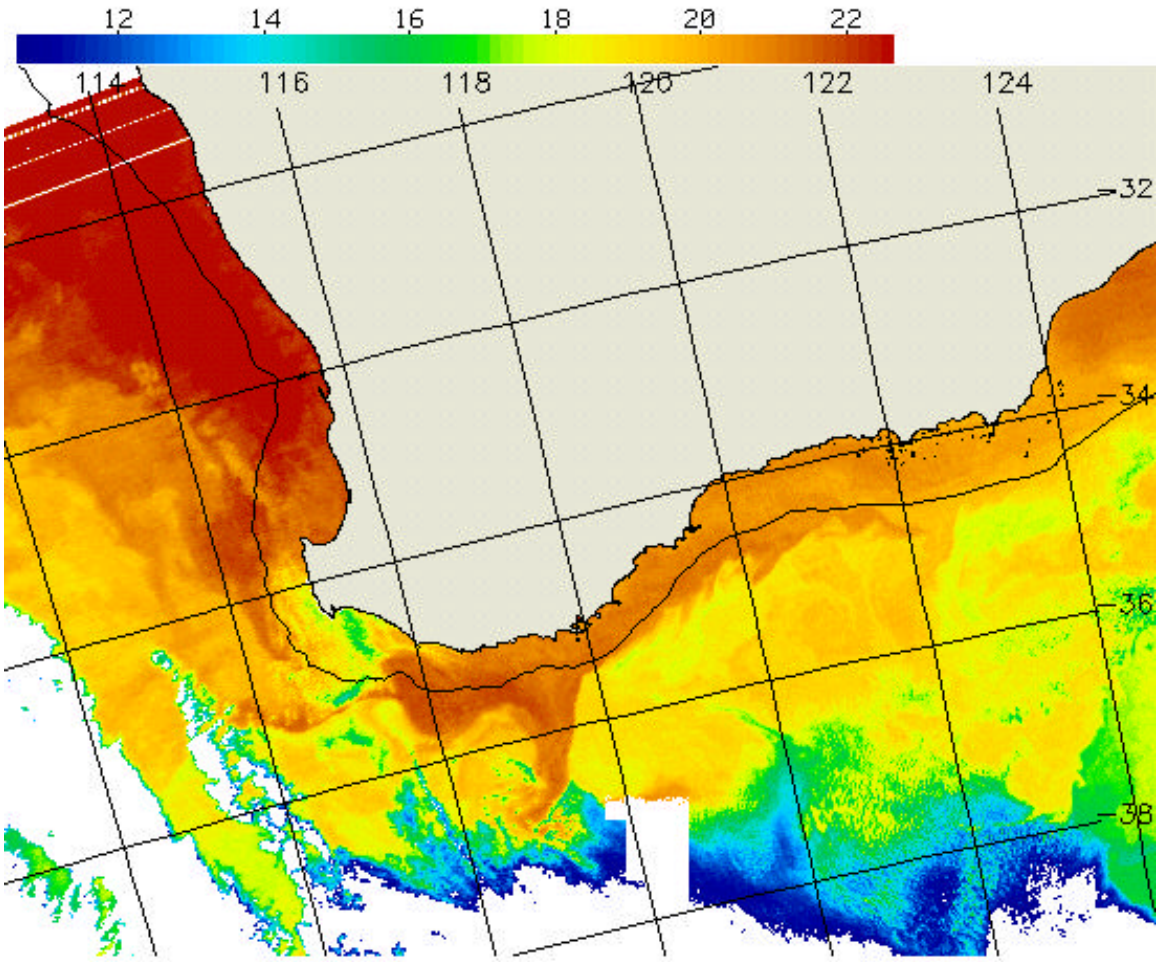

Figure 18a. Satellite image of surface water temperatures off Western Australia in April 2001, showing the warm waters of the Leeuwin Current (red/orange) and the cooler offshore water in green/blue. The white and mottled blue areas are clouds, and the black line represents the edge of the continental shelf (CSIRO, Marine Research).

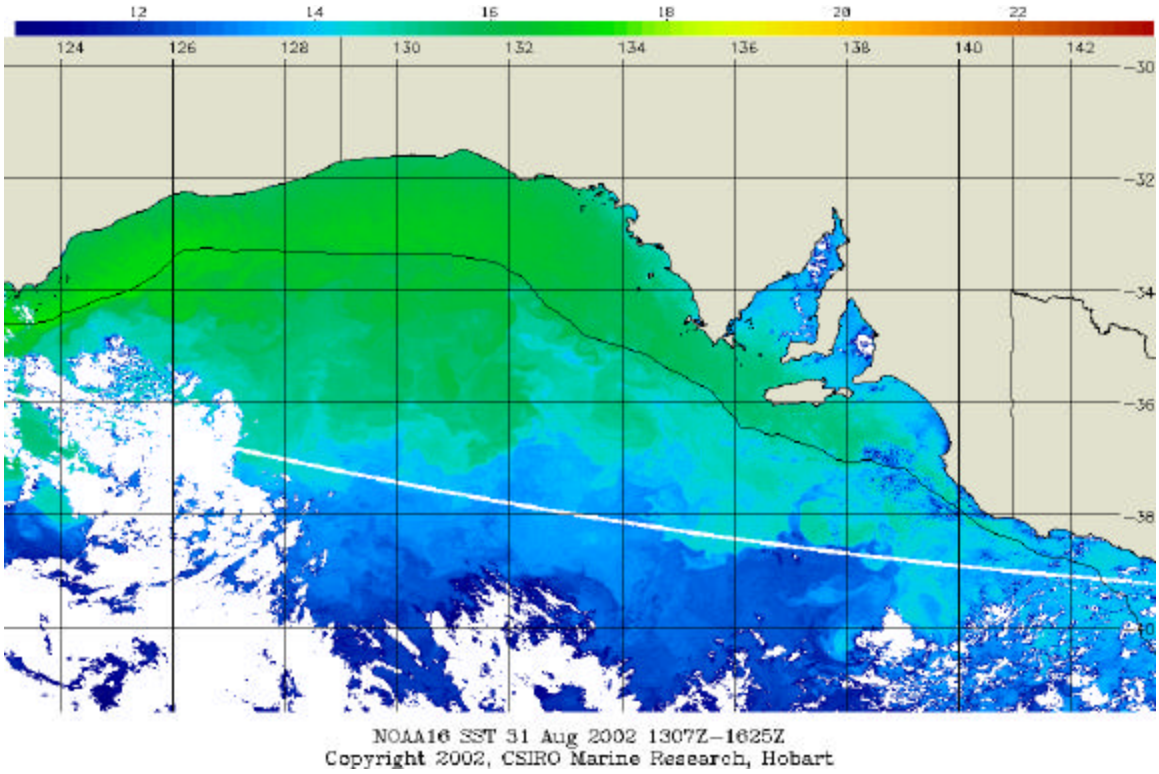

Figure 18b. Satellite image of surface water temperatures in the Great Australian Bight in August 2002, showing the relatively warmer waters of the Leeuwin Current (green) and the cooler offshore water in blue. The white and mottled blue areas are clouds, and the black line represents the edge of the continental shelf (CSIRO, Marine Research).

Exp. No.	Annual Wind	Annual Climatology	Topography
1	No	Horizontally Averaged	Yes
2	Yes	Horizontally Averaged	No
3	Yes	Horizontally Averaged	Yes
4	No	Full	No
5	No	Full	Yes
6	Yes	Full	No
7	Yes	Full	Yes

Table 1. Summary of experimental design.

Level	Depth (m)	Level	Depth (m)	Level	Depth (m)
1	0	12	300	23	1400
2	10	13	400	24	1500
3	20	14	500	25	1750
4	30	15	600	26	2000
5	50	16	700	27	2500
6	75	17	800	28	3000
7	100	18	900	29	3500
8	125	19	1000	30	4000
9	150	20	1100	31	4500
10	200	21	1200	32	5000
11	250	22	1300	33	5500

Table 2. Vertical levels and depths used by Levitus and Boyer (1994) and Levitus et al. (1994)

Level	Sigma Value	Level	Sigma Value
1	0	12	-0.61538
2	-0.00961	13	-0.69231
3	-0.01923	14	-0.76923
4	-0.03846	15	-0.84615
5	-0.07692	16	-0.92308
6	-0.15385	17	-0.96154
7	-0.23077	18	-0.98077
8	-0.30769	19	-0.99038
9	-0.38462	20	-0.99519
10	-0.46154	21	-1.0
11	-0.53846		

Table 3. Values of sigma levels

THIS PAGE INTENTIONALLY LEFT BLANK

LIST OF REFERENCES

Australian Oceanographic Data Centre (AODC), Oceanographic Analysis of South-eastern and South-western Australia, http://www.aodc.gov.au/Manuals/EAC/Introduction.html, Accessed 15 Apr 01.

Batteen, M. L., and C. L. Butler, Modeling Studies of the Leeuwin Current Off Western and Southern Australia, *J. Phys. Oceanography*, 28, 2199-2221, 1998.

Batteen, M. L., R. L. Haney, T. A. Tiekling, and P. G. Renaud, A Numerical Study of Wind Forcing of Eddies and Jets in the California Current System. *J. Mar. Research*, 47(3), 493-523, 1989.

Batteen, M. L., and M. J. Rutherford, Modelling Studies of Eddies in the Leeuwin Current: The Role of Thermal Forcing, *J. Phys. Oceanography*, 20, 1484-1520, 1990.

Batteen, M. L., M. J. Rutherford, and E. J. Bayler, A Numerical Study of Wind and Thermal Forcing Effects on the Ocean Circulation Off Western Australia, *J. Phys. Oceanography*, 22, 1406-1433, 1992.

Batteen, M. L., T. J. Tworek, and A. W. Cox, Modeling Studies of the Effects of Seasonal Wind Forcing and Thermohaline Gradients on the Leeuwin Current System, *Progress in Oceanography*, 2000, submitted.

Boedeker, S., A Fine Resolution Model of the Leeuwin Current System, Masters Thesis, Naval Postgraduate School, Monterey, CA, 76 pp, 2001.

Blumberg, A. F., and G. L. Mellor, A Description of a Three-Dimensional Coastal Ocean Circulation Model, In: *Three-Dimensional Coastal Ocean Models, Coastal Estuarine Sci*., 4, edited by N. Heaps, pp 1-16, AGU, Washington, DC, 1987.

Bye, J. A. T., The South East Indian Ocean and Great Australian Bight: A Brief Oceanographic Survey, http://www.es.flinders.edu.au/~pbarker/bye.html, Accessed 14 Apr 02.

Chapman, D. C., Numerical Treatment of Cross-Shelf Open Boundaries in a Barotropic Coastal Ocean Model, *J. Phys. Oceanography*, 25, 1060-1075, 1985.

Church, J. A., G. R. Cresswell, and J. S. Godfrey, The Leeuwin Current. In: *Poleward Flows Along Eastern Ocean Boundaries*, S. Neshhyba, C. N. K. Moorers, R. I. Smith, and R. T. Barber, Eds., Springer-Verlag, 230-252, 1989.

Cirano, M. and J. F. Middleton, The Mean Wintertime Circulation Along Australia's Southern Shelves: A Numerical Study, *J. Phys. Oceanography*, 2002, submitted.

Cresswell, G. R., and T. J. Golding, Observations of a South-Flowing Current in the Southeastern Indian Ocean, *Deep-Sea Res.*, 27A, 449-466, 1980.

Cresswell, G. R., and J. L. Peterson, The Leeuwin Current South of Western Australia, *Aust. J. Mar. Freshwater Res.*, 44, 285-303, 1993.

Ezer, T., and G. L. Mellor, Diagnostic and Prognostic Calculations of the North Atlantic Circulation and Sea Level Using a Sigma Coordinate Ocean Model, *J. of Geophys. Res.*, 99(C7), 14159-14171, 1994.

Ezer, T., and G. L. Mellor, Simulations of the Atlantic Ocean With a Free Surface Sigma Coordinate Ocean Model, *J. of Geophys. Res.*, 102(C7), 15647-15657, 1997.

Gill, A., *Atmosphere-Ocean Dynamics*. International Geophysics Series, 30, 662 pp, 1982.

Godfrey, J. S., and K. R. Ridgway, The Large-Scale Environment of the Poleward-Flowing Leeuwin Current, Western Australia: Longshore Steric Height Gradients, Wind Stresses and Geostrophic Flow, *J. Phys. Oceanography*, 15, 481-495, 1985.

Godfrey, J. S., D. J. Vaudrey, and S. D. Hahn, Observations of the Shelf-Edge Current South of Australia Winter 1982, *J. Phys. Oceanography*, 16, 668-679, 1986.

Herzfeld, M., The Annual Cycle of Sea Surface Temperature in the Great Australian Bight, *Progress in Oceanography*, 39, 1-27, 1997.

Herzfeld, M., M. Schodlock, and M. Tomczak, Water Mass Formation, Upwelling and Fronts in the Great Australian Bight, http://gaea.es.flinders.edu.au/~mattom/GAB/watermass.html, Accessed 15 Apr 01.

Herzfeld, M., and M. Tomczak, Numerical Modelling of Sea Surface Temperature and Circulation in the Great Australian Bight, *Progress in Oceanography*, 39, 29-78, 1997.

Hirst, A. C., and J. S. Godfrey, The role of Indonesian Throughflow in a Global Ocean GCM, *J. Phys. Oceanography*, 23,1057-1086, 1993.

Kennedy, R. A. Jr., A Numerical Study of the Forcing Mechanisms of the Leeuwin Current System, Masters Thesis, Naval Postgraduate School, Monterey, CA, 97 pp, 2002.

Levitus, S., and T. P. Boyer, World Ocean Atlas 1994, Vol. 4: Temperature, *NOAA Atlas NESDI 4*, 117 pp., U. S. Dept. of Commerce, Washington, D.C., 1994.

Levitus, S., R. Burgett, and T. P. Boyer, World Ocean Atlas 1994, Vol. 3: Salinity, *NOAA Atlas NESDI 3*, 99 pp., U. S. Dept. of Commerce, Washington, D.C., 1994.

Marchesiello, P., J. C. McWilliams, and A. Shchepetkin, Open Boundary Conditions for Long-Term Integration of Regional Oceanic Models, *Ocean Modeling*, 3, 1-20, 2001.

Martinho, A. C., A Fine Resolution Model of the Coastal Eastern Boundary Current Systems Off Iberia and Morocco, Masters Thesis, Naval Postgraduate School, Monterey, CA, 93 pp, 2001.

Martinho, A. C., Sensitivity Studies Using Multi-Block Nesting and Open Boundary Conditions for Terrain Bottom-Following Ocean Models, Ph.D. Dissertation, Naval Postgraduate School, Monterey, CA, 2002.

McCreary, J. P., S. R. Shetye, and P. K. Kundu, Thermohaline Forcing of Eastern Boundary Currents: With Application to the Circulation Off the West Coast of Australia, *J. Mar. Res.*, 44, 71-92, 1986.

Mellor, G. L., User's Guide for a Three-Dimensional, Primitive Equation, Numerical Ocean Model, 40 pp, Program in Atmos. And Ocean Sci. Report, Princeton Univ., Princeton, NJ 1996.

Mellor, G. L., L. Y. Oey, and T. Ezer, Sigma Coordinate Pressure Gradient Errors and the Seamount Problem, *J. Atmospheric and Ocean Technology*, 15, 1122-1131, 1998.

Mellor, G. L., and T. Yamada, Development of a Turbulence Closure Model for Geophysical Fluid Problems, *Rev. Geophys. Space Phys*., 20, 851-875, 1982.

Middleton, J. F., Wind-Forced Upwelling: The Role of the Surface Mixed Layer, *J. Phys. Oceanography*, 30, 745-763, 2000.

Middleton, J. F., and M. Cirano, Wind Forced Downwelling Slope Currents: A Numerical Study, *J. Phys. Oceanography*, 29, 1723-1743, 1999.

Middleton, J. F., and M. Cirano, A Northern Boundary Current Along Australia's Southern Shelves: The Flinders Current, *J. Phys. Oceanography*, 2001, submitted.

Middleton, J. F., and G. Platov, The Mean Summertime Circulation along Australia's Southern Shelves: A Numerical Study, *J. Phys. Oceanography*, 2002, submitted.

Palma, E. D., and R. P. Matano, On the Implementation of Passive Open Boundary Conditions for a General Circulation Model: the Barotropic Mode, *J. Geophys. Res.*, 103(C1), 1319-1341, 1998.

Palma, E. D., and R. P. Matano, On the Implementation of Passive Open Boundary Conditions for a General Circulation Model: the Three-Dimensional Case, *Journal of Geophysical Research*, 105(C4), 8605-8627, 2000.

Parrish, R. H., A. Bakun, D. M. Husby, and C. S. Nelson, Comparitive Climatology of Selected Environmental Processes in Relation to Eastern Boundary Current Pelagic Fish Reproduction. In: *Proc. Expert Consultation to Examine Changes in Abundance and Species of Neritic Fish Resources*, G. D. Sharp and J. Csirke, Eds., San Jose, Costa Rica, FAO Fish Rep. 291, Vol. 3, 731-778, 1983.

Pearce, A. F., and R. W. Griffiths, The Mesoscale Structure of the Leeuwin Current: a Comparison of Laboratory Model and Satellite Images. *Journal of Geophysical Research* 96, 16739-16757, 1991.

Sandwell, D. T., and W. F. Smith, Global Bathymetric Prediction for Ocean Modeling and Marine Geophysics, 1996.

Smagorinsky, J., S. Manabe, and J. L. Holloway, Numerical Results From a Nine-Level General Circulation Model of the Atmosphere, *Mon. Weather Rev.*, 93, 727-768, 1965.

Smith, R. L., A. Huyer, J. S. Godfrey, and J. A. Church, The Leeuwin Current Off Western Australia, 1986-1987, *J. Phys. Oceanography*, 21, 323-345, 1991.

Thompson, R. O. R. Y., Observations of the Leeuwin Current Off Western Australia, *J. Phys. Oceanography*, 14, 623-628, 1984.

Thompson, R. O. R. Y., Continental-Shelf Scale Model of the Leeuwin Current, *J. Mar. Res.*, 45, 813-827, 1987.

Tomczak, M., and J. S. Godfrey, *Regional Oceanography: An Introduction*, Elsevier Science, Pergamon, Oxford, England, 1994.

Trenberth, K. E., W. G. Large, and J. G. Olsen, The Mean Annual Cycle in Global Ocean Wind Stress, *J. Phys. Oceanography*, 20, 1742-1760, 1990.

Tworek, T. J., The Role of the Planetary Beta Effect on Currents and Eddies in the Leeuwin Current System, Masters Thesis, Naval Postgraduate School, Monterey, CA, 163 pp, 2000.

Wooster, W. S., and J. L. Reid Jr., Eastern Boundary Currents, in *The Seas*, Vol. 2, edited by M. N. Hill, pp. 253-280, John Wiley, New York, 1963.

INITIAL DISTRIBUTION LIST

1. Defense Technical Information Center
   Ft. Belvoir, Virginia

2. Dudley Knox Library
   Naval Postgraduate School
   Monterey, California

3. Chair, Department of Oceanography (Code OC/Bv)
   Naval Postgraduate School
   Monterey, CA

4. Dr. Mary L. Batteen, Department of Oceanography (Code OC/Bv)
   Naval Postgraduate School
   Monterey, CA

5. Dr. Curtis Collins, Department of Oceanography (Code OC/Co)
   Naval Postgraduate School
   Monterey, CA

6. CMDR Craig Roy
   Directorate of Oceanography and Meteorology
   Sydney, NSW, Australia

7. LEUT Robyn Phillips
   Directorate of Oceanography and Meteorology
   Sydney, NSW, Australia